MRS Studies of the Effects of Dietary Interventions on Hepatic Metabolism

Stephen Bawden BSc

Thesis submitted to the University of Nottingham

for the degree Doctor of Philosophy

December 2014

Abstract

Magnetic Resonance Spectroscopy is a powerful non-invasive tool for investigating liver metabolism *in vivo*. PRESS and STEAM localized ^{1}H MRS can be used to provide liver lipid measurements calculated from the fat to water peak ratios. Surface coils can also be used to measure other metabolites using multinuclear MRS, ^{13}C MRS directly measures glycogen levels and ^{31}P MRS measures ATP and other phosphate metabolites. This thesis reports on studies undertaken to develop these techniques and describes a number of *in vivo* investigations that explored the effects of dietary interventions on hepatic metabolism.

Technical developments were made to automate ^{1}H MRS lipid analysis and results showed that automatic post processing and peak fitting provided values in close agreement with manual spectral analysis in a much shorter analysis time. They also provide more repeatable results with less observer's subjective error and require less expertise. This makes automated processing (and MRS) more acceptable in a purely clinical setting. Surface coil B_1 field inhomogeneity in ^{13}C MRS at 3T was also explored and a Biot-Savart static field simulation was used with RF pulse modelling to estimate the sensitivity across a single loop coil. This showed good agreement with phantom data and can be used *in vivo* to understand distance from coil effects in liver tissue. ^{13}C MRS glycogen responses to a low calorie morning meal were also studied and showed significant changes compared to a control arm but not above baseline.

^{31}P MRS was used in an oral fructose challenge study to investigate the dynamic postprandial changes in liver ATP levels following consumption. The β-ATP peak, representing total ATP, declined for some of the time course, and in most subjects began to recover by the last measurement point. Correlations of rates of depletion with BMI and liver lipid levels, and between rates of recovery and baseline glycogen levels were significant and this technique may be able to be developed as a biomarker of liver health. A second study looked at the effects of high and low glycaemic index diets on liver lipid and glycogen levels measured using ^{1}H and ^{13}C MRS and found that a high compared with low glycaemic index breakfast produced a greater rise in liver glycogen stores. Also, after a 7 day high glycaemic index diet liver lipid levels were raised compared with a low glycaemic index diet.

In a final study CEST was explored as a method of measuring hepatic glycogen levels *in vivo*. In a new technique called spectroCEST multiple ^{1}H spectra were acquired at varying saturation frequencies and a Z spectrum produced. Individual spectra were used to quantify fat fractions and the Z spectrum asymmetry used to determine glycogen levels. This technique was tested in phantoms and piloted *in vivo* with success, offering a potential tool for measuring glycogen and lipid during a single scan session.

List of Publications

Articles in Journals

A Low Calorie Morning Meal Prevents the Decline of Hepatic Glycogen Stores: A Pilot *in vivo* ^{13}C Magnetic Resonance Study

***S. J. Bawden**, M. C. Stephenson, E. Ciampi, K. Hunter, L. Marciani, R. C. Spiller, G. P. Aithal, P. G. Morris, I. A. Macdonald, P. A. Gowland*

Food & Function, 2014, **5**(9), 2237 - 2242; Impact Factor 2.907

Articles in Peer Reviewed Conferences

Investigating Alterations in Hepatic ATP level Following Fructose and Fructose+Glucose Ingestion: A Simple Non-invasive Technique to Assess Liver Fucntion Using ^{31}P MRS

***S. J. Bawden**, M. C. Stephenson, L. Marciani, I. A. Macdonald, P. A. Gowland, P. G. Morris*

ISMRM 2012 20th Annual Meeting & Exhibition 5th – 11th May, Melbourne, Australia

Can ^{13}C MRS Be Used to Monitor Changes in Hepatic Glycogen Levels Following a Low Dose Oral Glucose Challenge?

S. J. Bawden*, M. C. Stephenson, E. Ciampi, J. Lane, L. Marciani, P. G. Morris, I. A. Macdonald, G. P. Aithal , K. Hunter, P. A. Gowland*

ISMRM 2013 21st Annual Meeting & Exhibition 20th – 26th April, Salt Lake City, USA

Simultaneously Measuring Glycogen and Lipid Levels Using Localized CEST Spectroscopy at 3T

S. J. Bawden*, O. Mougin, K. Hunter, L. Marciani, P. A. Gowland*

ISMRM 2014 22nd Annual Meeting & Exhibition 10th – 16th May, Milan, Italy

Surface Coil Sensitivity of ^{13}C Magnetic Resonance Spectroscopy at 3T: A Comparison of Static Field Approximations, Phantom Repositioning and MRSI data

S. J. Bawden*, K. Hunter, L. Marciani, P. Glover, P. G. Morris, P. A. Gowland*

20th Annual Scientific Meeting of the British Chapter of ISMRM 2014 3rd – 5th September, Edinburgh, UK

Acknowledgments

I would like to express my thanks to the many people who have helped me throughout my studentship. A special thanks to Professor Penny Gowland and Dr Luca Marcini who have always given me their time and support. I would also like to acknowledge Professor Peter Morris and Dr Mary Stephenson for all their expertise; and Professor Ian MacDonald and Professor Guru Aithal with whom I have collaborated on a number of projects and who have always been willing to provide excellent advice. Many thanks also to those at Unilever, in particular Dr Karl Hunter and Dr Elisabetta Ciampi.

For my many colleagues at the SPMMRC I am extremely grateful, especially Lesley Martin and Liz Croal who have always been so helpful and friendly, and Dr Andrew Peters for his expertise in the technical aspects of scanners and software.

I am also incredibly thankful to all my good friends in Leicester, to those at Knighton Free Church, and to those in the Evington Road community group who have become family to me. To my actual family in Swansea also I owe much gratitude, to my Mammy and Daddy particularly who have consistently shown love and support to me throughout my life.

Finally, but most importantly, to my beautiful wife Rachel and my precious daughter Alyssa. You have been my constant joy and I am deeply thankful to you – I could not have done this without you. I wish to praise my Lord and Saviour Jesus Christ for His gift of life and hope.

Contents

Chapter 1 Introduction 1

1.1 MRS in Hepatic Energy Metabolism 1

1.1.1 Introduction 1

1.1.2 Liver Fat MRS 3

1.1.3 Hepatic Glycogen MRS 5

1.1.4 ATP MRS 8

1.2 Thesis Aims 9

1.3 Thesis Overview 9

Chapter 2 NMR Theory and Instrumentation 11

2.1 Quantum Mechanical Foundation 11

2.1.1 Nuclear Spin States 11

2.1.2 Magnetic Moment 13

2.1.3 Spin ½ Nuclei 14

2.1.4 Spin Precession....16

2.1.5 Boltzmann Distribution....16

2.2 Classical Description....18

2.2.1 Magnetization Vector....18

2.2.2 RF Pulse and $B1$....19

2.2.3 T_1 and T_2 Relaxation....19

2.2.4 Bloch Equations....21

2.2.5 Flip Angle....22

2.2.6 B Effective....23

2.3 NMR Signal....24

2.3.1 Free Induction Decay....24

2.3.2 Fourier Transform....25

2.3.3 Signal to Noise Ratio....26

2.4 Magnetic Resonance Spectroscopy....27

2.4.1 Introduction....27

2.4.2 Chemical Shift Scale....28

2.4.3 J-Coupling....31

2.4.4 Localization 35

2.4.5 Surface Coils 36

2.5 Magnetization Transfer 37

2.5.1 Introduction 37

2.5.2 CEST Effects 37

2.5.3 Non CEST Effects 39

2.6 Pulse Shape and Gradients 41

2.6.1 Amplitude Modulation 41

2.6.2 Frequency Modulation and Adiabaticity 42

2.6.3 Gradients 44

2.7 Instrumentation 45

2.7.1 Introduction 45

2.7.2 Magnet 46

2.7.3 RF Transmission Section 48

2.7.4 Receiver Section 48

2.7.5 Gradient Coils 50

2.7.6 Surface Coil Hardware 52

2.8 MR Safety 53

2.9 Conclusion 55

Chapter 3 Hepatic Metabolism 56

3.1 The Liver.....56

3.2 Metabolism and Energy Storage 57

3.2.1 Introduction 57

3.2.2 Overview 58

3.3 Glycolysis and Gluconeogenesis 59

3.4 Glycogenesis and Glycogenolysis 61

3.5 Fatty Acid Synthesis and β-oxidation.....64

3.6 TCA Cycle 66

3.7 ATP.....67

3.8 Conclusion 69

Chapter 4 Technical developments of ^{1}H and ^{13}C MRS for Measurements of Hepatic Metabolism 70

4.1 Introduction.....70

4.2 ^{1}H MRS Measurements of Hepatic Fat Fractions.....73

4.2.1 Introduction 73

4.2.2 Method 75

4.2.3 Statistical Analysis 79

4.2.4 Results 80

4.2.5 Discussion 83

4.3 Surface Coil Signal Sensitivity of ^{13}C MRS Measurements of Glycogen Stores 86

4.3.1 Introduction 86

4.3.2 Method 88

4.3.3 Results 95

4.3.4 Discussion 107

4.3.5 Relevance to *In Vivo* Liver Studies 110

4.4 Lower end sensitivity of *in vivo* ^{13}C MRS in the liver 113

4.4.1 Introduction 113

4.4.2 Material and Methods 113

4.4.3 Results 117

4.4.4 Discussion 121

4.5 Conclusions 126

Chapter 5 *In Vivo* multinuclear MRS Studies of Hepatic Metabolism 129

5.1 Introduction.....129

5.2 Investigating the effects of an Oral Fructose Challenge on Hepatic ATP Reserves in Healthy Volunteers: A ^{31}P MRS Study.....133

5.2.1 Introduction 133

5.2.2 Study Design.....133

5.2.3 Data Acquisition.....134

5.2.4 MRS Analysis.....136

5.2.5 Statistical Analysis 137

5.2.6 Results 138

5.2.7 Discussion.....142

5.3 Multinuclear MRS Investigation of the Impact of High versus Low Glycaemic Index Diets on Hepatic Metabolism: A Randomized Cross Over Study 148

5.3.1 Introduction 148

5.3.2 Subjects.....149

5.3.3 Study Design.....149

5.3.4 Data Acquisition 154

5.3.5 MRS Analysis 157

5.3.6 Statistical Analysis 158

5.3.7 Results 158

5.3.8 Discussion 170

5.4 Conclusions 177

Chapter 6 SpectroCEST to Measure Liver Lipid and Glycogen Levels 179

6.1 Background 179

6.1.1 Introduction 179

6.1.2 GlycoCEST *in vivo* 180

6.1.3 GlycoCEST Spectroscopy and Lipid Measurements 181

6.2 Pilot Study 183

6.2.1 Method 183

6.2.2 MRS Analysis 187

6.3 Discussion 194

6.4 Future Work 197

6.5 Conclusions.....197

Chapter 7 Conclusions.....199

List of Abbreviation

ADC	Analogue to Digital Converter
ADP	Adenosine Diphosphate
AFP	Adiabatic Full Passage
AHP	Adiabatic Half Passage
AM	Amplitude Modulation
AMP	Adenosine Monophosphate
AMPD	Adenosine Monophosphate Deaminase
AMPK	Adenosine Monophosphate activated protein Kinase
ATP	Adenosine Triphosphate
AUC	Area Under Curve
BMI	Body Mass Index
cAMP	cyclic Adenosine Mono-Phosphate
CEST	Chemical Exchange Saturation Transfer
CV	Coefficient of Variation
DAC	Digital to Analogue Converter
EMF	Electro Magnetic Force
EPI	Echo Planar Imaging
FFA	Free Fatty Acids
FID	Free Induction Decay
GI	Glycaemic Index
HGI	High Glycaemic Index
HS	Hyperbolic Secant
IPAQ	International Physical Activity Questionnaire
IV	Intravenous
LB	Line Broadening
LD	Lorentzian Difference
LDL	Low Density Lipids
LGI	Low Glycaemic Index
MRI	Magnetic Resonance Imaging
MRS	Magnetic Resonance Spectroscopy
MTC	Magnetization Contrast effects
MTR_{asym}	Magnetization Transfer Asymmetry
NMR	Nuclear Magnetic Resonance
NAFLD	Non-Alcoholic Fatty Liver Disease
NASH	Non-Alcoholic Steatohepatitis
NOE	Nuclear Ovenhauser Effect
OIA	Offset Independent Adiabaticity
Pi	Inorganic Phosphate
PCr	Phosphocreatine
PDE	Phosphodiesters
PDH	Pyruvate Dehydrogenase
PFG	Pulse Field Gradient
PME	Phosphomonesters
PRESS	Point Resolved Spectroscopy
PSD	Phase Sensitive Detectors

RF	Radio Frequency
QMC	Queens medical Centre
SAR	Specific Absorption Ratio
SD	Standard Deviation
SEM	Standard Error on Mean
SNR	Signal to Noise Ratio
STEAM	Stimulated Echo Acquisition Mode
SVS	Single Voxel Spectroscopy
T2D	Type 2 Diabetes
TCA	Tricarboxylic Acid
TE	Echo Time
TR	Repetition Time
TMS	Tetramethylsilane
UTP	Uridine Triphosphate
VAS	Visual Analogue Scale
VLDL	Very Low Density Lipids
ZF	Zero Filling

Chapter 1 Introduction

1.1 MRS in Hepatic Energy Metabolism

1.1.1 Introduction

Metabolic disorders and fatty liver disease are becoming a vast global health burden [1, 2]. This can be attributed in part to dietary intake, which has changed considerably in recent decades marked by an increase in total energy consumption and a shift in dietary composition [3] as well as reduced levels of physical activity. Studies have shown that increased energy intake can increase liver lipid levels [4] in healthy subjects; short term hyperalimentation [5, 6] and has even been associated with elevation of liver enzymes as well as biomarkers of liver injury which correlate with liver fat content [7]. These and other factors are believed to be contributing factors that have led to the increased prevalence of type II diabetes, non-alcoholic fatty liver disease (NAFLD) and its progression to non-alcoholic Steatohepatitis (NASH).

The liver plays a central role in the metabolism and energy storage of dietary intake and is key to understanding the basic mechanisms underpinning the current crisis and evaluating the effects of preventative measures such as dietary intervention. Nutrients absorbed from the small intestines into the blood stream are transferred initially to the liver where they are metabolised and stored as either glycogen or lipid, providing an energy reserve for the post

absorptive period. Glycogen is later broken down to provide glucose between meals, whereas lipid provides a longer term energy store (Chapter 3).

Studies that investigate liver metabolism and the effects of medications or interventions in humans are particularly difficult as historically they required biopsies which sample a very limited volume, are highly invasive and uncomfortable for subjects, and can lead to complications. Magnetic Resonance Spectroscopy (MRS) provides a powerful non-invasive alternative and is a well validated tool for investigating basic physiology in the liver, in addition to the effects of dietary and lifestyle interventions [8, 9]. It uses non ionising radiation with no long term damaging effects and can be used to determine liver glycogen [10] and liver lipid levels [4] sampling larger liver volumes without the need for biopsies.

As such, many studies in the last few decades have explored the immediate post prandial effects of meal intake on hepatic glycogen metabolism using MRS techniques [11-13] and much information has been elucidated. In addition, the effects of longer term dietary interventions on both hepatic glycogen and lipid have been investigated many times [4, 14]. These have also been explored in patient groups, for example those with type II diabetes, and significant differences have been found compared with healthy population [12].

MRS has also been used to monitor *in vivo* adenosine triphosphate (ATP) levels and provides unique insights into the immediate postprandial regulation of energy supply [15]. The data from these studies work alongside lipid and glycogen measurements to bring together multiple aspects of metabolism in the

liver which together build a full picture of basic liver physiology and potential risk factors for disease.

1.1.2 Liver Fat MRS

Liver biopsies, the current clinical standard for assessing liver lipid levels, suffer many difficulties and risk factors and can be highly uncomfortable for patients [16]. Also, histology only examines a small section of the liver and assumes homogenous lipid dispersion for steatosis grading [17]. These and other factors have led some to question its use as the clinical standard [18]. Various *in vivo* Magnetic Resonance techniques have been used to determine liver lipid levels [19, 20], providing a completely non-invasive method with strong clinical potential. These techniques rely on the chemical shift properties of fatty acid hydrogen spins (Chapter 2). Of these techniques, MRS currently offers the clearest distinction between peaks, gives the most accurate quantification of liver lipid *in vivo* and has been well validated [21, 22] and used in many published articles [4, 19].

Liver tissue fat fractions are quantified by measuring the water and fat ^{1}H signals in the MR spectra and calculating the fat to water ratios. Hydrogens from fatty acid chains provide distinct signals in the spectra which can be easily resolved and correspond to the various positions of hydrogen spins within the lipid molecule. Six of these peaks have been named in *ex vivo* animal fat phantom MRS [23], as designated in the Table 1.1 below.

Peak	Location	Assignment	Peak Type
1	5.30 ppm	-CH=CH-	Multiplet
	5.19 ppm	-CH-O-CO-R	Multiplet
2	4.20 ppm	$-CH_2-O-CO-R$	Multiplet
3	2.75 ppm	$-CH=CH-CH_2-$ CH=CH-	Multiplet
4	2.20 ppm	$-CO-CH_2-CH_2-$	Multiplet
	2.02 ppm	$-CH_2-CH=CH-CH_2-$	Multiplet
5	1.60 ppm	$-CO-CH_2-CH_2-$	Multiplet
	1.30 ppm	$-(CH_2)_n-$	Multiplet
6	0.90 ppm	$-(CH_2)_n-CH_3$	Triplet

Table 1.1 Lipid Peak assignment.

Of these peaks, 1 and 2 tend to overlap with the water peak *in vivo* and peak 3 is generally not detectable. Typically, a single voxel spectrum is acquired with water suppression used to better resolve lipid peaks (Chapter 2). Various methods are used to determine the fat peak area. In most cases, a composite peak area is determined as the signal between 0.5 to 3 ppm [24] although this requires good field shimming and water suppression and is difficult in cases of low fat content. Alternatively, peak fitting algorithms can be used to measure the integral under the main $(CH_2)_n$ peak (peak 5 from Table 1.1) which has the largest signal and reflects the main carbon chain backbone of triglycerides.

Fat to water ratios (R) can be converted to absolute tissue wet weight fat fractions (%w/w) using the following equation:

$$\%w/w = \frac{RT_w}{(R+1)T_w}$$

Equation 1.1

where T_w is the fractional mass of tissue water (~ 0.711 g water / g tissue). Further corrections of the fat to water ratios can be made to account for T_2 relaxation giving a correction factor:

$$Z(TE) = \exp(-TE/T_2^{wat}) \,/\, \exp\left(-TE/T_2^{fat}\right)$$

Equation 1.2

T_2 relaxation effects are explored further in Chapter 4. The proton density of water and each fat peak can also be considered to provide more accurate quantification [25]. These equations were used throughout this thesis to give absolute %w/w fat fraction values.

Automated post processing of ^{1}H MRS is explored in chapter 4 and applied to *in vivo* studies in Chapter 5.

1.1.3 Hepatic Glycogen MRS

Alongside liver fat fractions measured using ^{1}H MRS, other spin ½ nuclei can provide useful information about metabolites within hepatic tissue. ^{13}C MRS, for example, can be used to measure hepatic glycogen stores. Given the

importance of glycogen in the postprandial stages of nutrition and its relationship with overall energy metabolism (Chapter 3), alongside the current global rise in metabolic disorders, this technique provides a powerful and clinically novel tool to non-invasively explore basic physiology in healthy volunteers or patients and also the effects of dietary and lifestyle interventions.

The C_1 nuclei in glycogen produce an MRS peak signal at 100.5ppm (Figure 1.1). Whilst there are many peaks in the *in vivo* spectrum, most of which are fat peaks, none of these are overlapping with the glycogen peak allowing well resolved quantification.

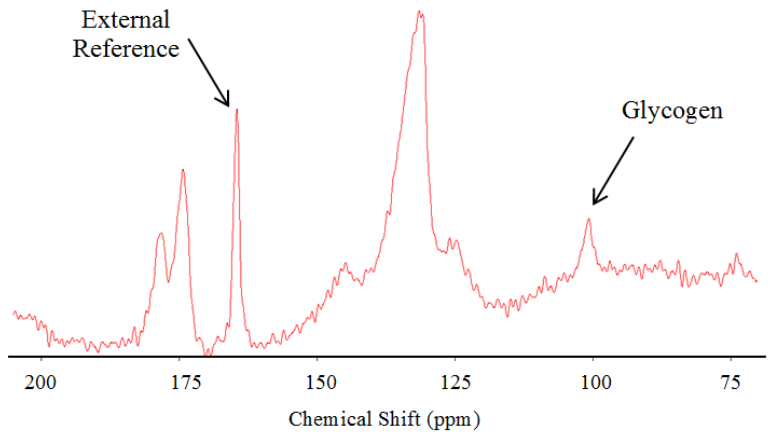

Figure 1.1 ^{13}C MR spectrum of a 200 mmol/l glycogen phantom. C_1 glycogen signal is seen at ~100.4 ppm with a reference peak at 170ppm.

It was first suggested that natural abundance ^{13}C MRS could be used to measure glycogen levels *in vivo* in 1987 [9] and since then has been well validated in human muscle [8, 26] and liver [11, 27]. Stephenson *et al.* tested measurement repeatability in healthy volunteers at 3T over 5 repeat acquisitions and reported single session coefficient of variation in hepatic and

muscle glycogen measurements of 13% and 22% respectively [25]. Many studies have used this technique to compare the effects of nutritional intake [13, 28] or exercise [29] and also variation between healthy volunteers and patients [12, 30].

Although natural abundance ^{13}C provides a unique and powerful way of investigating energy metabolism in the liver and muscle, there are a number of difficulties compared to ^{1}H MRS which need to be considered. Firstly, the ^{13}C nucleus has a gyromagnetic ratio of 10.705 MHz T^{-1} which is approximately 1/4 of that of the ^{1}H nucleus. The strength of the NMR signal depends on a number of factors discussed in section 2.3.3 which together reduce the overall signal to noise ratio (SNR) of ^{13}C MRS compared with ^{1}H MRS. Additionally, the sensitivity is further reduced because the natural isotopic ratio of Carbon is made up of only ~1% Carbon-13 which dramatically reduces the number of spin 1/2 nuclei in a given sample. All these factors of natural abundance ^{13}C MRS gives an SNR ~3200 less than that of ^{1}H MRS [31]. This has led many studies to use ^{13}C labelled products to explore glycogen metabolism *in vivo* [28] which provides particularly useful information about the uptake of labelled products and the direct pathway to glycogen production.

However, various techniques can be used to enhance the SNR from natural abundance ^{13}C MRS such as polarisation transfer or proton decoupling [32]. Natural abundance ^{13}C MRS does provide some important information that labelled ^{13}C MRS cannot, such as endogenous glycogen concentrations. Using higher field strengths will also help enhance the signal, and acquiring measurements over many signal averages will increase the SNR by $\sim\sqrt{n}$.

Given the large volume of liver tissue close to the surface of the body and also major muscles such as the gastrocnemius, a large amount of signal can be obtained from *in vivo* samples even at low isotopic ratios. This is exploited by the use of surface coils which can be positioned close to the surface of the body for both transmit and receive signals. However, these produce an inhomogeneous B_1 field, which is explored in Chapter 4.

1.1.4 ATP MRS

NAFLD and its progressive form, NASH, have also been associated with impaired homeostasis of hepatic ATP reserves. In particular, patients with NASH have been shown to have a reduced ability to replenish ATP following depletion [33]. It has been suggested that this inability to maintain ATP levels may prime hepatocytes to become vulnerable to injury by reactive oxygen species. Baseline hepatic ATP reserves have previously been shown to be more depleted in obese subjects [15, 34] which may be related to the increased frequency of NAFLD in the overweight population. The ability of hepatocytes to maintain adequate ATP reserves and replenish ATP levels post depletion has been hypothesised to be a critical mechanism underlying this pathogenesis.

Hepatic ATP reserves can be monitored noninvasively *in vivo* using ^{31}P MRS [35]. Using surface coils, localized ^{31}P MRS produces well resolved peaks for each of the 3 ATP phosphate groups (α-ATP, β-ATP and γ-ATP), along with inorganic phosphate (Pi), phosphodiesters (PDE) and phosphomonesters (PME) (Phosphocreatine (PCr) is also seen in muscle tissue but not in liver). A number of studies have used MRS to measure hepatic ATP levels and ATP

homeostasis in conjunction with an intravenous (IV) administration of fructose [6, 34, 36]. An *in vivo* study exploring hepatic ATP levels following an oral fructose challenge is discussed in Chapter 5.

1.2 Thesis Aims

The overarching aims of this thesis were to develop multinuclear MRS techniques for use in hepatic metabolism studies, and to apply these to *in vivo* human studies exploring the effects of dietary interventions on the liver. Specifically, ^{31}P MRS was used to explore the immediate post prandial effects and ^{1}H and ^{13}C MRS was used in combination to assess the short and longer term effects.

Technical methods were developed using a combination of computational modelling, phantom acquisition and a small human trial with the aim of improving current techniques and understanding better the NMR technologies applied. These techniques were then used to explore some of the current issues relating to liver health, such as the global rise in prevalence of NAFLD, with the aim of investigating the viability of new diagnostic techniques (liver ATP homeostasis) and preventative measures (dietary glycaemic index). A strong emphasis of these experiments was the use of multinuclear NMR technologies (^{31}P MRS, ^{1}H MRS, ^{13}C MRS and MRI) alongside each other to provide a full picture of basic hepatic physiology and pathogenesis.

1.3 Thesis Overview

Chapters 2 and 3 cover NMR theory along with a brief summary of hepatic metabolism theory.

Technical developments are outlined in Chapter 4, specifically improved post processing techniques for ^{1}H MRS lipid measurements, and also ^{13}C MRS surface coil effects (for use in *in vivo* glycogen experiments). Automatic post processing of MRS phase correction, frequency alignment and peak fitting are implemented and compared with manual processes using linear regression statistics. B_1 field inhomogeneities of surface coils are also explored, and applied to ^{13}C MRS measurements of liver glycogen reserves. The last section of Chapter 4 reports on a low dose oral glucose challenge study that considered the lower end sensitivity of liver glycogen MRS measurements.

In Chapter 5 the results from two experimental studies are reported and discussed. The first investigation considers the immediate postprandial effects of oral fructose intake on hepatic ATP reserves. The effects are also related to the baseline measures of liver lipid and glycogen levels using the techniques and developments discussed in Chapter 4. The second section of Chapter 5 reports on a randomized cross over design study on 8 subjects investigating the short and longer term effects of dietary glycaemic index on hepatic lipid and glycogen levels.

Finally, Chapter 6 explores a potential novel technique for measuring glycogen and lipid levels *in vivo* during a single scan session, named spectroCEST.

Chapter 2 NMR Theory and Instrumentation

This chapter covers the background theory of in vivo Magnetic Resonance Spectroscopy and the instrumentation used. Quantum mechanical and classical descriptions of the NMR phenomenon are given, and details of spectroscopy technique are explained.

2.1 Quantum Mechanical Foundation

2.1.1 Nuclear Spin States

Nuclear Magnetic Resonance (NMR) theory has grown over many years [37] having developed from early discoveries [38-40] and progressed with multiple contributions from a range of disciplines [41-44]. It relies on the fundamental quantum mechanical properties of particles [45] which vary between nuclei, as well as other related properties such as isotopic abundance. Some important properties of nuclei relevant for NMR are shown in Table 2.1.

Nucleus	Spin	Natural Isotopic Abundance	Gyromagnetic Ratio $\times 10^6\ \gamma/rad\ s^{-1}\ T^{-1}$
^{1}H	1/2	100%	267.522
^{12}C	0	98.9%	-
^{13}C	1/2	1.1%	67.262
^{31}P	1/2	~100%	108.394
^{19}F	1/2	100%	251.662

Table 2.1 Relevant NMR properties for a selection of nuclei.

Elementary particles (Leptons, Quarks etc.) are characterized by a spin quantum number S which produces an intrinsic spin angular momentum given by $\hbar\sqrt{S(S+1)}$ where $\hbar$ is Planck's constant $h/2\pi$ [46]. The direction of this angular momentum is defined by a second quantum number m (magnetic quantum number) which can have discrete value $m = -\mathrm{S}, -\mathrm{S}+1, \ldots, \mathrm{S}-1, \mathrm{S}$ resulting in $(2S\ +\ 1)$ quantum states. Together, these determine the spin state of the nucleus and give rise to the nuclear spin quantum number **I.**

The quantum dynamics of any nucleus can be described fully using the time dependant Schrodinger equation (Equation 2.1).

$$\mathbf{i}\hbar\frac{\boldsymbol{\partial}}{\boldsymbol{\partial t}}|\boldsymbol{\Psi}(\boldsymbol{t})\rangle = \widehat{\boldsymbol{H}}|\boldsymbol{\Psi}(\boldsymbol{t})\rangle$$

Equation 2.1

where $\boldsymbol{\Psi}$ is the wave function of the nucleus and $\widehat{\boldsymbol{H}}$ is the Hamiltonian operator which represents the quantised energy levels described in quantum theory. In NMR theory this can be simplified by only considering spin states and calculating solutions for the spin Hamiltonian operator $\widehat{\boldsymbol{H}}_{\boldsymbol{spin}}$ [47].

2.1.2 Magnetic Moment

Charged particles with non-zero spin (or composite neutral particles such as neutrons) will also have a magnetic dipole moment defined by the gyromagnetic ratio of the nucleus γ and the nuclear spin angular momentum operator $\hat{\boldsymbol{I}}$ as given in Equation 2.2.

$$\hat{\boldsymbol{\mu}} = \gamma \hat{\boldsymbol{I}}$$

Equation 2.2

NMR experiments begin by applying an external magnetic field (B_0) to a sample which by convention is aligned along the z axis. The interaction between spins and the field gives rise to the spin Hamiltonian operator expressed in Equation 2.3.

$$\widehat{\boldsymbol{H}}_{\boldsymbol{spin}} = -\hat{\boldsymbol{\mu}} \cdot \boldsymbol{B_0}$$

$$\widehat{\boldsymbol{H}}_{\boldsymbol{spin}} = -\gamma B_0 \hat{\mathbf{I}}_{\boldsymbol{z}}$$

Equation 2.3

The operator $\hat{\mathbf{I}}_{\boldsymbol{z}}$ represents the z component of the spin angular momentum operator. In this equation, γB_0 is defined as the Larmor frequency ω_0 discussed further below.

2.1.3 Spin ½ Nuclei

As stated above, the quantum number m of the nucleus has $2I + 1$ possible states. Spin ½ nuclei are of interest in most NMR experiments (Table 2.1), which results in two well defined spin states. The eigenfunction of the spin half nucleus in a z aligned external field is defined in Equation 2.5 [47]

$$\hat{\mathbf{I}}_{\boldsymbol{z}}\Psi_m = m\hbar\Psi_m$$

Equation 2.4

with eigenvalues:

$$m = \pm 1/2$$

Equation 2.5

When m is positive, spins are aligned with the external field and the nucleus is in a lower energy state denoted by $|\alpha\rangle$. Conversely, when m is negative, spins are aligned against the external field and the nucleus is in a higher energy state denoted by $|\beta\rangle$. The spin Hamiltonian operator for each spin state for a spin ½ nucleus can therefore be written as Equation 2.6.

$$\widehat{\boldsymbol{H}}_{\boldsymbol{spin}}|\alpha\rangle = \frac{1}{2}\hbar\omega_0|\alpha\rangle$$

$$\widehat{\boldsymbol{H}}_{\boldsymbol{spin}}|\beta\rangle = -\frac{1}{2}\hbar\omega_0|\beta\rangle$$

Equation 2.6

$|\alpha\rangle$ and $|\beta\rangle$ provide the basis pair of eigenstates for all possible states of spin ½ nuclei (Figure 2.1a) and have an energy difference of ΔE= $\left|-\frac{1}{2}\hbar\omega_0 - \frac{1}{2}\hbar\omega_0\right| = \hbar\omega_0$ (Figure 2.1a). This separation of energy levels of spin ½ nuclei in a magnetic field is termed nuclear Zeeman Splitting [48] and is fundamental for NMR spectroscopy which is the measure of energy sublevel splitting through spin interactions in the nucleus's ground state.

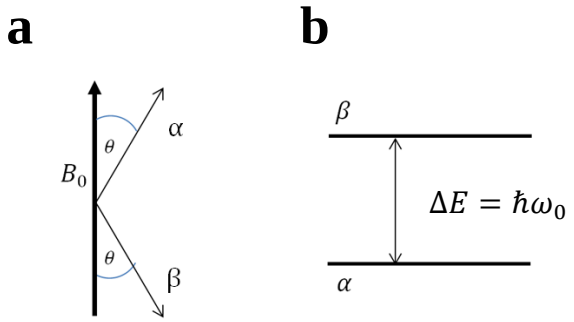

Figure 2.1 (a) is representation of high and low energy spin states, and (b) is energy diagram showing higher (β) and lower (α) energy levels.

Spin angular momentum can also be in a superposition state between both basis states [46]. For example, spins can be in the superposition states $|+x\rangle$ and $|-y\rangle$ which are well defined along the *x* or *y* axis ($\hat{\mathbf{I}}_x$ and $\hat{\mathbf{I}}_y$) shown in Equation 2.7.

$$|+x\rangle = \frac{1}{\sqrt{2}}|\alpha\rangle + \frac{1}{\sqrt{2}}|\beta\rangle$$

$$|-y\rangle = \frac{1}{2}(1+i)|\alpha\rangle + \frac{1}{2}(1-i)|\beta\rangle$$

Equation 2.7

2.1.4 Spin Precession

Substituting Equation 2.3 into the Schrodinger equation (Equation 2.1) reveals the following differential equation of motion:

$$\frac{\partial}{\partial t}|\Psi(t)\rangle = -\mathbf{i}\hbar\omega_0\hat{\mathbf{I}}_z|\Psi(t)\rangle$$

Equation 2.8

with solution:

$$|\Psi(t)\rangle = \exp(-\mathbf{i}\omega_0 t)|\Psi(t)\rangle$$

Equation 2.9

This describes the evolution of spins in the presence of a static external field and is equivalent to a clockwise rotation around the z axis at an angular frequency ω_0 in a classical description (discussed later). For spins in purely $|\alpha\rangle$ or $|\beta\rangle$ states this equates to a change in phase factor over time. Spin evolution in other states is best considered using spin ensembles and classical mechanics discussed in the next section.

2.1.5 Boltzmann Distribution

In reality, a sample will contain many spins and so ensembles of nuclear spin states are a more relevant consideration [49]. The expectation value of $\hat{\mathbf{I}}_z$is found by summing all states with probability p_Ψ as shown in Equation 2.10.

$$\overline{\langle\Psi|I_z|\Psi\rangle} = \sum_{\Psi} p_\Psi \langle\Psi|I_z|\Psi\rangle$$

Equation 2.10

In the case of spin ½ nuclei Equation 2.10 reduces to the difference between the basis states, shown in Equation 2.11.

$$\overline{\langle \boldsymbol{\Psi} | \boldsymbol{I_z} | \boldsymbol{\Psi} \rangle} = \frac{1}{2}(\overline{|\alpha|^2} - \overline{|\beta|^2})$$

Equation 2.11

This describes the population difference between nuclei in each spin state $|\alpha\rangle$ and $|\beta\rangle$ and is termed the polarization of the ensemble. The energy associated with the spin state is usually orders of magnitude less than the thermal energy, which results in a net polarization of effectively zero at room temperature when there is no magnetic field present. However, in the presence of a static magnetic field this small energy difference means that there will be a small tendency to align in a lower energy spin state $|\alpha\rangle$ which results in a net spin along this direction (polarization). This difference is the thermal equilibrium state of the spin ensemble, and is dependent on the Boltzmann probability factor. At room temperature using laboratory magnets the population difference in states will simplify to Equation 2.10.

$$\overline{\left| n_{\pm\frac{1}{2}} \right|^2} = \frac{1}{2} N \left(1 \pm \frac{\hbar \gamma B_0}{2 k_B T} \right)$$

Equation 2.12

where $n_{\pm 1/2}$are the populations of the $\pm 1/2$ spin states, N is the total number of spins, k_B is the Boltzmann constant and T is temperature [47]. This can be used to calculate the population difference ratio between both states of spin half nuclei (Equation 2.13).

$$\Delta \mathrm{n} = \left(\mathrm{n}_{+\frac{1}{2}} - n_{-\frac{1}{2}}\right) = \frac{\hbar \gamma B_0}{2k_B T}$$

Equation 2.13

The population difference of spin states is a key factor determining the strength of the NMR signal. In the presence of an external magnetic field the population difference between states is incredibly small (in most cases) and as such NMR is a comparatively insensitive measure.

During the application of a radio frequency (RF) pulse transverse magnetization is created through quantum coherence [46] and there will be a signal from inphase precession derived from the net population difference [50]. This can be more easily described using classical vector theory.

2.2 Classical Description

2.2.1 Magnetization Vector

In the presence of an external magnetic field (B_0) spin ensembles will produce a net magnetization vector M aligned with the field due to the small difference between populations of spin states described above. Spin ensembles will also precess around the external field which results in a rotational frequency of the magnetization vector around B_0. As with quantum spin state evolution (Equation 2.9), the rate of precession will depend on the gyromagnetic ratio of the nucleus and the strength of the magnetic field i.e. the Larmor frequency.

$$\omega_0 = -\gamma B_0$$

Equation 2.14

The equation of motion for nuclear magnetization on a macroscopic level can be found using the differential equation:

$$\frac{d\boldsymbol{M}(\boldsymbol{t})}{dt} = \gamma \boldsymbol{M}(\boldsymbol{t}) \times \boldsymbol{B}(\boldsymbol{t})$$

Equation 2.15

2.2.2 RF Pulse and B_1

A radio frequency (RF) pulse can applied to tip magnetization into the transverse plane. An RF pulse acts as a secondary oscillating magnetic field vector B_1 which, despite the fact that B_1 is usually much less than B_0, will have a cumulative effect by oscillating at the same frequency as spin precession (resonant frequency). Using a frame of reference that rotates at the frequency of the RF pulse allows for a much simpler analysis of this effect as the tipping of the magnetization vector can be viewed as a simple vector rotation around B_1.

Immediately following an RF pulse, M will be aligned at some angle from B_0 (a discussion of on and off resonance spins is given later). M will then precess around B_0 and give a net transverse magnetization oscillating at the resonant frequency.

2.2.3 T_1 and T_2 Relaxation

Over time, this transverse magnetization is lost as M relaxes back to thermal equilibrium under two processes – Longitudinal T_1 relaxation and Transverse T_2 relaxation.

Longitudinal magnetization relaxes back to its equilibrium state because absorbed energy from the RF pulse is dissipated into the sample lattice (also called spin-lattice relaxation). This causes the population difference to relax to thermal equilibrium as expressed and will follow an exponential recovery where T_1 is the longitudinal decay constant (Figure 2.2a).

The magnetization from spin states of adjacent nuclei will also interact to dephase precession until net transverse magnetization is completely destroyed (also called spin-spin relaxation). The decay in transverse magnetization will follow an exponential curve where T_2 is the transverse decay constant (Figure 2.2b).

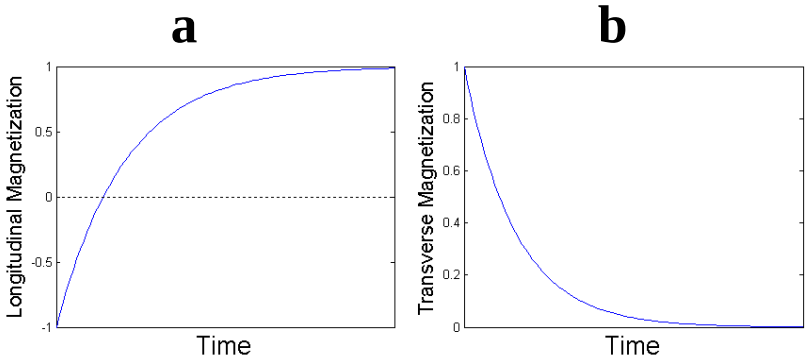

Figure 2.2 T_1 recovery of full inversion longitudinal magnetization (a) and T_2 decay of transverse magnetization (b).

In real life experiments the transverse relaxation is also affected by small variations and fluctuations in the external magnetic which means that there is faster dephasing and a quicker relaxation time, termed T_2^* decay. This will always be much shorter than T_2 and more accurately reflects signal decay in *in vivo* experiments.

Whilst T_2^* relaxation will dominate, a spin echo sequence [51] can be used to measure the actual T_2 by measuring the strength of the signal refocused with a π pulse. The spin echo sequence works by refocussing spins that have decayed under T_2^* relaxation. The πpulse will invert the transverse spins and result in a refocussing of static field effects causing dephasing of transverse magnetization. By repeating the spin echo with multiple spacings of the echo pulse and readout, T_2 can be calculated.

2.2.4 Bloch Equations

The Bloch equations [52] are equations that describe the macroscopic nuclear magnetization in a static magnetic field. They relate to Equation 2.15 and can include T_1 and T_2 relaxation to form the following differential equations:

$$\frac{dM_x(t)}{dt} = \gamma[\boldsymbol{M}(\boldsymbol{t}) \times \boldsymbol{B}(\boldsymbol{t})]_x - \frac{M_x(t)}{T_2}$$

$$\frac{dM_y(t)}{dt} = \gamma[\boldsymbol{M}(\boldsymbol{t}) \times \boldsymbol{B}(\boldsymbol{t})]_y - \frac{M_y(t)}{T_2}$$

$$\frac{dM_z(t)}{dt} = \gamma[\boldsymbol{M}(\boldsymbol{t}) \times \boldsymbol{B}(\boldsymbol{t})]_z - \frac{M_z(t) - M_{z\,eq}}{T_1}$$

Equation 2.16

where $M_{z\,eq}$ is the z aligned magnetization at thermal equilibrium.

Simple solutions to these equations can be derived to calculate the evolution of magnetization that is tipped to be at some angle from M_z with starting transverse magnetization along $M_x(0)$:

$$M_z = M_{z\,eq} + \big(M_z(0) - M_{z\,eq}\big)\exp(-t/T_1)$$

$$M_x = M_x(0)\cos(\omega_0 t)\exp(-t/T_2)$$

$$M_y = M_x(0)\sin(\omega_0 t)\exp(-t/T_2)$$

Equation 2.17

The transverse magnetization oscillates at the Larmor frequency until it is fully decayed under T_2 relaxation.

2.2.5 Flip Angle

The flip angle for a continuous wave RF pulse will be proportional to the strength and duration of the RF pulse:

$$\beta = -\gamma \int B_1(t)dt$$

Equation 2.18

Using a frame of reference that rotates at the RF frequency, on resonance spins will rotate around B_1 by an angle β in an anti-clockwise direction. Equation 2.18 shows that nuclei with greater gyromagnetic ratio will require RF pulses with lesser strength or duration to produce the same flip angle, and that the flip angle can be increased by applying stronger or longer pulses. However, this

increases the specific absorption rate (SAR) for *in vivo* studies and the profile of the RF pulse $B_1(t)$ which defines the bandwidth.

2.2.6 B Effective

The flip angle around perpendicular field B_1 expressed in Equation 2.18 will only hold for frequencies equal to the applied RF pulse at the centre of the spectral window (i.e. on resonance). This is because off resonant magnetization will precess at some rate faster or slower than the RF pulse. This effect is understood by considering the effect of B_1 in the reference frame rotating at the RF pulse frequency. A fictitious field arises due to the circularly accelerating frame of reference compared to the laboratory frame, which works against the external field (B_{fict}) leaving a resultant field $B_{res} = B_0 - B_{fict}$ (Figure 2.3). For on resonance magnetization (precessing at the frequency of the rotating frame) $B_{fict} = B_0$ and therefore experiences an unperturbed B_1 field as shown in Figure 2.3a. However, for off resonance frequencies where $B_{fict} \neq B_0$ there will be a resultant effective field B_{eff} some angle α from B_1 about which spins will rotate (Figure 2.3b). The angle α will depend on the magnitude of B_1 and B_{res} and can be found using simple vector analysis. The angle is minimised when $B_1 \gg B_{res}$ which can be achieved by using a high power RF signal to increase B_1. However, some nuclei will exhibit a large range of chemical shifts whereby B_{res} cannot be ignored and more advanced techniques must be employed.

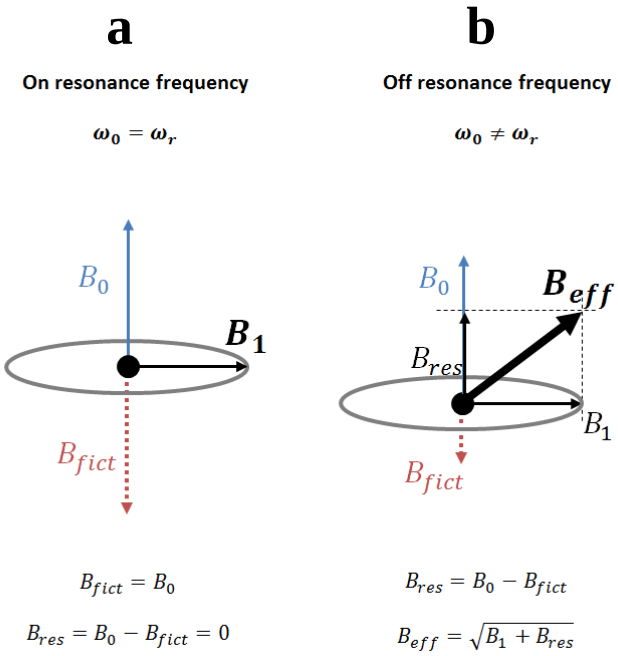

Figure 2.3 On resonance (a) and off resonant (b) spins.

2.3 NMR Signal

2.3.1 Free Induction Decay

The relaxing transverse magnetization signal from spins within the sample is measured through an induced current in a receiver coil which decays under T_2^* relaxation. Precessing transverse spin magnetization produces an oscillating current, called the free induction decay (FID, Figure 2.4).

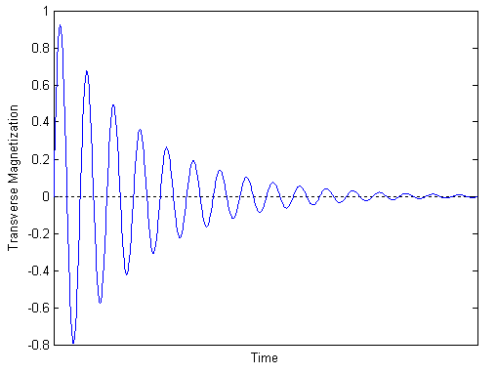

Figure 2.4 Simulated FID signal oscillating at the Larmor frequency and decaying under $\boldsymbol{T_2^*}$ relaxation.

Quadrature detection is used to determine the signal along the *x* and *y* axis (see Section 2.7.4) to produce the complex signal $s(t) = s_x(t) + is_y(t)$. This signal contains the superposition of all precessional frequencies in the rotating frame. After an RF pulse with flip angle β spins will produce an FID as follows:

$$M_0 \sin(\beta) \exp(i\Omega t) \exp(-t/T_2)$$

Equation 2.19

2.3.2 Fourier Transform

This FID signal contains all the frequency information needed for imaging and spectroscopy, and can be converted from the time to frequency domain using the standard Fourier transform algorithm [43] shown in Equation 2.20.

$$s(\omega) = M_{z\,\mathrm{eq}} \sin(\beta) \int_0^\infty \exp[(\, i(\Omega - \omega_0) - 1/T_2)t]\, dt$$

Equation 2.20

The Fourier transform produces a complex spectrum made up of real and imaginary components ($\mathfrak{L} = \mathfrak{R} + i\mathfrak{I}$) described in Equation 2.21, which produce the absorption ($\mathfrak{R}$) and dispersion ($\mathfrak{I}$) spectra shown in Figure 2.5.

$$\mathfrak{R}\big(S(\omega)\big) = M_0 \sin(\beta) \frac{1/T_2}{(1/T_2)^2 + (\Omega - \omega)^2}$$

$$\mathfrak{I}\big(S(\omega)\big) = M_0 \sin(\beta) \frac{\Omega - \omega}{(1/T_2)^2 + (\Omega - \omega)^2}$$

Equation 2.21

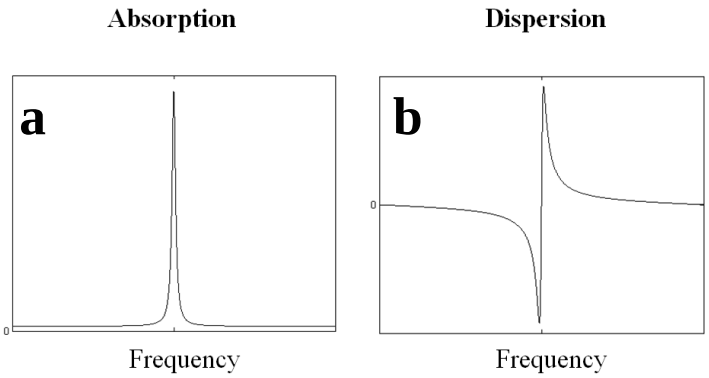

Figure 2.5 Absorption spectrum (a) and Dispersion spectrum (b).

The Fourier transform is generally calculated using a numerical algorithm called the fast Fourier transform. In most cases the absorption spectrum alone is displayed and used in analysis as it has a better resolution than the dispersion spectrum [46].

2.3.3 Signal to Noise Ratio

The strength of the NMR signal depends on three factors – the population difference between spin states, the strength of magnetization and the rate of precession. At thermal equilibrium the population difference of N spin ½

nuclei will be proportional to the energy gap between spin states $N\gamma B_0/T$; the strength of the precessing magnetization proportional to γ and the rate of precession equal to γB_0. NMR noise is roughly proportional to $(\gamma B_0)^{1/2}$ which leads to a SNR relationship shown in Equation 2.22[31]

$$SNR \propto \frac{N\gamma^{5/2}B_0^{3/2}}{T}$$

Equation 2.22

There is therefore a great advantage in using stronger magnets to increase B_0 and measuring nuclei with high natural abundance of spin ½ isotopes (increasing N) and with higher γ. More advanced pulse sequences can be used to enhance sensitivity by exploiting these factors.

In addition, signal will be enhanced by taking a number of averages to reduce the effect of noise. Whilst taking *n* averages will produce *n* times the signal, the noise will increase dependent on the error propagated through the variance such that the overall SNR will increase by $\sim\sqrt{n}$.

2.4 Magnetic Resonance Spectroscopy

2.4.1 Introduction

Within a sample there will be a range of spin frequencies which can be investigated using MRS. Spins precess at varying frequencies based on their chemical environment, providing the frequency bandwidth observable in MRS experiments. The source of this range of frequencies is produced by the interaction between the external magnetic field and surrounding electrons

(chemical shift) and the through bond interaction from spin states of neighbouring nuclei (spin-spin coupling) as shown diagrammatically on Figure 2.6.

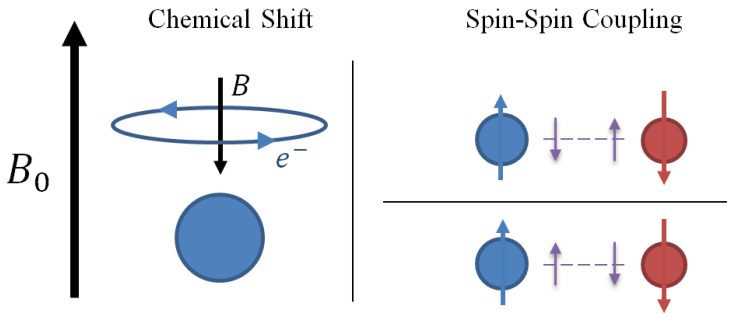

Figure 2.6 Illustration of chemical shift (a) and spin-spin coupling (b).

These variations in resonant frequency provide useful information about a sample as observed in the NMR spectrum, such as the position of nuclei within molecules and the distance of neighbouring nuclei. MRS can also be used to determine the quantity of specific substances within samples which is the basis of many *in vivo* studies [4, 11, 12].

2.4.2 Chemical Shift Scale

The separation of individual peaks is usually measured as chemical shift from some standard reference molecule (often TMS) and is measured on a scale of parts per million [45]. B_0 will induce a current in the electron cloud surrounding the nucleus which generates a small field which will oppose B_0via Lenz's law.

This results in the nucleus experiencing an effective magnetic field offset from the external magnetic field as defined below:

$$B = B_0(1 - \sigma)$$

Equation 2.23

where σ is a shielding factor.

Nuclei with greater neighbouring electron density will experience a greater shielding effect and their resonance will move up field in the spectrum (lower Larmor frequency). Conversely, if neighbouring bonded nuclei are electronegative then electrons are drawn away from the nucleus resulting in a deshielding effect (greater Larmor frequency).

Currents can also be induced in more complex molecules causing anisotropic chemical shift effects depending on the orientation of the molecule in the sample (Figure 2.7). Protons attached to mobile molecules will experience shielding or deshielding effects depending on the molecule's orientation with respect to the external field. The overall chemical shift will be the net shielding effect as a result of the combined shielding / deshielding. Alkenes, for example, have a dominant deshielding effect on attached protons when the double bond is perpendicular to the external field due to induced currents in the π electron orbitals, resulting in a net deshielding effect (Figure 2.7, Alkenes). By contrast, the triple bond in Alkynes has a dominant effect when parallel to the external field, resulting in a net shielding of attached protons (Figure 2.7, Alkynes). Protons attached to Aromatic rings, such as benzene, will experience

a dominant deshielding effect when the ring is perpendicular to B_0. A current is induced in electrons in the ring structure, which causes a shielding effect inside the ring and a deshielding effect outside the ring where attached protons are located (Figure 2.7, Aromatic Rings).

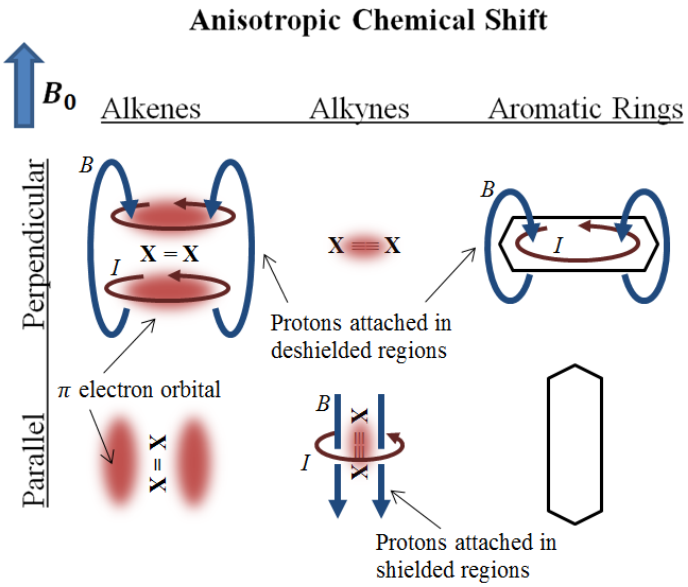

Figure 2.7 Chemical shift of Alkenes, Alkynes and Aromatic rings

The separation of individual peaks within the NMR spectrum is determined by the strength of the external magnetic field and hence varies depending on the field strength of the magnet. The following equation is used to calculate the chemical shift of the nuclei in ppm:

$$\delta = \frac{(\upsilon - \upsilon_R)}{\upsilon_R} \text{ ppm}$$

Equation 2.24

where δ is chemical shift, υ is the frequency of the nuclei, and υ_R is the frequency of a reference nucleus.

2.4.3 J-Coupling

Peaks within the MR spectra can also be split into multiple smaller peaks depending on their interaction with bonded spins through the bond pathway [31]. The nuclear spin resonances can split into doublets or multiplets, and also other more complicated patterns depending on the number of interacting nuclei as outlined in Figure 2.8.

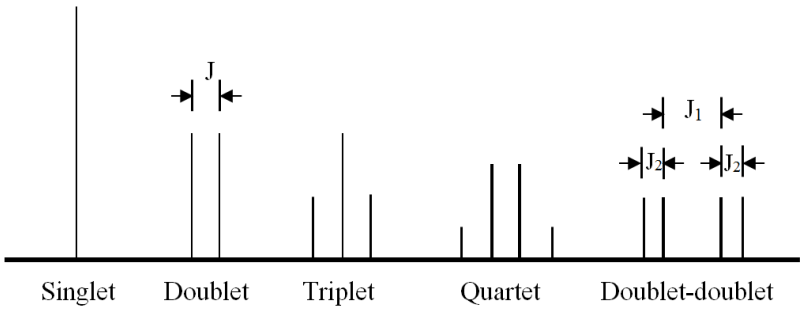

Figure 2.8 J Coupling of simple and complex coupled systems.

Peak splitting occurs as a result of a number of nuclei being spin coupled to each other. The magnetic interaction between a nucleus and local electrons causes a constant increase or decrease in energy. In an external magnetic field a simple non-coupled heteronuclear two spin system will contain four energy levels: ββ, βα, αβ, αα, (Figure 2.9). The energy between spin state transitions determine the frequency observed, which will be a singlet for each nucleus in this example (ν_1 and ν_2).

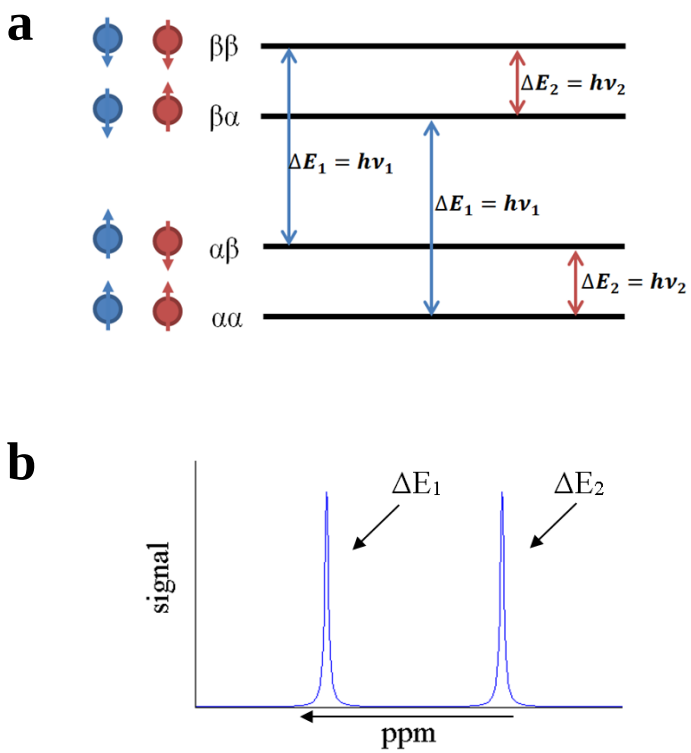

Figure 2.9 Energy diagram of a simple two spin uncoupled system (a) and corresponding spectrum (b).

The energy levels in this system will be altered if the spin states of the nuclei are coupled as transmitted through the electrons in the bond. When the electron spin is aligned with B_0 there is an overall lowered energy state, and the converse occurs when the electron spin is aligned against B_0. When nuclei are coupled the electron spin orientation is transferred between nuclei through the covalent bonds and Pauli's exclusion principle. Due to this principle, the spin state of the electron from one nucleus will be in the opposite spin state of the electron from the neighbouring nucleus. This is also transmitted over multiple bond pathways via Hund's rules (up to 3 bonds). The result is that the energy levels of the coupled two spin system will be perturbed depending on whether

the electron spin alignment is in a lower or higher energy state as shown in Figure 2.10.

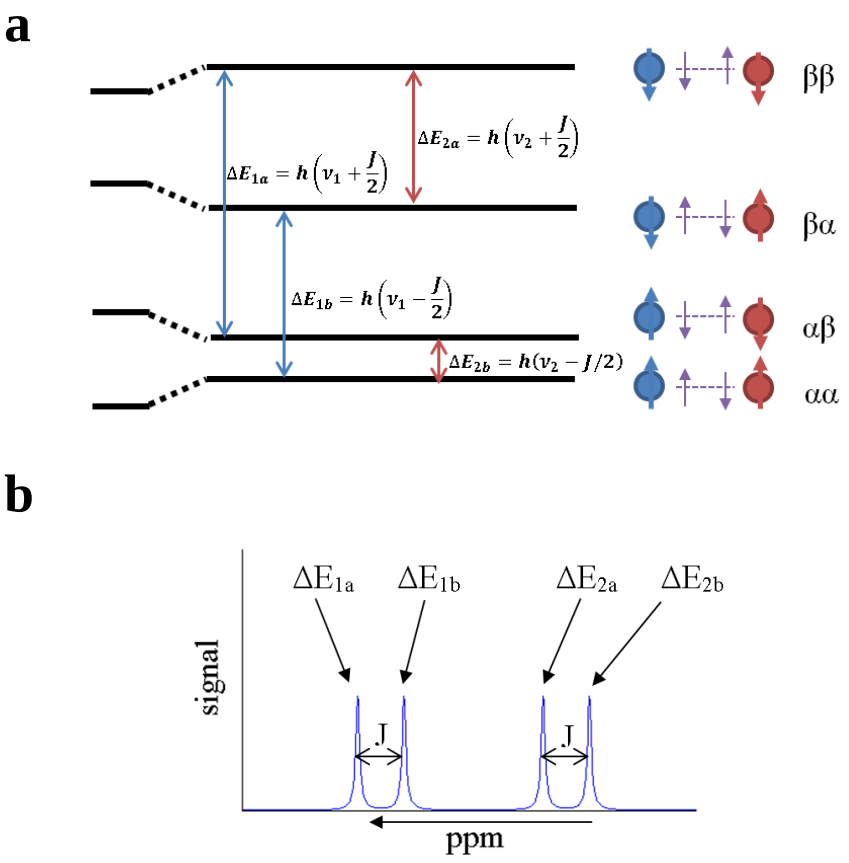

Figure 2.10 Energy diagram showing a simple two spin coupled system (a, compare Figure 2.9) and corresponding spectrum (b).

In this example, resonant frequencies corresponding to nuclear spin transitions are split, resulting in doublet peaks in the spectra (+J/2 and –J/2, Figure 2.10b). Given that approximately half the nuclei will be in each spin state (Equation 2.12) the signal intensity will be split by half for each doublet peak. The difference between peak positions is defined as the coupling constant J, and is measured in Hertz. This constant defines the frequency spacing between two

peaks, is independent of the strength of the external field strength and will be the same for both nuclei.

As the spin system becomes more complex, there will be greater multiplicity of peaks in the spectrum. Spectral peaks from nuclei coupled with two other nuclei will split into three frequencies, corresponding to the electron spin close to the nucleus being in the up up (↑↑), up down (↑↓), down up, (↓↑), and down down (↓↓) orientations. The energy levels for up down (↑↓) and down up (↓↑) will be equal, but there will be twice the number of transition pathways corresponding to this resulting in a 1:2:1 ratio of intensities for the triplet peak (Figure 2.8). As the number of attached nuclei increases, the number of peaks and relative intensities can be deduced using the same logic and follows Pascal's triangle for increasing splitting (1:1, 1:2:1, 1:3:31, 1:4:6:4:1 etc.). Split peaks may also experience further splitting resulting in multiple coupling constants (J_1, J_2 etc.) and more complex splitting patterns (doublet-doublets etc.).

Hetero nuclear J coupling can be destroyed by applying a continuous wave RF pulse at the frequency of the spins coupled to the nucleus of interest during acquisition. This acts to equalise the populations of the coupled spins and remove the through bond effects. Decoupling is an essential part of natural abundance ^{13}C MRS due to the low signal intensities which makes coupled peaks much harder to determine. These techniques require a dual coil design to operate at both the multinuclear frequency for excitation, and ^{1}H frequency for decoupling.

2.4.4 Localization

MRS is often acquired from a single voxel of interest within tissue using spectroscopic localization techniques, the most common of which are Point RESolved Spectroscopy (PRESS) and STimulated Echo Acquisition Mode (STEAM). Both techniques use three RF pulses applied alongside three magnetic gradient pulses in each direction in turn and rely on spin echoes (Section 2.2.3) as outlined in Figure 2.11.

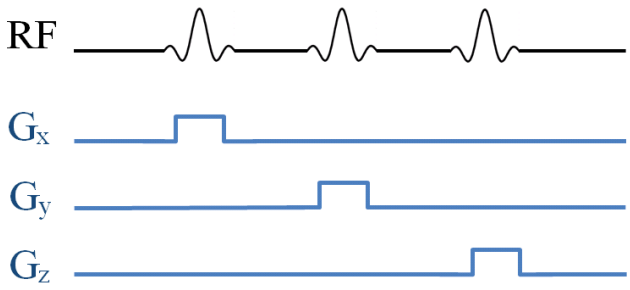

Figure 2.11 Representation of a PRESS or STEAM localised sequence. In both sequences the first pulse is a slice selective π/2 pulse, followed by two π pulses for PRESS or two π/2 pulses for STEAM.

PRESS uses three consecutive slice selective pulses with flip angles π/2 – π – π whereas STEAM uses three excitation pulses π/2 – π/2 – π/2. The first pulse applies a slice selective excitation (π/2) in one plane. For PRESS, each of the final two pulses results in a spin echo signal and after the final pulse the signal will be received from the intersection of the three orthogonal planes excited by the pulses. STEAM acquires the spin echo read out from the calculated effect of the final two π/2 RF pulse, which means that the spacing between the 3 pulses is important. The second π/2 pulse in STEAM moves spins back into the

z axis, which still contain coherences from the initial excitation pulse. This is then refocused by the final π/2 pulse. STEAM doesn't require as long a time between pulses because the signal does not need to be fully decayed after the first pulse or fully refocused after the second pulse, and so the echo time (TE) can be shorter compared to PRESS.

2.4.5 Surface Coils

Surface coils are used in some experiments to enhance the signal received from the sample. This is particularly useful for nuclei with lower sensitivity (e,g ^{13}C MRS). These sit on the surface of the subject and can be used to transmit and / or receive the NMR signal. Whilst in some cases surface coils are used in combination with localization sequences such as PRESS or STEAM (e.g. ^{31}P), for many *in vivo* application the spectrum is acquired without localization gradients in order to acquire signal from as large a region of tissue as possible, increasing the signal strength (e.g. ^{13}C MRS measurements of liver glycogen). Even without a localization sequence, surface coils provide some localisation (over a larger volume) due to the B_1 signal drop off which will only excite spins within a particular region of interest.

Surface coils cause B_1 field inhomogeneity within the field of view which can make quantification of substrate concentrations difficult as there will be a variation in flip angle (transverse magnetization) across the sample. These difficulties are explored in more detail in Chapter 4.

2.5 Magnetization Transfer

2.5.1 Introduction

Most MRI and MRS techniques excite the spin state of nuclei in order to measure the resultant signal form (FID). However, alternative techniques can be used to excite nuclei and measure the effect it has on neighbouring nuclei. For example, magnetization transfer considers the transfer of spin excitation between molecules in a sample.

2.5.2 CEST Effects

There has been recent interest in chemical exchange saturation transfer (CEST) and a number of studies have considered using this as a new magnetic resonance technique for exploring metabolism *in vivo* [53, 54]. CEST relies on the transfer of hydrogen nuclei between a chemical of interest and water, as shown in Figure 2.12. Commonly, a low power pre saturation pulse is applied at varying frequencies and the signal of the water peak is subsequently measured. As the saturation pulse frequency varies across the spectrum, the water peak will be saturated to varying degrees. A pre saturation pulse at the frequency of water will reduce the peak signal close to zero. When a pre saturation pulse is applied at the frequency of metabolites with exchangeable protons there will be a partial suppression of water signal due to the chemical transfer of saturated hydrogens to the water molecule.

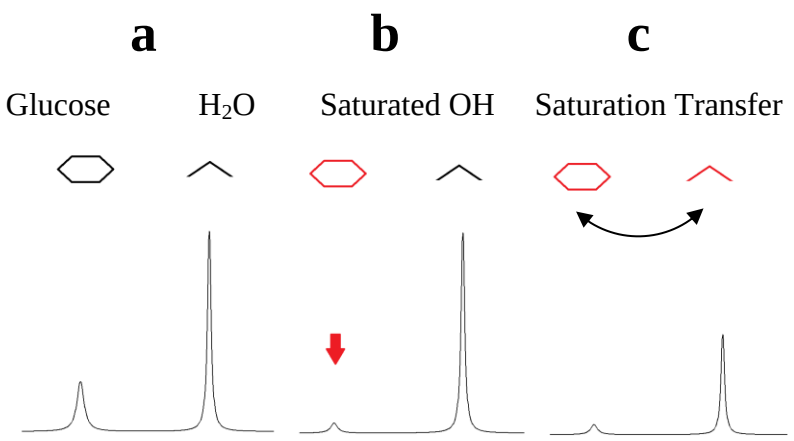

Figure 2.12 MR spectrum of glucose and water peaks (a) showing saturation transfer from glucose (b) to water (c) via chemical exchange.

Measuring the water peak signal over a range of pre saturation frequencies will produce the so called 'Z spectrum' (Figure 2.13a) which reveals a large central dip around the water saturation, and a smaller off resonance dip from chemical exchange. This can be plotted as the magnetization transfer asymmetry (MTR_{asym}) defined as the water signal difference between negative offset frequencies and positive offset frequencies (Figure 2.13b).

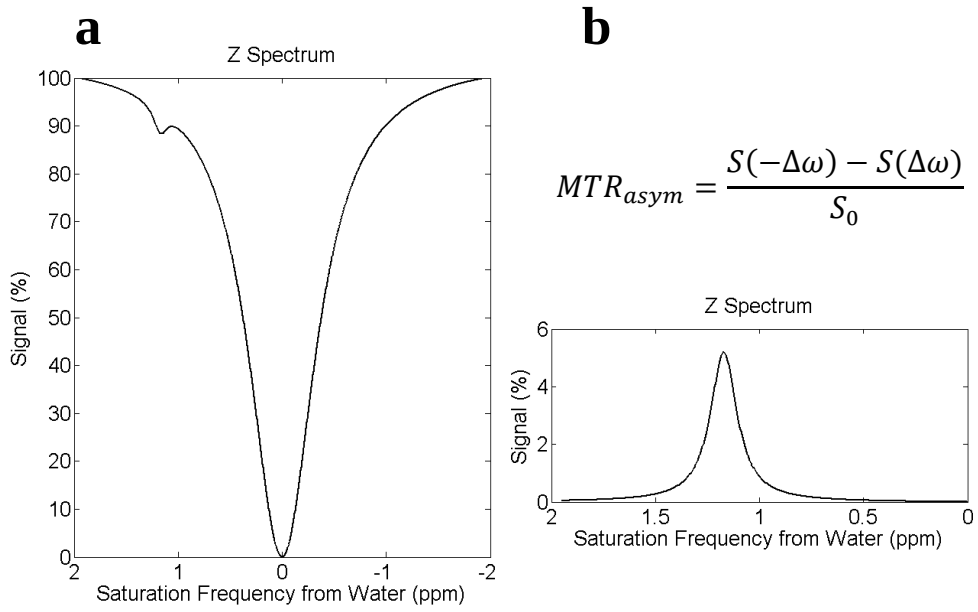

Figure 2.13 Representative Z spectrum (a) showing asymmetry of water peak when exchangeable protons are saturated, and corresponding $\boldsymbol{MTR_{asym}}$ equation and plot (b).

The advantage of using CEST is that it acts as a sensitivity enhancement mechanism where low concentration solutes can be investigated through the solvent signal [55]. The CEST effect is observed in some cases where temperature of the sample (e.g. *in vivo*) does not allow for standard MRS techniques due to the increased chemical exchange at higher thermal energies. CEST can be used with standard MRI techniques to map out metabolite concentrations using saturation pre pulses.

2.5.3 Non CEST Effects

Despite the advantages of CEST techniques, it has become apparent in the literature that there are multiple contributions to the Z spectrum that include non CEST effects. In particular, other saturation transfer effects have been

discovered that contribute across the Z spectrum and upfield of water – namely magnetization transfer contrast effects (MTC) and cross relaxation through the Nuclear Overhauser effect (NOE). MTC occurs due to the effects of semi-solid tissues and cause a strong broad asymmetric effect $MTR_{asym}^{MTC}(\Delta\omega)$ [56] whereas NOE causes more narrow peaks in the Z spectrum up field from water $MTR_{asym}^{NOE}(\Delta\omega)$ [55]. The upfield NOE peaks have been attributed to aliphatic and olefinic protons ranging from 0 – 5 ppm in the ^{1}H MR spectrum and result in cross relaxation of the water peak found in the -5 to 0 ppm range in the Z-spectrum [53]. Given these extra components of saturation transfer, the magnetization asymmetry can be described as the result of the combination of three separate factors:

$$\boldsymbol{MTR_{asym}(\Delta\omega) = MTR_{asym}^{CEST}(\Delta\omega) + MTR_{asym}^{MTC}(\Delta\omega) + MTR_{asym}^{NOE}(\Delta\omega)}$$

Equation 2.25

as defined by Jones *et al* [57]. These extra saturation transfer effects complicate the analysis of CEST effects for *in vivo* studies. Some have attempted to model the various contributing effects to separate the MT and CEST effects [58] whilst others have fitted an inverse Lorentzian curve and measured the difference of the Z spectrum from this curve [57]. As such, the magnetization transfer ratio can be defined as the Lorentzian difference (LD):

$$LD(\Delta\omega) = LF(\Delta\omega) - {}^{S(\Delta\omega)}/_{S_0} = MTR(\Delta\omega)$$

Equation 2.26

where $LF(\Delta\omega)$ is the Lorentzian fit over the Z spectrum baseline (defined in the regions of no asymmetry) [57]. This equation provides a simple method of estimating the magnetization transfer at varying frequencies without the added complications of NOE peaks on the opposite side of CEST metabolites.

Chapter 6 explores using CEST alongside ^{1}H MRS in a novel technique named 'spectroCEST' as a way of measuring hepatic lipid and glycogen levels during a single scan session.

2.6 Pulse Shape and Gradients

2.6.1 Amplitude Modulation

The excitation profile of a pulse across a bandwidth can be approximated by Fourier transform [31]. A simple rectangular pulse of constant power and frequency through time period t_p yields the excitation profile of a standard Sinc function ($sin(x)/x$) with peak excitation in the centre of the spectrum window of width $1/t_p$. A long duration, low power pulse yields a selective excitation at the centre of the spectral window, whereas a short duration high power pulse broadens the central excitation region so that there is only little loss towards the edges of the window (Figure 2.14).

Long duration low power selective excitation:

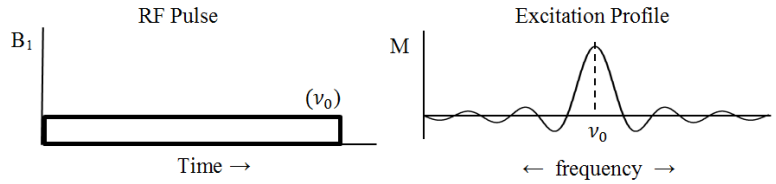

Short duration high power broad excitation:

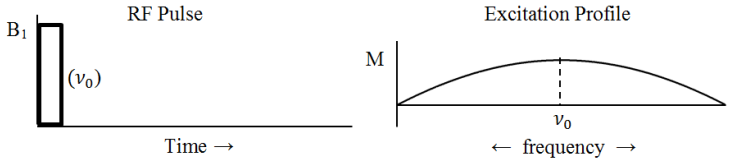

Figure 2.14 Excitation for varying length and power block pulses.

To generate equal excitation across the whole spectral width by using an amplitude modulated (AM) Sinc pulse, or Gaussian pulses can also be used.

2.6.2 Frequency Modulation and Adiabaticity

Another way of exciting a broad range of chemical shift frequencies fully into the transverse plane, or full inversion, is to use an adiabatic pulse [59]. These pulses use frequency and amplitude modulation to vary B_{eff} (Section 2.2.6) and provide a constant excitation across a defined bandwidth. The angle of B_{eff} from B_0 is varied by modulating the amplitude of B_1 or the frequency of the RF pulse ω_{RF} (Figure 2.15). If B_{eff} is moved from $+z$ towards $-z$ at a slow enough angular rate ($d\alpha/dt$) then the magnetization will remain aligned with B_{eff} and be moved through the transverse plane to finally be inverted.

To achieve this the adiabatic condition must be satisfied (Equation 2.27).

$$K(\Omega, t) = \left|\gamma B_{eff}(t)/\dot{\alpha}\right| \gg 1$$

Equation 2.27

Alternatively stated, the rate of rotation of B_{eff}needs to be much slower than the effective Larmor frequency in the rotating reference frame. Using a second frame of reference which rotates in the $B_1 B_{res}$ plane and follows B_{eff}, there will be a fictitious field $(d\alpha/dt)/\gamma$ acting perpendicular to B_1 resulting in an effective field E at angle ε from B_{eff} (Figure 2.15).

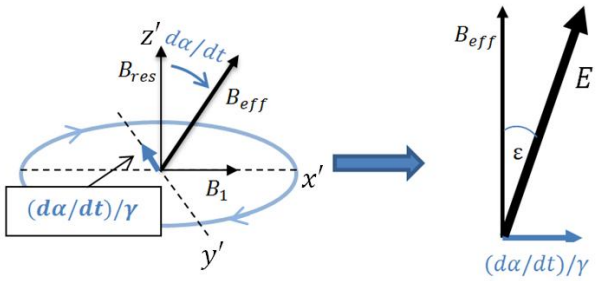

Figure 2.15 Slowly varying the RF frequency causes spins to precess around **E** and tip along with $\boldsymbol{B_{eff}}$ in the rotating frame ($\boldsymbol{x'y'z'}$).

Magnetization along B_{eff}precesses about E and is moved along with B_{eff}so that the net sweep angle of B_{eff} becomes the magnetization's flip angle [59]. The adiabatic half passage (AHP) and full passage (AFP) pulses describe pulse shapes with flip angles of $\pi/2$ and π respectively. These pulses can be used to increase the magnetization over a range of B_1 and provide a more uniform excitation across the bandwidth. Adiabatic pulses consist of an amplitude

modulation function $F_1(t)$ and frequency modulation function $F_2(t)$ which work in combination to achieve adiabaticity according to Equation 2.27. An example of such a pair often used is $F_1(t) = \mathrm{sech}(\beta t)$ and $F_2(t) = \tanh(\beta t)\,/\tanh(\beta)$ known as the hyperbolic secant (HS) pulse which works to significantly increases transverse magnetization across the spectral bandwidth compared with a similar duration rectangular pulse of similar power. This is simulated and explored in Section 4.3.

2.6.3 Gradients

Gradients can also be used in MRS techniques. They are used for spatial localisation in such technique as PRESS or STEAM (Section 2.4.4) and also to temporarily or permanently destroy unwanted signal. Different spins along the gradient axis G_z will experience a different external field and precess at a different rate according to Equation 2.28.

$$\omega_g = -\gamma z G_z$$

Equation 2.28

When applied across a sample, spins along the gradient axis will begin to dephase until eventually all spins will be out of phase and the net transverse magnetization across the sample will equal zero (Figure 2.16). Although the net signal is zero due to dephasing there is still transverse magnetization which can be refocused at a later time. For example, sandwiching a π pulse between two equal strength and duration gradients will produce a gradient spin echo whereby all peaks in the spectrum are fully dephased after the first gradient to be fully restored after the second. Because precession is also proportional to γ,

gradients can be used in carefully designed heteronuclear pulse sequences to dephase specific signal whilst retaining others.

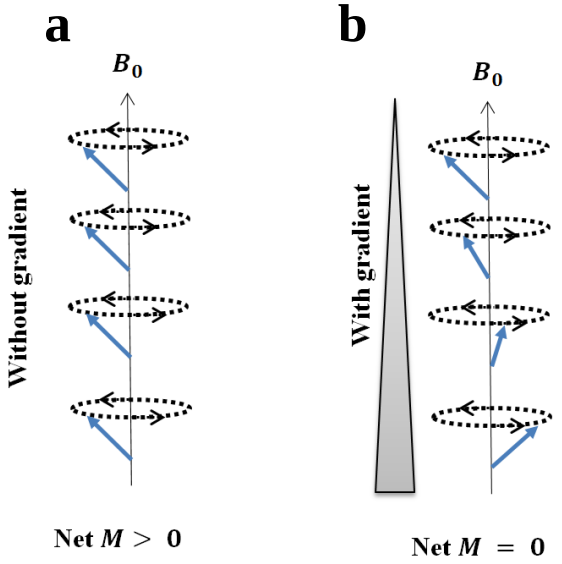

Figure 2.16 Without a gradient excited spins precess in phase and produce a net signal (a) whereas a field gradient moves spins out of phase and net signal is zero (b).

2.7 Instrumentation

2.7.1 Introduction

Magnetic Resonance instrumentation can vary depending on the sample (human, animal or chemical) and also setting (clinical or research). Whilst these variations are usually related to size, field strength, spectrometer and gradient design, similar setups are required throughout. The NMR instrumentation can be divided into four major components: the magnet, the RF transmission system, the signal receive system and the gradient coils. MRI scanners and NMR systems have developed considerably since their inception,

and are now regularly used in clinical and research settings. Advances in technology and computational ability have allowed for quicker scanning and produce higher quality images and spectra - with greater signal to noise ratios and higher resolution (better shimming). A basic schematic of the setup is shown Figure 2.17 [31, 46] and the four main components are outlined in the following sections.

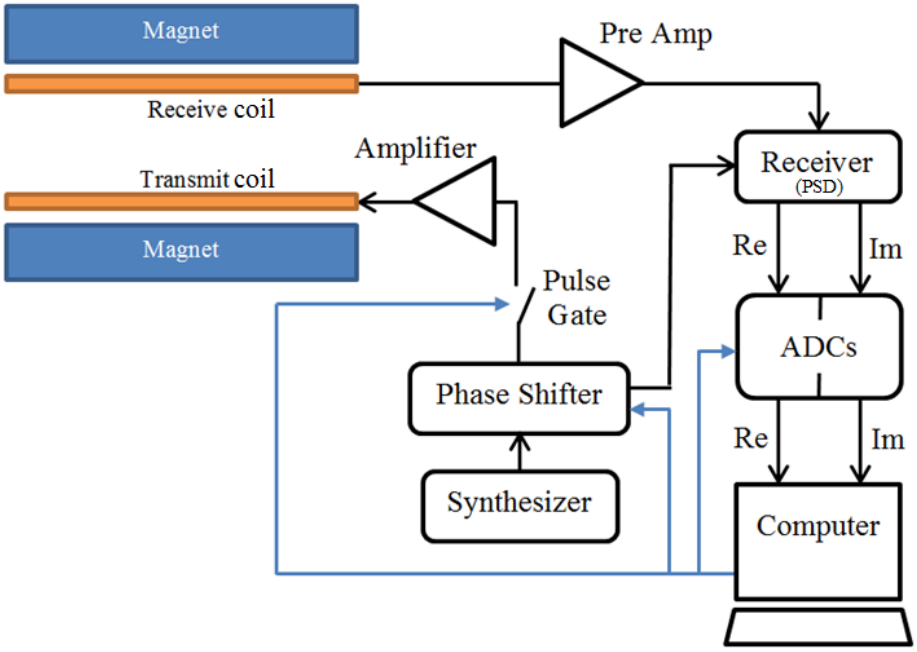

Figure 2.17 Simplified overview of a single (RF) channel MR system (gradient coils not shown). Blue arrows represents user input control and black arrows represent flow of pulses / signal.

2.7.2 Magnet

As described previously, the magnetization vector of a nucleus will oscillate at a rate defined by the gyromagnetic ratio and the magnetic field strength ($\omega = -\gamma B_0$). Given that the signal strength is proportional to the Larmor

frequency, increasing the magnetic field strength B_0 also increases the signal strength. A high field magnet sits at the heart of all MR systems.

In order to receive a constant signal it is crucial for there to be a highly stable magnet that will give a consistent field strength. Presently, most scanner systems achieve this by using a super conducting coil cooled using cryogens which provides resistance close to zero and allows a steady current flow without the need for external power. However, liquid Helium needs to be continually supplied to the system often by a refrigeration unit on the magnet. Early human scanners provided field strengths of less than 1.5T, whereas modern scanners have been built up to 9.4T but are regularly used in research at 3T or 7T.

B_0 field homogeneity is essential in the NMR experiment. Small variations in field strength will result in a perturbed Larmor frequency which will broaden the line width of resonant signals. This becomes particularly relevant in spectroscopy where peaks can have a small separation and greater line widths would result in a lower resolution and overlapping peaks. The homogeneity of the external field is optimised by using shim coils that work to counteract naturally occurring inhomogeneity. The aim of these coils is to match the B_0 variation function with an inverse function in order to oppose the effects. Whilst this can be done manually, most modern human scanning systems apply automatic shim corrections which employ various methods to measure the inhomogeneity that needs to be corrected. [31] .

2.7.3 RF Transmission Section

Modern scanners are controlled by a computer, which is used to control the transmission of RF pulses and also reception of the NMR signal. During RF transmission, the pulse frequency, phase and amplitude are defined (alongside any gradients) and sent to the transmitter coil through various stages (Figure 2.17). Firstly, an RF synthesiser generates the RF pulses at the reference frequency, which is then manipulated by a phase shifter using the user defined inputs. The phase shifters are used to adjust the phase of inputted pulses and can be used to remove artefacts through phase cycling. The resulting RF pulses are sent as small pulse packets with user defined pulse shapes to the transmission coil positioned close to the sample. The waveform is first passed through an RF amplifier to produce a high amplitude RF wave to be sent into the transmission coil (a pulse gate, controlled by the computer, is often used to connect the coil to the amplifier Figure 2.17). The amplification must be limited by the maximum SAR allowed for the tissue which needs to be carefully calculated (usually automatically by the system) to ensure safe levels of energy deposition (usually done before the sequence is implemented). The amplitude is also determined by pulse shapes inputted by the user. The final outcome is to produce an RF pulse at the reference frequency which is used to excite magnetization from equilibrium in order to produce the NMR signal [46].

2.7.4 Receiver Section

After excitation, nuclei will relax back to equilibrium (under T_1 relaxation) whilst precessing at the Larmor frequency (plus any chemical shift) which will

produce an oscillating transverse magnetization decaying under T_2^* relaxation. This is what is recorded as the NMR signal, as described previously. The NMR signal induces an oscillating current in the receiver coil, the FID (Section 2.3.1). However, this signal measured from the sample will be very small and first needs to be amplified to a usable level. The signal is run through a preamplifier close to the receiver coil in order to reduce any noise accumulation which would also be amplified at the pre amp (minimising the distance minimises electrical noise). The signal must then be converted into a digital format for analysis and interpretation, which is performed at the ADC. In older systems the receive signal was mixed with the reference RF pulse which centred the spectral bandwidth at this frequency. Newer systems are able to sample at a much greater frequency and will modulate the signal directly to centre the bandwidth on resonance. The new frequencies within the FID now oscillate at a frequency relative to the RF pulse frequency (Ω_0). One of the problems with this down-conversion of the NMR signal is that positive and negative frequencies (relative to the reference frequency) cannot be distinguished from each other, which means that downfield and upfield peaks overlap and may be plotted at the wrong chemical shift. This is overcome using quadrature detection, which for older systems was achieved by mixing the signal with the RF pulse in phase and out of phase by π, but for newer systems is done by mixing the signal with two digital signals out of phase by π. From this two signals are received, referred to as the real and imaginary signals discussed in Section 2.3.1. These are then combined to determine the positive and negative frequency signal and can also be used to adjust the phase of the spectrum.

The receive signal will also contain a phase factor which may be a result of phase shifts produced in the amplifiers and filters [47] and introduce artefacts into the spectrum. These can be overcome by cycling through a number of phases of the transmitted pulse and receiver. These phase cycles can be set up to cancel out unwanted phase shifts whilst maintaining the FID signal [45].

The Real and Imaginary components of the signal are fed individually into an ADC. The ADC works by measuring the voltage of the signal at regular consecutive time points. The time between sampling points is known as the dwell time, and the number of points obtained will correspond to the spectral resolution and is limited by the Nyquist rate of sampling (below which frequencies are indistinguishable and aliasing occurs). The total acquisition time is the product of the dwell time and the number of samples.

It should be noted that the transmission and receiver sections described here apply to a simple single channel system. Many modern systems use multichannel transmission and reception which follows similar processes but multiplied over a number of channels for faster acquisition, greater signal and more controlled B_1.

2.7.5 Gradient Coils

The NMR signal will contain a range of frequencies determined by chemical shifts and J coupling effects across a spectral bandwidth (Section 2.4). Spatial localization is achieved by using gradient coils which result in a spatially dependant frequency range (Section 2.6.3). These coils work to apply an external B_0 field gradient which will result in a spatially varying Larmor

frequency. This can be applied in each of the orthogonal directions to give the exact position of the received signal. For example, if the B_0 field is defined in the z direction and $\hat{\boldsymbol{\imath}}$, $\hat{\boldsymbol{\jmath}}$ and $\hat{\boldsymbol{k}}$ are unit vectors in the x, y and z direction respectively, a spatially varying gradient G will modify the B_0 field at position **r** according to

$$B(\boldsymbol{r}) = B_0\hat{\boldsymbol{k}} + G_x x\hat{\boldsymbol{\imath}} + G_y y\hat{\boldsymbol{\jmath}} + G_z z\hat{\boldsymbol{k}}$$

Equation 2.29

Gradient coils are set up so that a current will produce a spatially varying field which acts to modify B_0as shown in Figure 2.18.

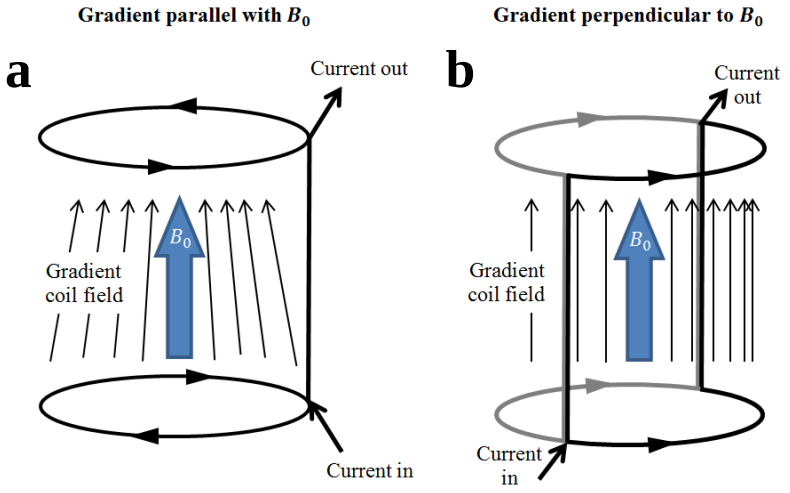

Figure 2.18 Gradient coils produce a spatially varying field in the $\boldsymbol{z}$ direction (a) and in the $\boldsymbol{xy}$ direction (b). The gradient coil field (black arrows) superimpose on the B_0 field from the magnet (blue arrow)

The pulse programmer (computer) sends a digital signal which is converted to an analogue voltage using a digital to analogue converter (DAC). This signal

may be a simple ramping up, followed by a constant gradient, followed by a ramping down. In some cases more complex gradient pulses are required, such as with echo planar imaging (EPI) where the gradient is switched between positive and negative consecutively. A gradient driver amplifier is then used to produce the well-controlled current used to generate the field gradient [46].

The field gradient and RF transmission often work in close connection, for example in slice selection and single voxel spectroscopy (SVS). In some cases the gradient coils can be used for purposes other than localization, such as dephasing / rephasing signal or decoupling coupled nuclei to enhance signal (Section 2.6.3).

2.7.6 Surface Coil Hardware

Surface coils are often used in *in vivo* NMR spectroscopy experiments which provide an enhanced signal due to proximity to the sample tissue (Section 2.4.5). The simplest setup for a surface coil is a single loop LRC circuit in which resonant frequency can be found by adjusting the inductor or the capacitor. This process is called ‘tuning’ and can be done manually or automatically depending on the system. In order to minimize the power transmitted to the coil the impedance of the coil needs to be matched to the impedance of the transmission line (called ‘matching’) which can also be done manually or automatically on modern systems. Surface coils can be used in the transmission or receiver systems, or as is often the case, for both transmit and receive.

Surface coils optimized for specific nuclei may also have integrated coils that operate at other frequencies for the purpose of acquiring scout images (^{1}H coil) or for heteronuclear decoupling. One example of this is the surface coil used in this thesis which was produced by PulseTeq (Surrey, UK) and consists of a 14 cm diameter single loop ^{13}C coil with ^{1}H quadrature decoupling coils (Figure 2.19) for use in conjunction with the Philips Achieva 3T body scanner (Philips, Best, The Netherlands) [25, 60]. Quadrature coils are located perpendicular to each other so that transmit / receive signals are out of phase by this amount, which provides increased decoupling.

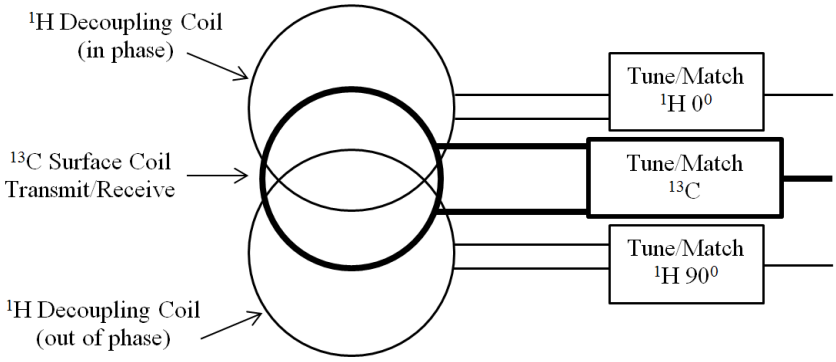

Figure 2.19 Surface coil schematic used for *in vivo* ^{13}C MRS studies. ^{1}H decoupling coils are set to produce and receive quadrature signal

2.8 MR Safety

In Vivo MRI and MRS uses non ionising radiation at RF frequencies which significantly reduces the risk when applied to biological tissue compared to

alternative radiation techniques. However, there are a number of safety issues which need to be considered in MR applications.

Firstly, the static magnetic field B_0 uses a powerful magnet in order to polarise the sample. This field will attract ferrous metal objects which may become dangerous as they are propelled in the field. All loose objects of this kind should be removed before entering the scanner hall. Likewise, if subjects have any pacemakers or implants (e.g. cochlear implants) these can become particularly hazardous. This consideration should be made for all objects that may need to be brought near the scanner in the case of an emergency, such as fire extinguishers, which need to be constructed from nonmagnetic materials.

Secondly, RF radiation can result in excess heating through induced currents. This may apply to non-ferrous metal objects also and as such all cables and surface coils should be carefully examined and built appropriately. It is important that pulse sequences are tested and that the absorption of energy in the tissue is calculated (SAR levels). This is done automatically in the Philips Acheiva 3T scanners used in this thesis, but new sequences should be checked manually also. Pads should be used to stop cables coming into direct contact with skin, and fixed metal implants in areas of high RF radiation should be avoided.

Thirdly, gradient switching can result in a high audio output and noise can reach damaging levels. Subjects placed in the scanner should wear appropriate noise protection gear and ear plugs. Fast gradient switching can also induce peripheral nerve stimulation during some sequences. There are not any known

long term risks associated with this, but it can make subjects uncomfortable. None of the sequences used in this thesis caused peripheral nerve stimulation.

Finally, there may be a number of psychological risks associated with the scan routine. For example, some people are claustrophobic and struggle to spend any length of time in the scanner. These factors are usually eliminated by screening subjects and excluding any who would not be appropriate for scanning.

2.9 Conclusion

In conclusion, the nuclear spin state of spin ½ nuclei allow researchers and clinicians to probe into biological tissue and examine related parameters. A strong static field is used to polarize spin ensembles in the sample and an applied RF pulse can excite spins states to produce transverse magnetization. As the precessing spins relax to equilibrium a current is induced in a receiver coil and used to elucidate structural and metabolic information about the sample. Gradient coils are used to localize spectra, or destroy unwanted signal. In particular, for this thesis, MRS can be used to measure the concentration of specific metabolites and explore basic liver physiology (Chapter 1). In addition to ^{1}H MRS for liver lipid measurements, surface coils can be used to acquire ^{13}C and ^{31}P MRS in order to measure glycogen and ATP levels.

Chapter 3 Hepatic Metabolism

This chapter provides a brief overview of the theory behind metabolism in the liver. The four main pathways of energy metabolism are described and details of the two primary energy stores, glycogen and lipids, are given. Finally, the role of ATP as the energy currency for all cells is considered.

3.1 The Liver

The human liver is the largest organ inside the body and performs a number of crucial functions. As can be seen from Figure 3.1 it sits just below the heart and extends down to the transverse colon. It can be divided into the right and left lobes and is made up of 60-75% of the same type of cells, namely hepatocytes.

The portal vein runs through the liver and absorbed nutrients from the intestines are transported into the many blood vessels and capillaries running throughout the liver mass. Whilst the liver performs many functions, including hormone production and detoxification, this Chapter focuses on its role in metabolism and energy storage. Nutrients derived from dietary food are transferred into hepatocytes either through active transport or diffusion, where they undergo various metabolic processes. The two primary forms of energy storage in the liver are glycogen and lipids.

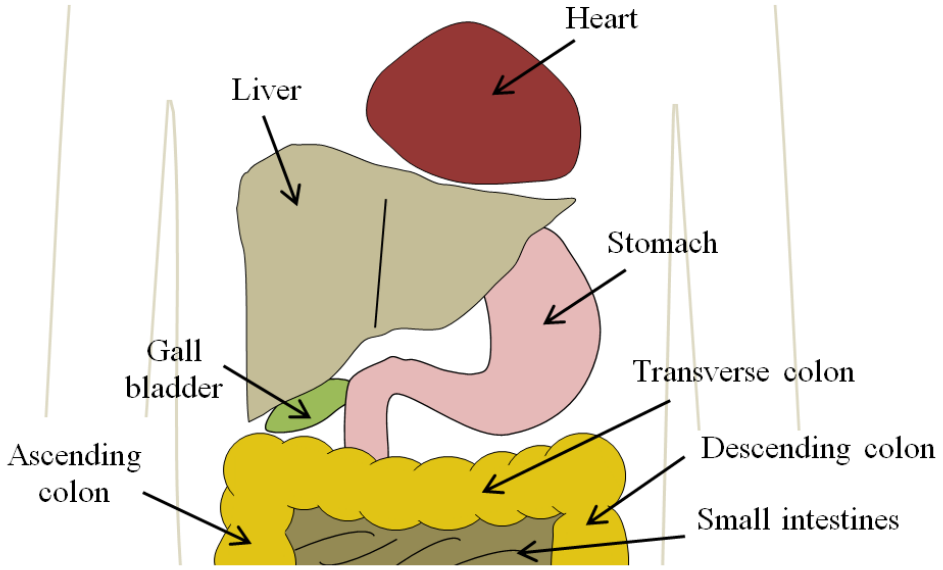

Figure 3.1 Illustration of the abdominal region showing the liver (left and right lobes), the stomach, the colon and the small intestines.

3.2 Metabolism and Energy Storage

3.2.1 Introduction

Energy for the human body is derived from dietary food which is absorbed and either used in cells or stored primarily in the liver as glycogen and triglycerides, or in adipose tissue. Dietary intake is metabolised to yield ATP which is used as the fuel of the vast majority of physiological processes. The liver plays a principle role in the metabolism and storage of these energy sources, as well as the regulation of output for energy demand. As such nutrients absorbed in the small intestines are first transported to the liver through the portal vein before flowing to the rest of the body. The major metabolic pathways active in the liver are glycolysis / gluconeogenesis,

glycogenesis / glycogenolysis, fatty acid synthesis / β oxidation, and the tricarboxylic acid (TCA) cycle.

3.2.2 Overview

An overview of the metabolic pathways in liver cells are seen in Figure 3.2

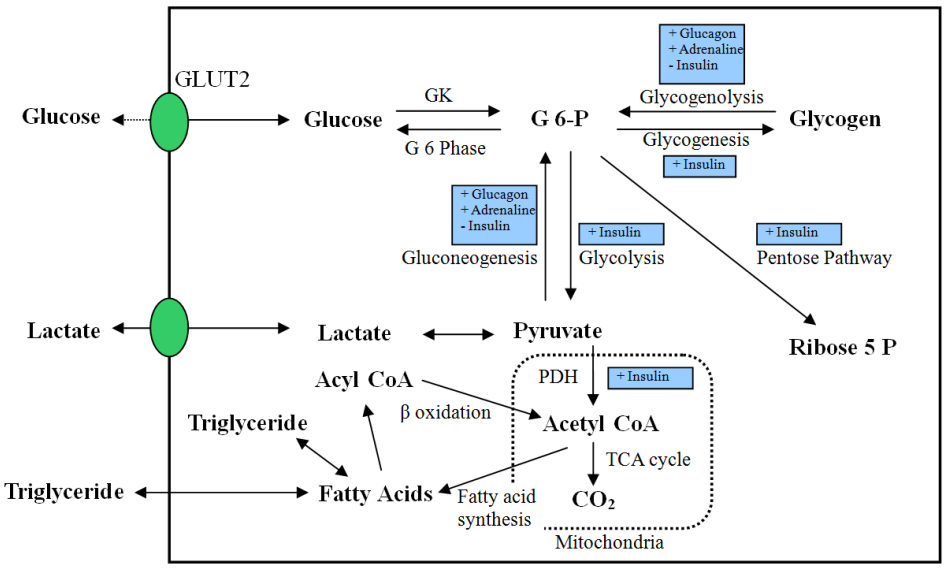

Figure 3.2 Overview of the metabolic processes in hepatocytes. GK is glucokinase, G 6 Phase is glucose 6-phosphatase, G6-P is glucose 6-phosphate, Ribose 5 P is ribose 5-phosphate, PDH is pyruvate dehydrogenase.

Glucose and other monosaccharides are transported from the portal vein into the liver (via transporter molecules) where they are either built up into glycogen (glycogenesis) or converted into pyruvate (glycolysis) which produces ATP and is also later used in another process to produce more ATP (TCA cycle). Triglycerides are broken down into fatty acids before moving into the liver, where they are either repackaged as triglycerides and stored or

converted into Acetyl CoA (β oxidation) for use in the TCA cycle. Acetyl CoA can also be converted back to fatty acids through fatty acid synthesis. The four main metabolic processes are explored in more depth below.

3.3 Glycolysis and Gluconeogenesis

Carbohydrates are polysaccharides made up from smaller units, and provide the major short term energy source in human diets. Dietary Carbohydrates are broken down in the stomach and small intestine into monosaccharides (e.g. glucose, fructose, Figure 3.3) where they are absorbed and transported through the blood stream first to the portal vein, and then throughout the body.

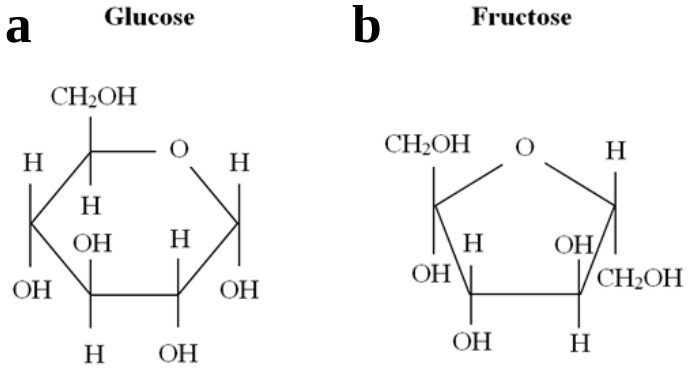

Figure 3.3 Chemical structure glucose (a) and fructose (b).

From the portal vein they are moved into liver cells via transporter molecules (e.g. GLUT2) as shown in Figure 3.4. Glycolysis occurs in most tissues to produce ATP for energy demands. For the first few stages of glycolysis (investment stage) there is a consumption of energy (ATP to ADP) as glucose is phosphorylated to form glucose 6-phosphate, and then fructose 6-phosphate is further phosphorylated to form fructose 1,6 biphosphate. The second half of

glycolysis (pay off stage) consists in converting phosphorylated molecules into pyruvate. Throughout the whole glycolysis process one monosaccharide molecule produces two pyruvate molecules and there is a net production of two ATP molecules (two molecules used during investment stage, and four molecules produced during pay off stage). Whilst this is the primary catabolic pathway, many of the intermediate metabolites are also extracted and used in anabolic pathways, including lipid metabolism, the TCA cycle and gluconeogenesis (discussed later).

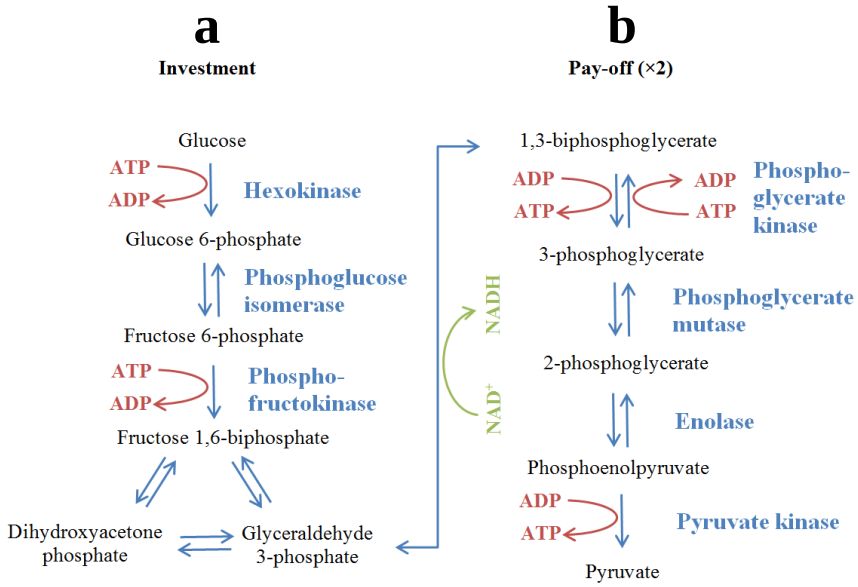

Figure 3.4 Glycolysis pathway. Investment (a) and payoff (b) phase.

The final product of glycolysis is pyruvate which is further decarboxylated via the enzyme pyruvate dehydrogenase (PDH) to generate Acetyl-CoA which enters the TCA cycle to supply more energy (Section 3.6).

For most tissues, the initial phosphorylation process prevents absorbed monosaccharides from leaving the cell. However, in liver tissue glucose 6-

phosphate can be converted back to glucose via the enzyme glucose 6-phosphatase. In addition, the gluconeogenesis pathway (reverse of glycolysis) can convert pyruvate back into glucose which is then released for use in other cells (particularly important in the brain as it requires glucose for metabolism).

The rate of glycolysis is regulated so that ATP is produced to satisfy energy demands. It is also coordinated with other metabolic pathways such as fat and protein metabolism in order to get the right balance derived from each source. Hormones play a central role in regulating the rates of these pathways. Insulin is produced in β cells in the pancreas and is secreted in response to high glucose levels. It is an antagonist to glucagon, which is produced in the α cells of the pancreas and acts to raise blood glucose levels by stimulating glucose production from glycogen stores and gluconeogenesis.

Insulin works to stimulate the uptake of glucose into cells which subsequently lowers blood glucose levels. However, transport into the brain and liver is not directly affected by insulin, although a lower blood glucose level will stimulate hepatic metabolic processes (Figure 3.2). It also inhibits the release of glucagon which stops the use of fats as an energy source. Glucagon also causes the liver to convert stored glycogen into glucose. Other enzymes in the glycolysis pathway can also regulate the rate of glucose metabolism.

3.4 Glycogenesis and Glycogenolysis

Following ingestion of a meal some glucose will be converted into glycogen, which is a readily available and quickly utilised energy store. Glycogen is a highly branched polysaccharide made up from glucose units. The main chain of

glycogen is formed of glucose units bonded at C_1 – C_4 and branches approximately once every twelve units via the C_1 – C_6 bond (Figure 3.5).

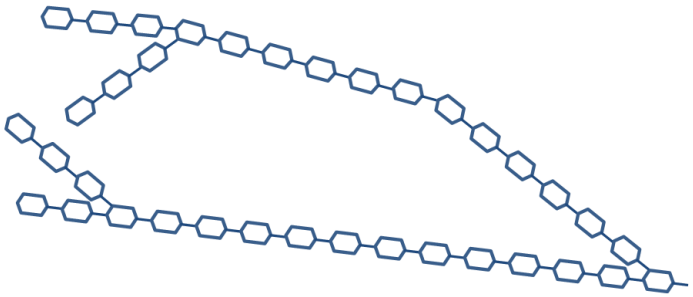

Figure 3.5 Branched glycogen molecule.

Glycogen is synthesised via a process called glycogenesis, and is broken down through glycogenolysis. An increase in insulin levels increases the rate of glycogenesis, whereas an increase in glucagon or adrenaline increases the rate of glycogen breakdown and conversion to glucose to be released into the blood stream.

The process of glycogenesis begins with a phosphorylated glucose molecule (glucose 6-phosphate and glucose 1-phosphate) as does glycolysis. Under the action of Uridyl transferase glucose 1-phosphate is then converted into UDP-glucose which is the precursor to the glycogen molecule. Initially, glycogenin is required as a primer creating the first glucosyl unit and also adds the first glucose molecules to the glycogen chain. Glycogen synthase then takes over continuing the process to elongate the glycogen chain. Glycogenin remains bound to the glycogen molecule throughout this whole process. Levels of

glycogen synthase are used to regulate the addition of glucose to the glycogen molecule.

During the post absorptive state glycogen is used to produce glucose which is released into the blood stream. This process of glycogenolysis is activated by glycogen phosphorylase which works to remove glucose from the $C_1 - C_4$ glycogen bond to produce glucose 1-phosphate without the need for ATP consumption through phosphorylation. Glucose 1-phosphate is then converted to glucose 6-phosphate which can be utilised in glycolysis (Section 3.3) or converted straight to glucose via glucose 6-phosphate. Remaining glucose units at the branching point ($C_1 - C_6$) can be removed directly by glucosidase in the form of glucose.

The rates of glycogenesis and glycogenolysis are regulated by the enzymes glycogen synthase and glycogen phosphorylase respectively, which are in turn regulated by insulin, glucagon and adrenaline as well as the rate of phosphorylation. As discussed above, insulin is secreted when blood glucose levels are high and stimulates an increased rate of glycogen synthesis. Insulin binds to receptors on the cell surface and causes a cascade of phosphorylation that ultimately activates glycogen synthase and glycogen synthesis. Conversely, glucagon is released when blood glucose levels are low. Glucagon works to produce cyclic adenosine monophosphate (cAMP) in liver cells which activates (through other processes) phosphorylase kinase. This in turn catalyses glycogen phosphorylase which is the enzyme used to catalyse the breakdown of glycogen into glucose.

3.5 Fatty Acid Synthesis and β-oxidation

Fats are metabolised in the liver and other cells by different processes from the carbohydrate metabolism processes outlined above. They provide the primary long term energy store and are deposited in large quantities for use in times of starvation. The vast majority of lipid is stored in adipose tissue although it can also be found inside liver cells and around internal organs. Whilst the primary function of fat is an energy store, visceral fat around organs also provides protection and insulation. Fats can be obtained directly from foods, or synthesised in the body.

The primary storage form of fat in the body is triglyceride, which consists of three fatty acid chains with a glycerol backbone. The fatty acid chains can be saturated, with only single hydrogen bonds (saturated with hydrogen atoms) or unsaturated, with one or more double bonds (unsaturated with hydrogen atoms) as shown in Figure 3.6.

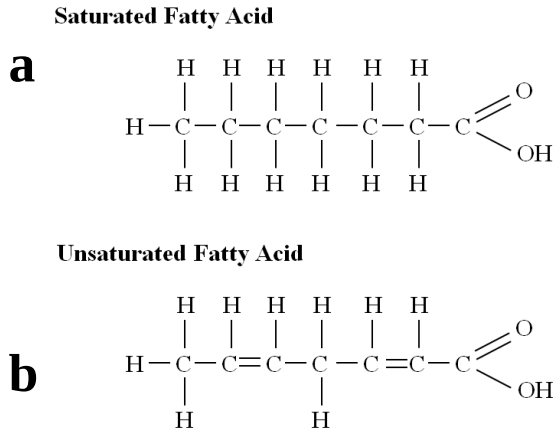

Figure 3.6 Fatty acid chains showing saturated (a) and unsaturated (b) fats (note the double carbon-carbon bonds).

Lipids stored in the cells as triglyceride cannot be released directly, but need to be broken down into fatty acid and glycerol via lipolysis. Similar to glycolysis, specific enzymes work to break down lipids into free fatty acids (FFA) which diffuse to the blood stream and are transported to tissues as required e.g. muscle or liver where they are again synthesised as triglyceride.

Inside the cell, triglycerides are broken down into fatty acids as catalysed by lipases according to energy requirements. Before being transported into mitochondria for oxidation FFAs are first converted into fatty acyl-CoA under the enzyme fatty acyl-CoA synthetase. Fatty acyl-CoA can then be transported into the mitochondrial matrix, where it undergoes β-oxidation to produce Acetyl-CoA for use in the TCA cycle to produce usable energy.

β oxidation provides the major pathway for fatty acid metabolism in which molecules are broken down to form Acetyl CoA (also formed from glycolysis, see above). Once in the mitochondria, Acyl CoA moved through various steps catalysed by dehydrogenating and hydrogenating enzymes and produces a yield of ~14 ATP molecules for each oxidation cycle, along with Acetyl CoA. One of the side effects of β oxidation is the release of oxidised radicals due to transfer of electrons from donors to acceptors used in the process. It has been suggested that these free radicals are damaging to cells. To combat this hepatocytes produce antioxidants (e.g. glutathione) that are released to maintain a reduced environment (i.e. decrease in oxidation state).

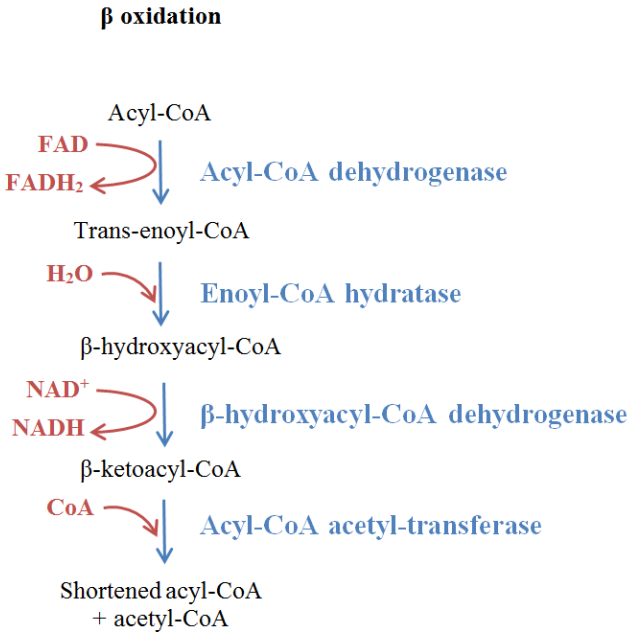

Figure 3.7 β oxidation pathway showing the conversion of Acyl-CoA into Acetyl-CoA that occurs in the mitochondria. Red are subsidiary products/reactions and blue show the active enzymes.

3.6 TCA Cycle

The TCA cycle, also known as the Krebs cycle, is a key metabolic pathway that generates energy through the oxidation of Acetyl CoA (derived from carbohydrate, lipids and proteins). Figure 3.8 shows an overview of the cycle, which occurs in the mitochondria of tissue cells. Acetyl CoA is generated from both pyruvate (glycolysis, Section 3.3) and Acyl CoA (β Oxidation, Section 3.5). At the start of the TCA cycle Acetyl-CoA is converted to citrate. Citrate undergoes numerous transformations producing many intermediaries used in other processes and requires much enzyme activity which is beyond the scope of this thesis. The majority of the energy from oxidative steps in the TCA cycle is transferred to NAD^+ to form NADH and oxaloacetate is regenerated to feed

back into the cycle. NADH can later be fed into oxidative phosphorylation to produce ATP from ADP.

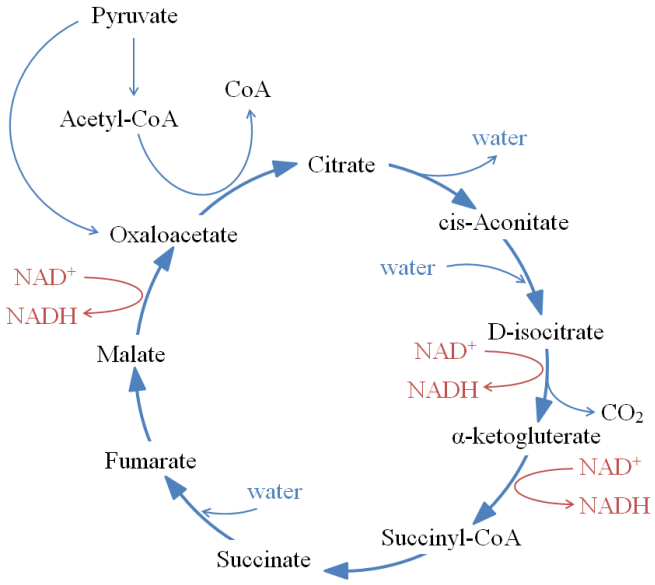

Figure 3.8 The TCA cycle.

Theoretically, one glucose molecule passing through glycolysis, the TCA cycle and oxidative phosphorylation yields 38 ATP, although in reality it is less due to various inefficiencies. The TCA cycle is predominantly regulated by the availability of substrates.

3.7 ATP

All the metabolic processes described above have the end point of providing a usable energy supply for all the cell's needs. Dietary intake, in particular fats and carbohydrates, are broken down and the energy is transferred and stored in ATP which is the energy currency of most cellular processes. ATP is formed by adding phosphate to adenosine diphosphate (ADP) or adenosine

monophosphate (AMP) from a phosphate donor, such as inorganic phosphate (P_i). The structure of ATP is shown in Figure 3.9.

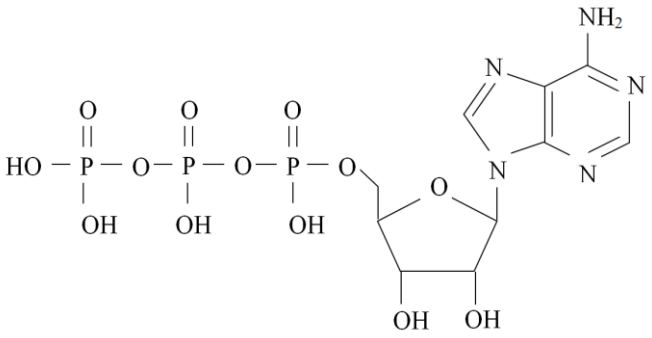

Figure 3.9 ATP molecule. Energy is stored in the phosphate bonds and released when broken down to ADP and AMP.

Cell processes that use ATP as the energy source break down the phosphate bonds to produce its precursors ADP and AMP, which release the energy stored.

The ATP energy supply is regulated largely by the enzyme AMP-activated protein kinase (AMPK) which detects the fluctuations in the AMP : ATP ratio. As AMP increases and ATP decreases due to consumption of energy, AMPK acts to up regulate many pathways to increase the ATP supply, such as glucose uptake, glycolysis, fatty acid uptake and β oxidation. It also works to block systems that will store fuel, such as glycogen synthesis and triglyceride synthesis. This process helps to maintain ATP homeostasis in cells and provides suitable energy for needs. Interestingly, this homeostasis can be overridden in hepatocytes by lowering the cellular phosphate level with fructose. The vast majority of absorbed fructose enters the liver which reduces

ATP to ADP rapidly during initial phosphorylation (to fructose 6-phosphate). Furthermore, in contrast to glucose the enzyme used in this process (fructokinase) is not inhibited by ADP and citrate and is therefore not regulated (for glucose the early stages of glycolysis are controlled by lowered ATP reserves). Lowered phosphate in the cells activates AMP deaminase which further converts ADP ultimately producing uric acid. This is explored in Chapter 5.

3.8 Conclusion

This chapter has discussed the basic metabolic processes occurring in the liver. The liver plays a crucial role in maintaining the appropriate energy supply for the body's needs. As explored in the Chapter 1, Magnetic Resonance Spectroscopy provides a powerful tool that can be used to investigate these metabolic pathways completely non-invasively.

Chapter 4 Technical developments of ^{1}H and ^{13}C MRS for Measurements of Hepatic Metabolism

This chapter explores technical developments of multinuclear MRS for use in hepatic metabolism studies. The first section explores ^{1}H MRS to measure liver lipid levels and considers the necessity of individual T_2 measurements, and the use of automatic post processing techniques and peak fitting algorithms. The second section investigates the effects of using surface coils and in particular the effects of B_1 field inhomogeneity on signal sensitivity for in vivo ^{13}C MRS. Finally, the third section explores the sensitivity of in vivo ^{13}C MRS glycogen measurements in a two-way randomized cross over study.

4.1 Introduction

Magnetic Resonance Spectroscopy is a powerful technique for investigating hepatic metabolism *in vivo*. As discussed in Chapter 1, ^{1}H MRS can be used to determine liver fat fractions [4, 23] and ^{13}C MRS provides the only non-invasive measure of glycogen stores [11, 28]. Together, these provide a complete picture of energy storage in the liver in the post absorptive state.

Whilst these techniques have been well validated and used in many studies, further technical developments are still required to optimize methods of acquisition and post processing. In this Chapter a number of important technical issues for ^{1}H and ^{13}C MRS are explored and their relevance to *in vivo* studies discussed.

^{1}H MRS Acquisition, Post Processing and Analysis

Despite the power and convenience of ^{1}H MRS measurements of liver lipid levels *in vivo* there is reluctance to use it in the clinical setting. Some of the main reasons for this are the technical steps required for processing data and for spectral analysis. For example, acquired ^{1}H MR Spectra need phase correction and frequency alignment which can be time consuming and requires a level of expertise. In addition, calculations of the water and fat peak areas can be complicated, even when using commercially available software (e.g. jMRUI). Spectral post processing and analysis is also open to human error as many stages rely on subjective user judgement. These stages were automated and compared with manual methods in order to develop quicker, simpler and more repeatable techniques (assessed in Section 4.2).

^{13}C MRS Surface Coil Signal Sensitivity

^{13}C MRS measurement of *in vivo* glycogen levels use multinuclear surface coils to transmit and receive the MR signal (Section 2.4.5). Although these improve the signal received due to their proximity to the tissue they cause added complications due to the inhomogeneous transmit B_1 field and receive sensitivity.

In the case of ^{1}H and ^{31}P MRS, three alternative methods have been employed to account for this spatial variation in B_1 field [61]. Firstly, the receive signal can be corrected based on expected spatial RF field variations modelled for the coil's geometry [62]; secondly, the signal can be corrected by comparison with a large phantom that corresponds to the subject's position and loading; or thirdly, B_1 maps can be acquired across a homogenous phantom to produce a sensitivity map that can be used to correct the final signal [61]. Despite these alternative methods of surface coil sensitivity correction available for ^{1}H MRS, ^{31}P MRS and MRI, less consideration has been given in the literature to B_1 inhomogeneity corrections of ^{13}C MRS. This is explored in Section 4.3.

***In Vivo* Glycogen Sensitivity**

The time scale of changes in hepatic lipid levels is different from that of hepatic glycogen. Liver lipid levels remain fairly constant with small fluctuations in the post prandial period and are changed significantly only after days, whereas glycogen stores rise immediately after meals over several hours through glycogenesis and are subsequently broken down to supply glucose to the body (Chapter 3) [63].

In the majority of cases, investigations of liver glycogen use extreme testing conditions such as large calorie intakes [28], feeds after long periods of fasting [10] or high levels of exercise [64]. Therefore, less is known about the more subtle changes that may be expected under normal physiological conditions or the *in vivo* sensitivity of MRS in response to a low calorie intake. This was investigated in a randomized cross over study and is reported in Section 4.4.

4.2 ^{1}H MRS Measurements of Hepatic Fat Fractions

4.2.1 Introduction

The aim of this study was to compare automated post processing and quantification of ^{1}H MRS with manual techniques in order to reduce the analysis time, level of operator expertise required and inter observer variability.

The data flow of MRS experiments is outlined in Figure 4.1 below:

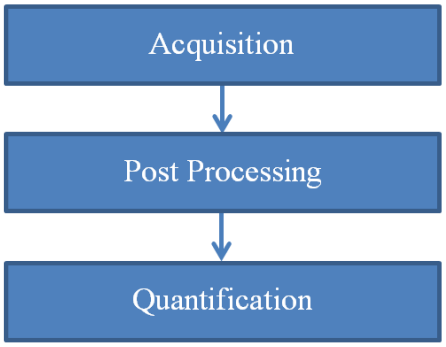

Figure 4.1 Data flow of MRS.

Acquisition

^{1}H MRS data is acquired using either PRESS [65] or STEAM [66, 67] localized spectroscopy (Section 2.4.4). These techniques have been compared in the literature [24] and there are specific benefits to each depending on the type of investigation. The main advantage of STEAM is that it uses shorter echo times which results in less time for signal decay and J coupling effects. On the other hand, PRESS has been shown to be less susceptible to motion

effects [68-70] and therefore is a better choice for respiratory triggered acquisition.

The spectral signal decays with T_2 relaxation (Section 2.2.3) which means that the acquired spectra need to be corrected back to their initial signal strength. This can be done using average population derived values [25] or by explicitly measuring relaxation by acquiring spectra at a range of TEs. Whilst the primary aim of this study was to compare automated and manual post processing and quantification, a secondary end point was to assess the variability in individual T_2 values to confirm whether future studies should include this during spectral acquisition.

Post Processing

The acquired FIDs are Fourier transformed to produce spectra that need to be post processed before fat fraction quantification (Section 2.3.2). Whilst many of the post processing steps are easily applied across all the spectra and require little to no input, such as zero filling (ZF) and line broadening (LB), other steps are usually undertaken manually and require subjective assessment. For studies with many subjects and multiple spectral acquisitions this can be incredibly time consuming and opens up the possibility of human error and inter observer variability. In this study, automatically and manually post processed spectra were compared.

Quantification

Following spectral post processing, the peak areas of the water and fat peaks need to be calculated, and various methods are available to do this [23]. Some

studies take the composite peak signal from all fat peaks upfield from water, whilst others examine only the peak corresponding to the main carbon chain back bone of lipids (the $-[CH_2]_n-$ peak) as it produces the most signal and is less susceptible to J-coupling effects and non-flat baselines. Peak areas can either be calculated by summing the spectral signal under the peak (or peaks) of interest, or by peak fitting using prior knowledge of expected peak shapes and models of metabolic NMR responses. This is not necessarily an easy process [23] as some fat peaks have complicated J coupling and may be overlapping with neighbouring peaks as is clear from the *in vivo* spectrum shown in Figure 4.4.

Peak fitting algorithms exist in commercially available software (e.g. AMARES in jMRUI) using simple least square fitting algorithms from user defined peak information and can be easily replicated using in house programmes (e.g. using Matlab). The advantage of using in house software is that peak fitting can be incorporated into automated post processing which further reduces analysis time and the expertise required. In this study an in house peak fitting algorithm was compared with a simple method that summed over user defined regions.

4.2.2 Method

Spectral data from 20 subjects with a range of liver fat levels were used in this study, acquired from a Philips Achieva 1.5T scanner (Philips, Best, The Netherlands) using a respiratory-triggered PRESS localized sequence (30mm x 30 mm x 30 mm, 512 samples, 1000 Hz bandwidth, 3000ms repetition time). Four spectra of varying TE were acquired (TE = 30, 40, 60 and 80ms) with

twice the averages at the shortest TE for higher SNR (8 averages for TE = 40, 60 and 80 ms; 16 averages for 30 ms). Long repetition times (3000 ms) allowed for full longitudinal relaxation. All spectral data were zero filled to 1024 data points and line broadened by 30 Hz before post processing.

Phase correction and frequency alignment were applied using both manual (MAN) and automatic (AUT) methods as outlined below. The water and fat peak areas were calculated using both Lorentzian fitting (LF) and user defined region summing (UD) methods also outlined below.

T_2 values were calculated by averaging the processed data for each of the four TE acquisitions and fitting an exponential function to the signal at each TE. The water and fat peak areas were fitted to an exponential relaxation curve and used to calculate T_2 times. Fat / Water peak ratios at TE = 30ms were used with individual T_2 values to determine fat fractions as described previously [25].

Manual Spectral Processing

Phase Correction. First order phase effects were negligible due to the small bandwidth in comparison to precessional frequency, and as such only linear zero order phase correction was required. Zero order phase corrections were made using manual adjustments in jMRUI until all peaks were positive. This was assessed using subjective visual analysis (Figure 4.2a).

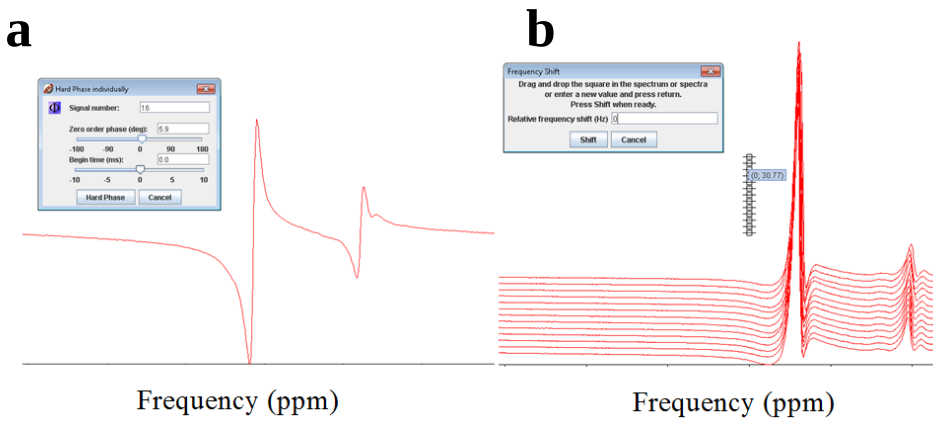

Figure 4.2 ^{1}H MRS post processing showing zero order phase correction (a) and frequency alignment (b) using jMRUI software.

Frequency Alignment. Following phase correction, shifts in resonance frequency between successive spectra were corrected by manually aligning the peaks for each acquisition before averaging in jMRUI (Figure 4.2b).

Peak Area Calculations Once the spectra had been processed and averaged together, the areas of the lipid peak (CH_2 only) and water peak were estimated to quantify the liver fat fraction. To do this the investigator defined the left and right extremes of the non-overlapping region of the CH_2 peak using in house software written in Matlab and the area of signal between these points was determined by summing across the region.

Automatic Spectral Processing

All automated post processing steps were written in Matlab.

Phase Correction. Phase correction was automated by cycling through different zero order phase shifts until all absorption peaks were positive. This was found by monitoring the minimum spectral point for each phase shift loop.

The final phase corrected spectra was defined when this minimum point reached a maximum (Figure 4.3).

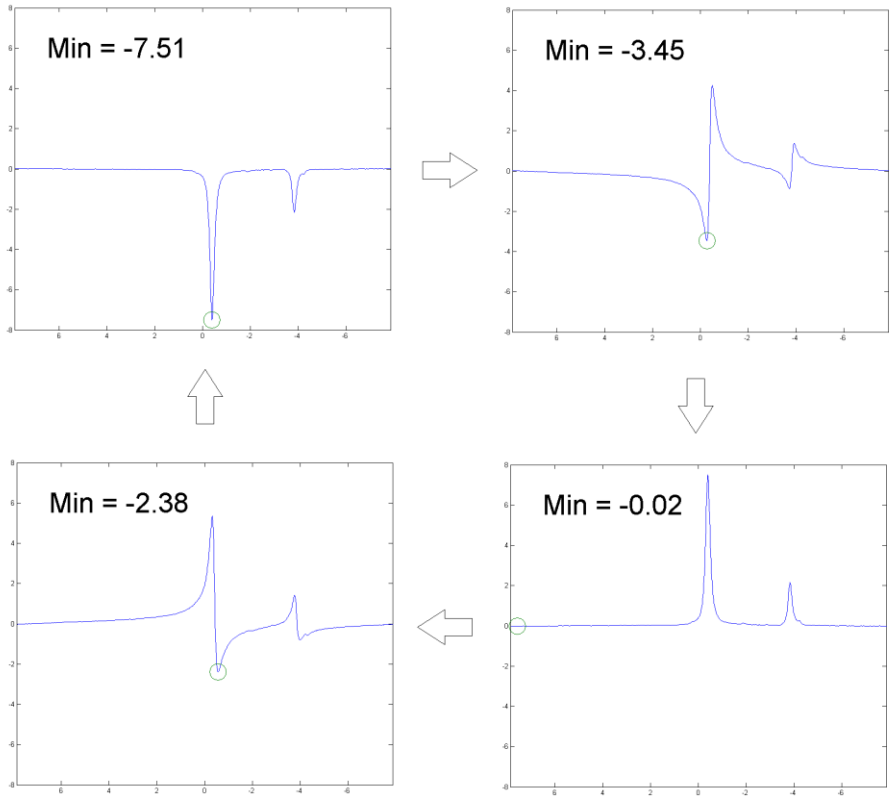

Figure 4.3 Cycling through phase shifts with minimum data point quoted. When min is greatest, the spectrum is phase corrected.

Frequency Alignment. Frequency alignment was automated by finding the maximum spectral point (water peak maximum) of the first spectrum and aligning subsequent spectra with this.

Peak Area Calculation A peak fitting algorithm was written to fit water and fat peaks separately to Lorentzian curves and measure the area under the fitted peaks. The investigator defined the non-overlapping region of the main CH_2 peak (~1.3 ppm) and a least square fitting algorithm calculated the best

Lorentzian curve fit in this region. For the water peak (~4.7 ppm) the maximum spectral point was found and the Lorentzian fit algorithm was applied (Figure 4.4).

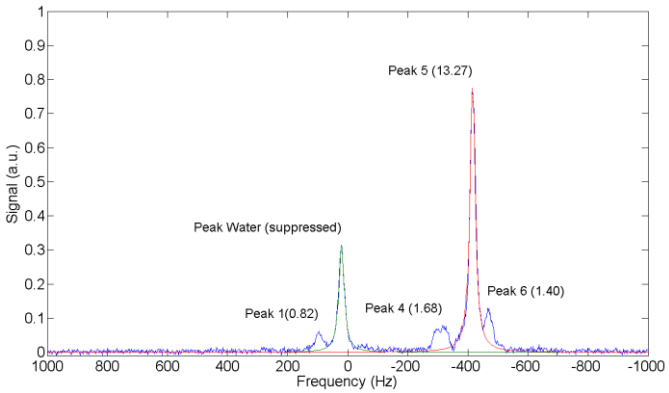

Figure 4.4 Peak fitting algorithm of main CH_2 peak (peak 5) shown on an *in vivo* water suppressed liver lipid spectrum (peak size in brackets). Peaks are numbered according to Table 1.1 from Chapter 1.

4.2.3 Statistical Analysis

All values are quoted as mean ± SD. Coefficients of variation were calculated to assess inter-subject T_2. Correlations between manual post processing and automated post processing and also between area under user define peak regions and area under Lorentzian fitted peaks were assessed using linear regression analysis. Means difference T testing was used to compare means between techniques using the SPSS software. Significance was attributed to $P < 0.05$.

4.2.4 Results

T_2 Variability

The mean T_2 value across subjects was 40 ± 11 ms for the lipid peak and 42 ± 6 ms for the water peak. The inter-subject coefficient of variation was 27% for the lipid peak and 15% for the water peak. The mean standard error of regression in fitting across subjects was 12% for the lipid peak and 6% for the water peak.

Peak Correction and Frequency Alignment

A comparison of manual and automated post processing is shown in

Table 4.1. Significant differences between manual and automatic processes were seen in the lipid peak area and the final fat fraction calculations which were significantly lower for the automatic processing compared with manual processing.

	Manual	**Automatic**	**Significance (P < 0.05)**
Lipid Peak Area	87 ± 58 a.u.	68 ± 49 a.u.	$P < 10^{-7}$
Lipid T_2	40 ± 10 ms	49 ± 11 ms	-
Water Peak Area	492 ± 120 a.u.	492 ± 121 a.u.	-
Water T_2	42 ± 6 ms	49 ± 8 ms	-
Liver Fat Fraction	16 ± 12 %	15 ± 11 %	$P < 10^{-7}$

Table 4.1 Results showing comparison of ^{1}H MRS manual and automatic processing (P values is significant differences between methods).

Correlation between manual and automated results for lipid peak area and fat fractions are shown in Figure 4.5a and b. The data is spread evenly over a broad range of values and contains no obvious outliers, with a statistically significant Pearson correlation coefficient ($P < 10^{-7}$). The gradient and y intercepts are shown on the graphs indicating the variation from the line of identity.

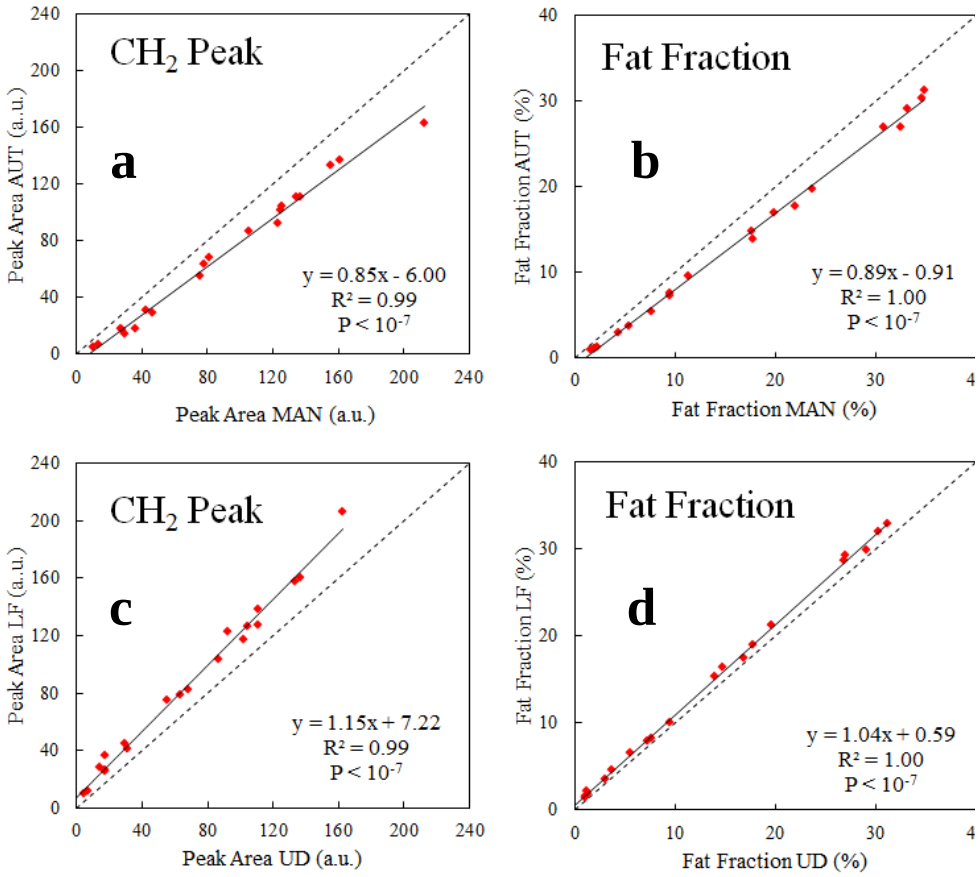

Figure 4.5 Correlations of lipid peak area (a and c) and fat fractions (b and d). AUT and MAN are automatic and manual phase correction and frequency alignment respectively; LF is Lorentzian peak fitting algorithm and UD is user defined peak region calculations.

Peak Fitting

Both the lipid and water peak areas were significantly greater using Lorentzian fitting compared with the area under user defined peak regions. T_2 values were not significantly changed. The liver fat fraction estimated using Lorentzian fitting was 15 ± 11 % compared with 13 ± 11 % for area under user defined regions (mean difference $P < 10^{-7}$) and there was strong significant correlations between these measures (Figure 4.5c and d).

Fully automated phase correction, frequency alignment and peak fitting together gave mean fat fractions of 15 ± 11 % compared with fully manual processed mean fat fractions of 16 ± 12 %. Correlations between methods were strong and significant (Figure 4.6).

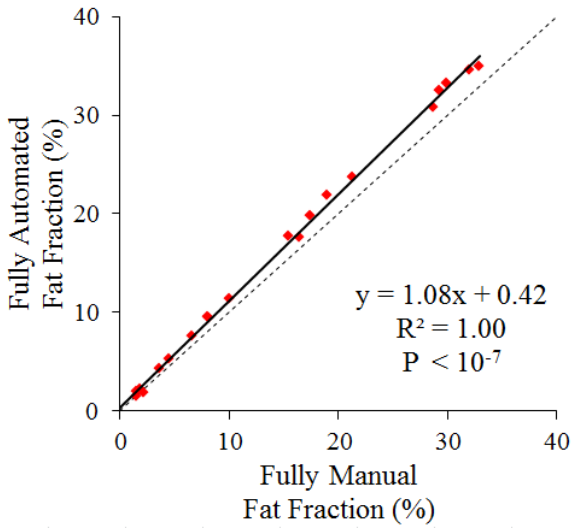

Figure 4.6 Correlation and linear regression of fully automated v fully manual processed liver fat fractions. Identity line is shown as dotted line.

4.2.5 Discussion

This study has explored some of the techniques of ^{1}H MRS analysis relating to acquisition (T_2 calculations), post processing (phase correction and frequency alignment) and quantification (peak fitting).

Firstly, measurements of T_2 relaxation in this study confirmed that individual calculations of relaxation rates are important for *in vivo* lipid studies. The coefficients of variation across subjects were higher than the standard error from exponential fitting showing that inter subject differences in T_2 for fat and water were greater than noise in the data. Analysis of the impact of this variability on liver fat fractions is substantial and could contribute to an error of ±30%. Stephenson *et al* [25] reported a single session variability in hepatic fat fractions at 3T of 12% and 7% for those with and without diabetes respectively. This means that T_2 variability across subjects has a greater potential effect than random fluctuations due to single session repeat measure variability and suggests that individual T_2 measurements are preferable over bulk population values. This is in agreement with previous studies and is important in clinical populations where T_2 is sometimes changed by iron. For example, Hamilton et al [23, 24] have published a number of studies exploring these factors and concluded that individual measurements of T_2 should be made where possible. The disadvantage of this is that it adds extra scan time for respiratory triggered protocols or will require added breath hold scans for non-respiratory triggered acquisitions. This is relevant for studies with patients who may struggle with longer scans.

Automated phase correction and frequency alignment showed strong and significant correlations with manual techniques with some notable advantages. Comparing fat peak areas calculated using the manual (area under user defined regions) and automated (Lorentzian fitting) processing showed smaller peak areas for automated processing. It is likely that the lower estimation from automated processing results from a better phase correction and frequency alignment producing a flatter baseline and narrower peaks. In particular, small subjective human errors of judgement in aligning peaks before averaging cause spectral peaks to blur and become broader. This suggests that the automated post processing gives a more precise fat fraction.

Lorentzian fitting gave consistently greater peak areas for both water and fat signal. This was expected as the user defined peak regions exclude the area of the peak that is overlapping with adjacent fat peaks (see peak 5 on Figure 4.4). It is reasonable to conclude that the peak fitting algorithm will produce more accurate fat fraction calculations given that it accounts for the full peak shape and more reliably reflects the CH_2 peak signal, although this should be tested against a gold standard. Other studies have explored peak fitting using AMARES in jMRUI [23] and also Gaussian fitting algorithms. The AMARES software in jMRUI is designed to be versatile for all metabolite fitting, and as such can be complicated to use for a simple analysis of fat. The fitting algorithm used in this study can easily be incorporated into the automatic post processing steps to allow all post processing and quantification to be done in a single software package during one operation. An interesting direction for

future research would be the inclusion of different fat peak analysis in healthy and patient populations.

Interestingly, this study showed an opposite effect from automating the phase correction and frequency alignment (smaller fat fractions) compared with using peak fitting (larger fat fractions) which more or less cancelled each other out when used together. Whilst this meant that the final results were similar, it seems advisable to ensure each stage produces as accurate a result as possible.

In summary, inter subject T_2 variability exceeded intra session variability reported in previous studies. As such, individual T_2 values should be measured by acquiring spectra at varying TE. The overall fat fractions for automated post processing and peak fitting correlated significantly with manual processes. Lower estimations of mean fat fractions using automated processing and analysis represent more precise results. Automated post processing techniques also provide a more repeatable method of analysis which results in a more reliable measurement by minimising user input, and also dramatically reducing analysis time. The final fat fractions of automated processing and peak analysis may also be more accurate as they use objective optimisation of phase correction and frequency alignment and use the full peak in fat fraction calculations.

4.3 Surface Coil Signal Sensitivity of ^{13}C MRS Measurements of Glycogen Stores

4.3.1 Introduction

The aim of this study was to assess surface coil sensitivity as applied to *in vivo* ^{13}C MRS measurements of glycogen in the liver. Figure 4.7 shows the 14 cm diameter PulseTeq (Surrey, UK) surface coil used for ^{13}C MRS experiments in this thesis. The surface coil connects to the 3T Philips Achieva Scanner (Philips, Best, The Netherlands) and is attached to the subject using a Velcro belt (Figure 4.7b). The surface coil also contains a ^{1}H quadrature decoupling coil as outlined in Section 2.7.6.

Figure 4.7 PulseTeq ^{13}C surface coil used for glycogen signal detection (a), position of subject (b), and MR image of liver (c) showing region of interest.

Due to the B_1 field inhomogeneity intrinsic to surface coil techniques there will be a position dependent flip angle of magnetization, and a position dependent sensitivity of the receiver to spin precession. These two components make up the overall signal sensitivity. Previous studies have modelled the magnetic field around a surface coil for ^{1}H MRS at frequencies less than 3T and found good approximations using a static field model from the Biot-Savart law [71, 72].

These simple models have been compared with *in vivo* data for scanners up to 1.5T and can be used to correct inhomogeneity effects in MRI [71]. However, at higher frequencies the static field approximation breaks down as transmission wave and tissue conductivity effects begin to make the B_1 field within tissue more complex, requiring more complicated full wave modelling. By comparison, ^{13}C MRS at 3T resonates at a frequency ~1/4 of ^{1}H so that the precessional frequency at 3T is comparable to ^{1}H acquisition at < 1.5T suggesting that a simple static field approach can be made.

Hoult *et al* [73, 74] derived the induced EMF (ξ) in a surface coil during the NMR experiment by applying the law of reciprocity, shown in Equation 4.1:

$$\xi = 2\omega {M_{xy}}^{(+)}(B_{1x} - iB_{1y})$$

Equation 4.1

where ${M_{xy}}^{(+)}$ is transverse magnetization in the positive rotating frame and B_{1x} and B_{1y} are the transverse magnetic fields in the corresponding directions. In this equation, ${M_{xy}}^{(+)}$ represents the transverse magnetization of the nuclei after the RF pulse and $(B_{1x} - iB_{1y})$ represents the receive signal from this magnetization so that ξ is a measure of the overall signal sensitivity. In order to assess the effects of signal sensitivity on *in vivo* ^{13}C MRS studies the transmit and receive components need to be assessed individually and then combined together using the above equation.

This study explored the effects of signal sensitivity on ^{13}C MRS experiments in the liver using a static field approximation (Biot-Savart method) and considered its relevance for *in vivo* experiments.

A program was written in Matlab to calculate the signal sensitivity at typical liver distances, as described below. This was compared with 3 alternative phantom methods of measuring surface coil sensitivity: (1) Multiple ^{13}C MRS acquisitions from a small high concentration glucose phantom at varying positions; (2) Magnetic Resonance Spectroscopic Imaging (MRSI) of a large homogenous methanol phantom; and (3) Acquiring ^{13}C MRS from a liver type glycogen phantom (typical volume and concentration) at a range of distances from the surface coil.

4.3.2 Method

Modelled Data

The steps taken to determine the signal sensitivity at typical liver distances are outlined in the flowchart shown in Figure 4.8.

(1) Modelling the RF pulse response at varying B_1

A computer programme was written in Matlab to model pulse excitation profiles using rotation equations. A vector version of rotational matrices was used, defined in the Rodriquez rotation formula (Equation 4.2).

$$\boldsymbol{v_{rot}} = \boldsymbol{v}\cos\theta + \left(\hat{\boldsymbol{k}} \times \boldsymbol{v}\right)\sin\theta + \hat{\boldsymbol{k}}(\hat{\boldsymbol{k}} \cdot \boldsymbol{v})(1 - \cos\theta)$$

Equation 4.2

where $\boldsymbol{v}$ is the initial position of a vector, $\boldsymbol{v_{rot}}$ is the rotated position of the vector, θ is the angle of rotation and $\widehat{\boldsymbol{k}}$ is the unit vector normal to vectors $\boldsymbol{v}$ and $\boldsymbol{v_{rot}}$ [75].

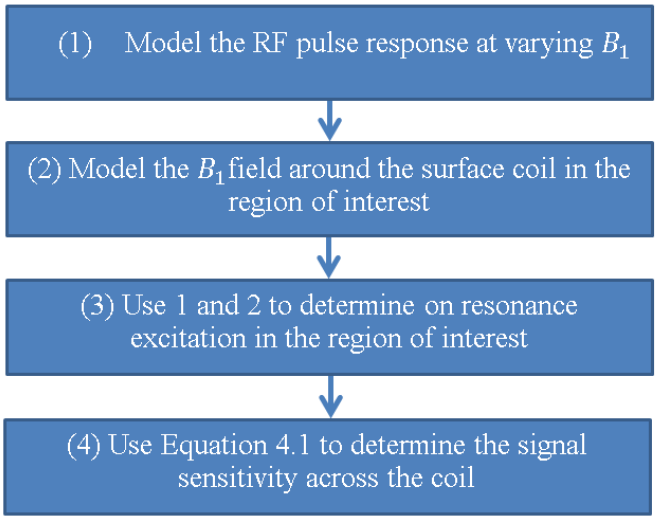

Figure 4.8 Flow chart of method used for modelling signal sensitivity of a surface coil used in ^{13}C MRS.

Equation 4.2 was used to simulate magnetization response step by step successively through the pulse with rotation angles determined usingB_{eff}, γ and the rotation axis aligned with B_{eff}. The script was first tested on a basic block pulse, and then applied to an AFP pulse. Finally, an AHP pulse response (as used in *in vivo* experiments) was modelled using a hyperbolic secant pulse profile with parameters defined from the standard adiabatic pulse in the Philips 3T multinuclear MRS protocol (pulse width = 3.5 ms, frequency sweep from -1821 Hz to 0 Hz for AHP and +1821 Hz for AFP, peak B_1 = 150 μT).

(2) Modelling the B_1 Field Across a Surface Coil

A second programme was written in Matlab to model the variation in B_1 field across a 14 cm diameter single loop surface coil (as used in later *in vivo* ^{13}C MRS studies) using a static field model. The script calculated the integrated effects of current elements around a closed loop representing the coil on each pixel in the field of view, using the Biot-Savart law (Equation 4.3).

$$\boldsymbol{B} = \frac{\mu_0}{4\pi} \oint \frac{I\boldsymbol{dl} \times \boldsymbol{r}}{|\boldsymbol{r}|^3}$$

Equation 4.3

where $\boldsymbol{B}$ is the magnetic field at distance $\boldsymbol{r}$ from current element $\boldsymbol{dl}$ [76].

(3) Determining On Resonance Excitation in the Field of Interest

The effects of RF pulse shape on spins in the field of view found in (1) and the Biot-Savart approximation of B_1 field across the surface coil (2) were combined together to determine the transverse excitation in the field of view near a surface coil.

(4) Determining the Signal Sensitivity of the Surface Coil for ^{13}C MRS

Finally, this was substituted into Equation 4.1 to determine the signal sensitivity across the coil.

Assuming transverse magnetization varies approximately linearly with B_1 at typical liver distances from the coil, M_{xy} can be substituted for in Equation 4.1 to determine the approximate induced EMF in response to excitation from AHP pulses.

$$\xi = \frac{\omega\kappa\left(B_{1x}^2 + B_{1y}^2\right)}{2} \propto B_1^2$$

Equation 4.4

where κ is the proportionality constant relating transverse magnetization to B_1 [74]. Equation 4.4 was used to map out the signal sensitivity of AHP pulses across the surface coil for ^{13}C MRS.

Phantom Data

All three phantom methods used a single loop 14cm ^{13}C surface coil (PulseTeq, Surrey, UK) with integrated quadrature decoupling coils as described in Chapter 2.

Small Phantom Method. A 10 mm diameter high concentration $^{13}C_1$ labelled glucose vial was produced (~500 mmol/l) and ^{13}C MR spectra acquired for varying vial positions. A polystyrene insert cut to fit the geometric shape of the coil was used with pre-set holes for vial positioning at 10 mm spacing in both directions along the surface of the coil (100 mm x 100 mm) as illustrated in Figure 4.9. The vial was placed in each hole during successive scans which was repeated over 4 planes (30 mm, 40 mm, 70 mm and 100 mm). Spectra were acquired using a non-localized AHP pulse-aquire sequence with proton

decoupling (512 samples, 7000 Hz bandwidth, 144 averages, 2150 ms repetition time, narrowband decoupling, scan duration ~ 5 minutes).

Water vials were positioned in a ring around the glucose vial to make it possible to determine the distance of the phantom from the coil (Figure 4.9 and Figure 4.10). Additional water pouches were also included for coil loading.

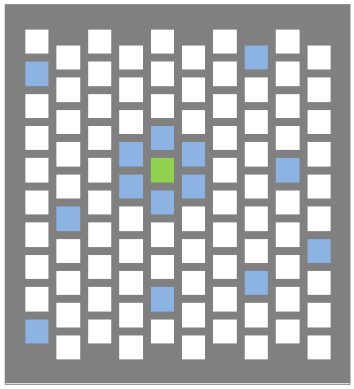

Figure 4.9 Position of holes for glycogen vial placement in polystyrene surface coil insert. Green is glycogen vial, Blue is water vial.

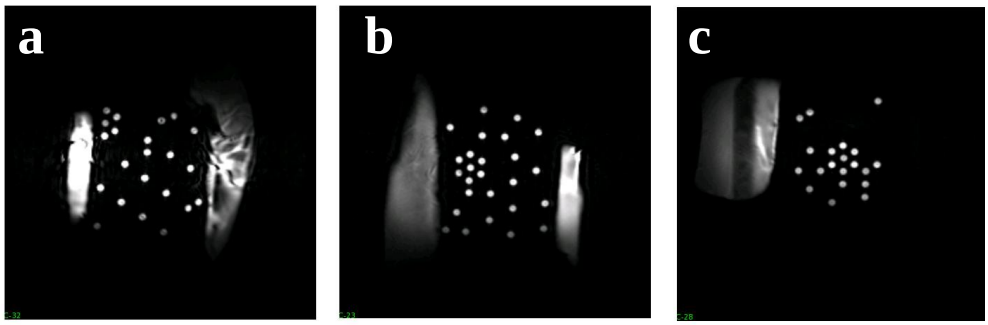

Figure 4.10 MRI images showing glycogen position (cluster ring of vials) in top left (a) centre left (b) and centre (c).

Data were analysed using a semi-automated phase correction and peak area calculations outlined in Section 4.2, although for ^{13}C MRS the corrections were more complicated and required a higher level of user input including first order phase corrections due to the wider bandwidth. Scout MRI images were acquired (Figure 4.10) to measure for distance from the coil. The glucose / reference peak ratios (Figure 4.11) were plotted against distance from coil in each plane.

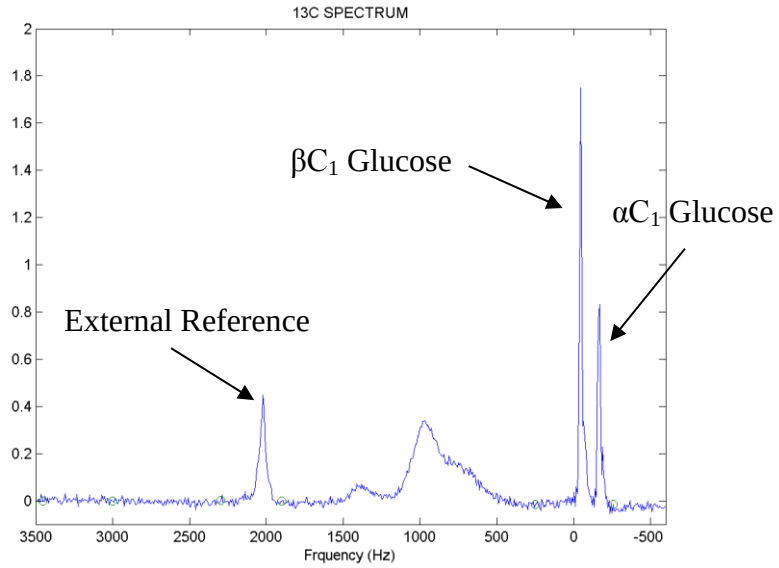

Figure 4.11 ^{13}C MRS spectrum of small glucose phantom, with external ^{13}C formate peak visible also

MRSI Method. MRSI sequences were first tested on the small glucose phantom used above. Following this, a large homogenous methanol flood phantom was used to determine coil variations in ^{13}C MR spectra signal. Data were acquired in 10mm x 10mm voxels using a slice selective phase encoded MRSI sequence (2048 samples, 7000 Hz bandwidth, 4000 ms repetition time, narrowband decoupling). On analysis, the area under the reference peak was first used to

confirm localization due to its known location at centre of coil. The area under the methanol peaks were then calculated and used to map out signal strength using in house software. The results were compared voxel by voxel with the Biot-Savart model using linear regression analysis. Signals across planes were also averaged for comparison between techniques.

Liver Phantom Method. A large cylindrical phantom was produced of comparable size and concentration with a typical adult human liver (volume = 1.5 l, concentration = 200 mmol/l, Potassium chloride = 150 mmol/l, sodium azide = 0.05%). Spectra were acquired at varying perpendicular distances between the phantom and the coil surface (MRI Figure 4.12). Water pouches were added to increase signal for preparation steps and fat pouches were added in order to emulate *in vivo* conditions as closely as possible. ^{13}C MR spectra were acquired using a non-localised adiabatic sequence (512 samples, 7000 Hz bandwidth, 528 averages, 2150 ms repetition time, narrowband decoupling, scan duration ~20 minutes) and post processed using in house software (ZF = 4096, LB = 30Hz). The integrals of the glycogen peaks (100.5 ppm) and an external reference peak were calculated and ratios were used to determine variations in signal strength with perpendicular distance from coil (taken as distance to centre of phantom) as described previously [28].

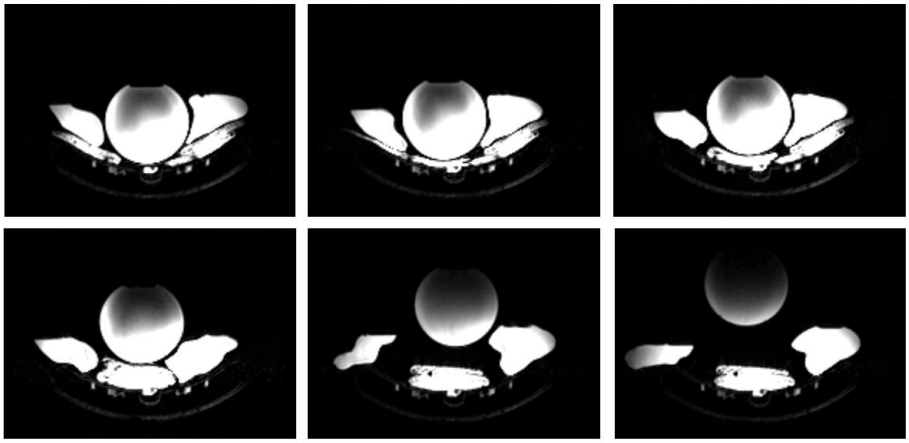

Figure 4.12 MRI scans showing increasing distance of large glycogen phantom from surface coil along the bottom of image.

4.3.3 Results

Modelled Data

(1) RF Pulse Response at Varying B_1

The modelled excitation responses of a $\pi/2$ block pulse across the bandwidth are shown in Figure 4.13 and were as expected. Scaled to $M_{z\,eq}$, the pulse causes transverse magnetization to move from 0 to 1, longitudinal magnetization to move from 1 to 0, and the x and y components to become out of phase by $\pi/2$.

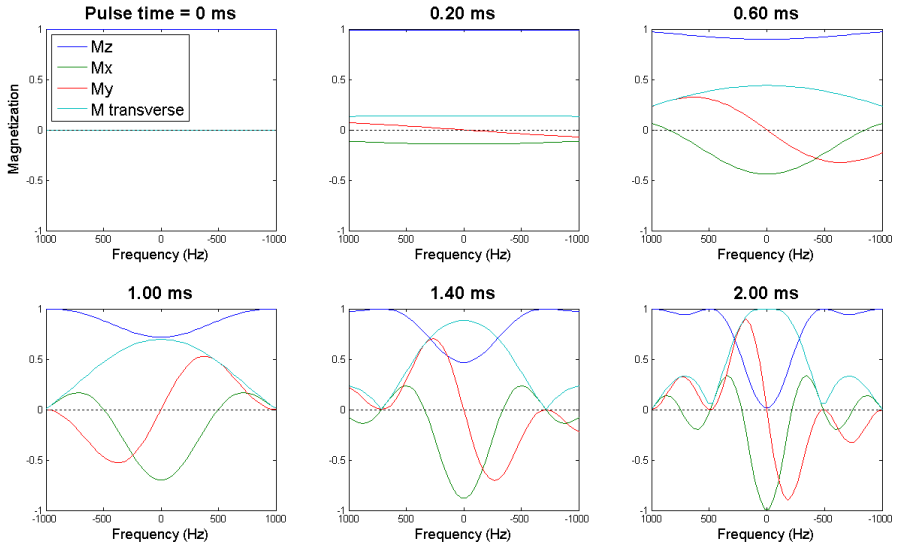

Figure 4.13 Magnetization (x, y, z) in response to a block pulse ($\boldsymbol{B_1}$= 2.94 μT) at various time points (0, 0.2, 0.6, 1.0, 1.4 and 2.00 ms) until full on resonance excitation is achieved (τ = 2 ms).

Figure 4.14 shows the modelled final response to the AFP hyperbolic secant pulse. The longitudinal excitation following the pulse shows uniform inversion across the frequency sweep range of the hyperbolic secant RF pulse (-1821 Hz to +1821 Hz) as expected, with spins outside this range unaffected by the pulse. The effects of varying B_1 are shown in Figure 4.14c with B_1 coming out of page from 0 to 150 μT. This showed an approximately linear dependency at lower B_1 which plateaus for the final 1/3 of the B_1 range. At sufficient power (~100 μT) complete inversion is achieved across the frequency sweep range regardless of B_1.

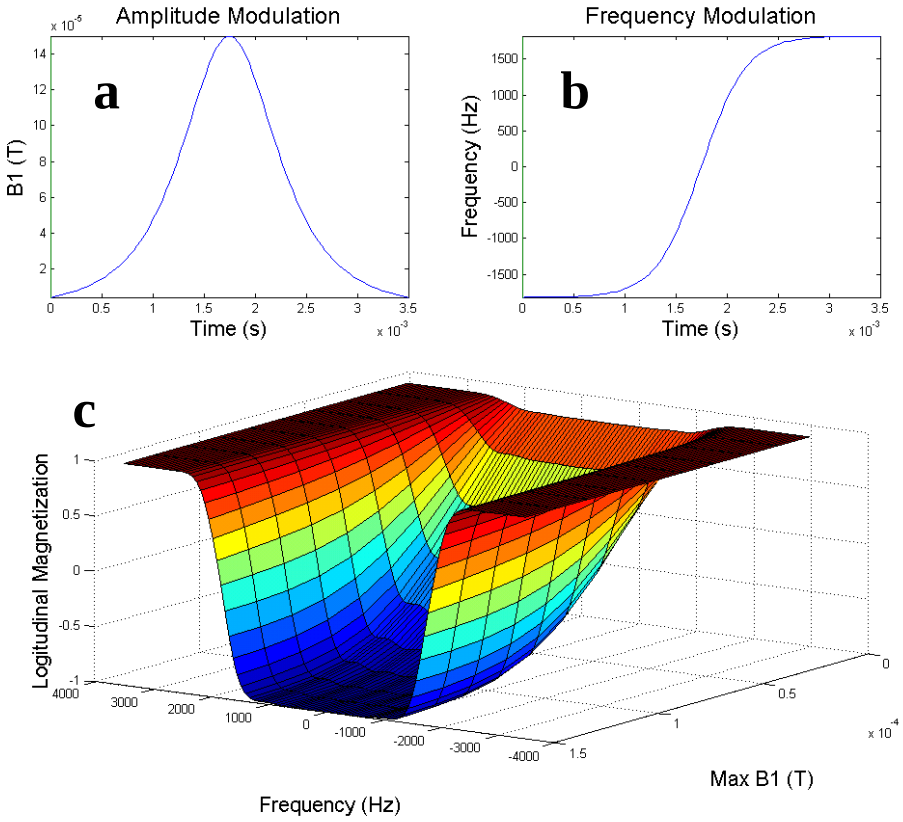

Figure 4.14 Pulse amplitude modulation (a), pulse frequency modulation (b), and longitudinal magnetization response (c) across a 3T ^{13}C MRS bandwidth (7000 Hz) for a range of pulse $\boldsymbol{B_1}$.

The response to the AHP pulse is shown in Figure 4.15. Uniform ^{13}C excitation was not achieved across the spectral bandwidth. At full B_1 field strength, the signal is reduced off resonance and there is a small dip in signal at around 1000 Hz upfield from resonance.

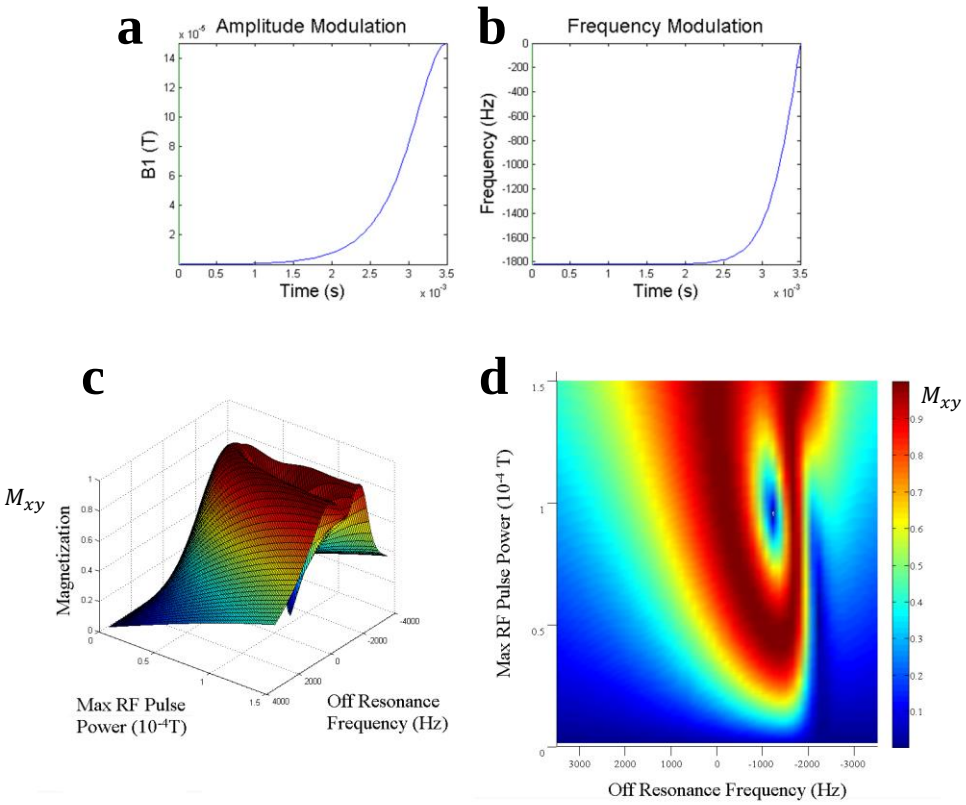

Figure 4.15 The pulse profile for AHP pulse showing amplitude modulation (a) and frequency modulation (b), and the transverse magnetization response across the bandwidth (c and d) and for varying pulse $\boldsymbol{B_1}$.

The transverse signal remains above 40% maximum achievable magnetization across the majority of the spectral window at the applied RF power (150 μT).

Figure 4.16 shows a cross section through Figure 4.15 showing the variation in transverse magnetization with B_1 for on resonance spins alongside the modelled response to a $\pi/2$ block pulse of equal duration. The difference between these curves represents the increase in transverse magnetization achieved using an AHP pulse. Over the range of B_1 field strengths the

excitation from the AHP pulse was consistently greater than the block pulse (greatest difference at ~60% B_1) and converged at 100% efficiency.

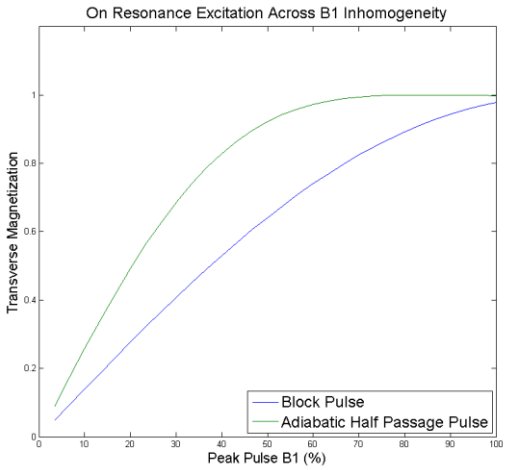

Figure 4.16 Transverse magnetization of on resonance spins over a range of peak pulse field strengths in response to a block pulse (blue) and an AHP pulse (green).

(2) B_1 Field across a Surface Coil

Figure 4.17 shows the B_1 field drop off with perpendicular distance from coil. As indicated on the graph, previous MRI data suggests that the distance of the closest edge of liver tissue from the surface coil in lean subjects is greater than 30 mm, which corresponds to B_1 field strengths of less than 25% of the maximum applied field.

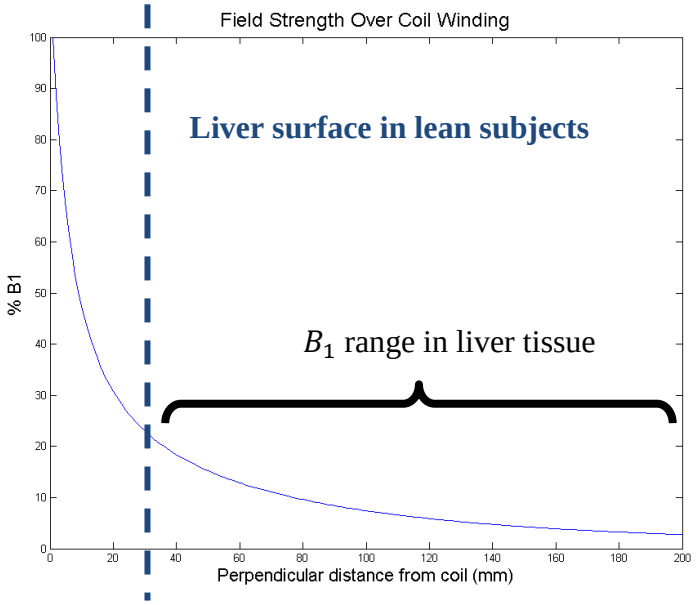

Figure 4.17 B_1 drop in signal as voxels move away from the coil wire.

(3) On Resonance Excitation in the Field of Interest

The excitation response of on resonance spins for the range of B_1 typical in liver tissue (< 25%) was confirmed to be approximately linear with B_1 as expected (Figure 4.17 and Figure 4.15). As such, Equation 4.4 can be used to determine the signal sensitivity as described in the Methods (Section 4.3.2).

(4) Signal Sensitivity of the Surface Coil for ^{13}C MRS

The coil sensitivity in the field of view is shown in Figure 4.18a and Figure 4.22b (compared with phantom methods). The maximum signal is found close to the coil wires (symmetrically in bottom corners) and the maxima begin to merge together at increasing distances from the coil. From ~50mm from the coil surface the field drop off is fairly sharp.

Comparison with Phantom Data

Small Phantom Method. Figure 4.18 shows the sensitivity maps acquired from each of the four planes. The 30 mm plane had peak signals towards the edge of the region although there is no discernibly systematic pattern. As the plane moves further from the coil the signal drop is substantial and the peak signal moves more towards the centre of the plane.

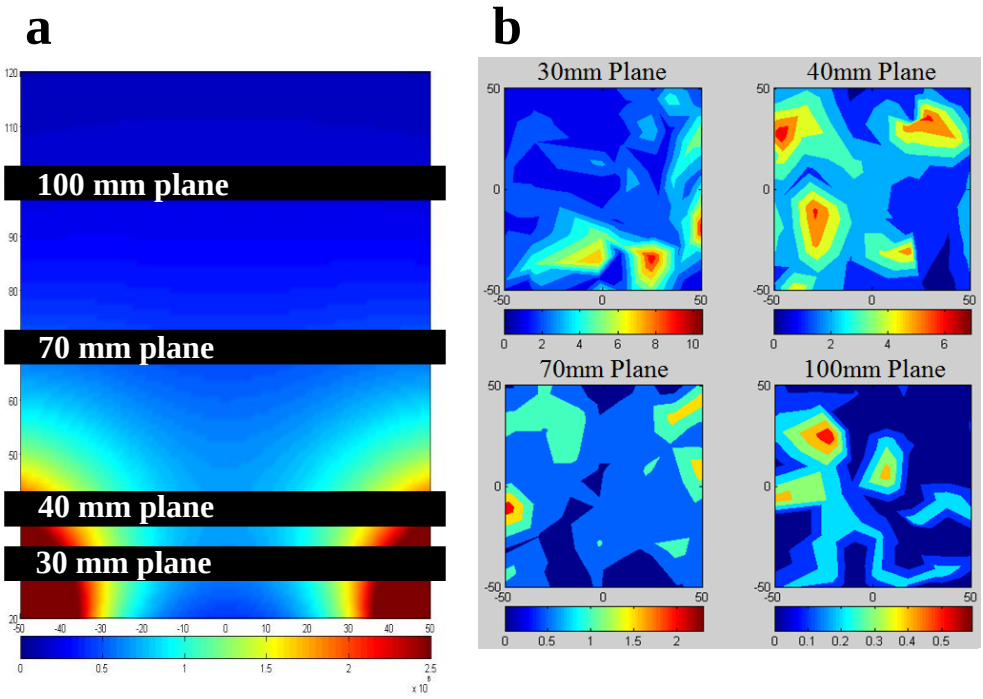

Figure 4.18 Biot-savart model of surface coil sensitivity (a); and signal strength in glucose / ref peaks at varying position across each of the 4 planes: 30mm, 40mm, 70mm and 100mm (b). Note that the scale decreases for increasing slices in b.

The histogram of signal strength across each plane (Figure 4.19a) shows a narrower spread in signal intensity as the plane moves away from the coil as

expected from the Biot-Savart model. Figure 4.19b shows how this varies with perpendicular distance from coil. The largest range in signal is found for the planes closer to the coil.

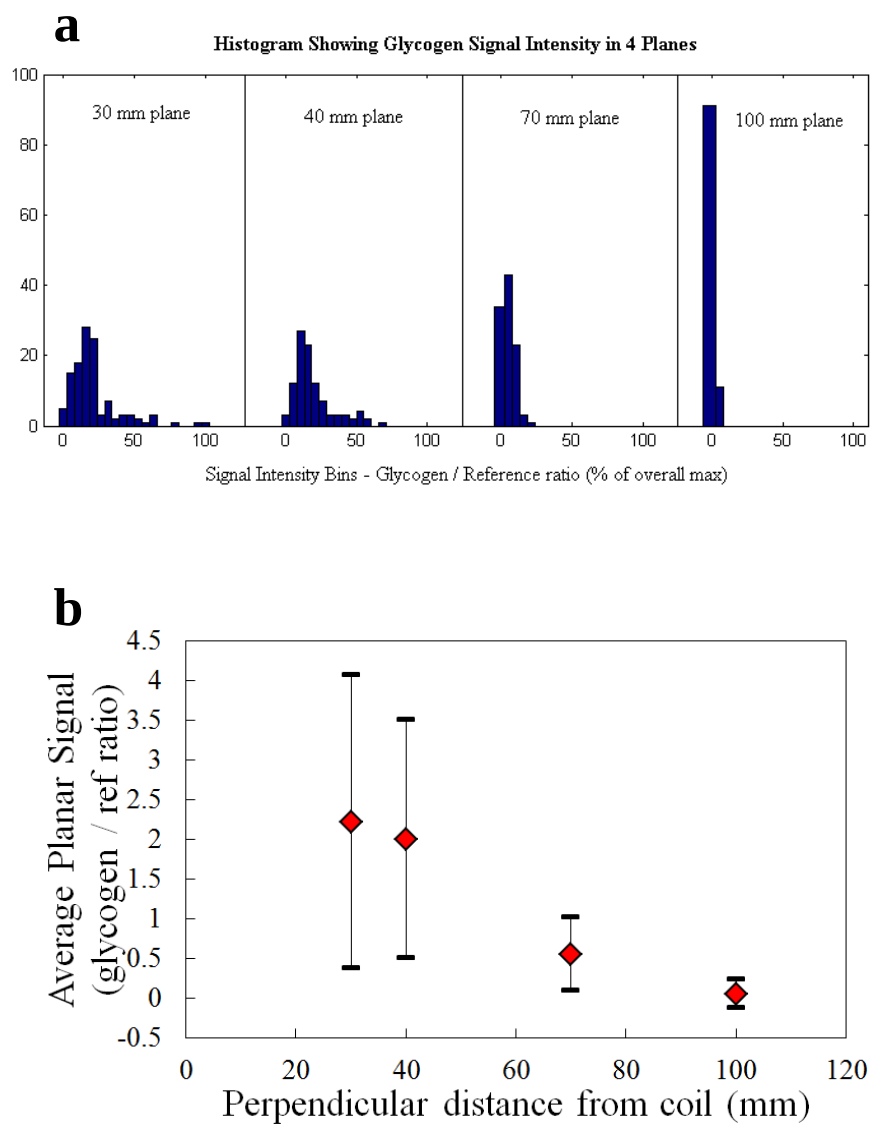

Figure 4.19 Histogram showing signal spread in each of the four planes (a) and a plot of average planar glucose/ref signal showing decreasing deviations (b).

MRSI Method. The ^{13}C MRSI sequence successfully localised the concentrated glucose phantom, as can be seen from Figure 4.20. Two different positions of the glucose vial were clearly located in the same regions as the glucose vial from MRI scout images (see rings in Figure 4.20a).

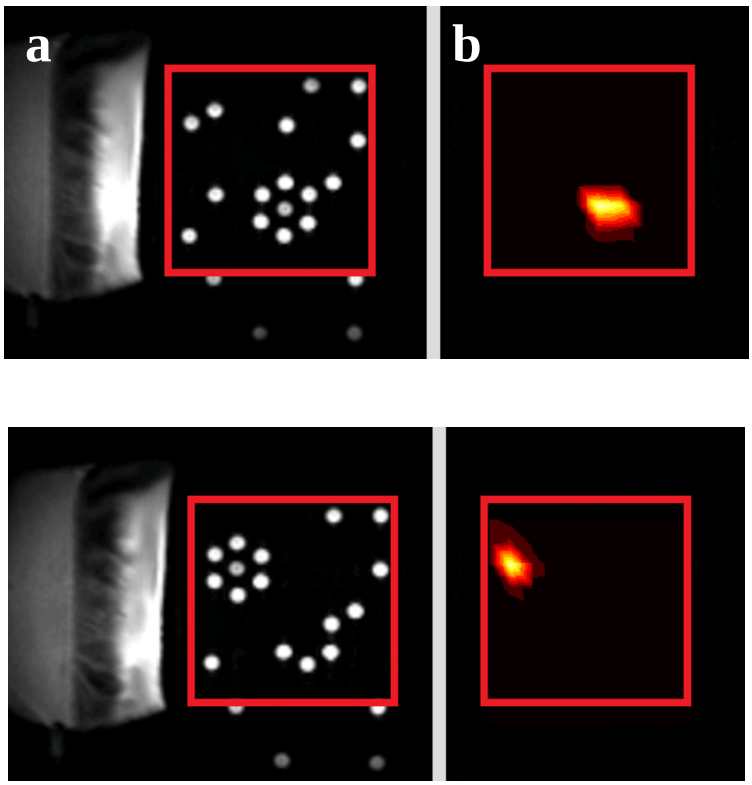

Figure 4.20 ^{13}C MRSI data mapping out glycogen signal intensity (b) and MRI of glycogen vial position (a) showing strong visual correspondence.

MRSI positioning in the large methanol phantom is shown in Figure 4.21a. Mapping out the external reference peak area confirmed successful localisation (Figure 4.21b). As expected, the reference signal (170ppm) was only found at the centre of the coil where the external reference sample was positioned with low level fluctuations in noise outside this region.

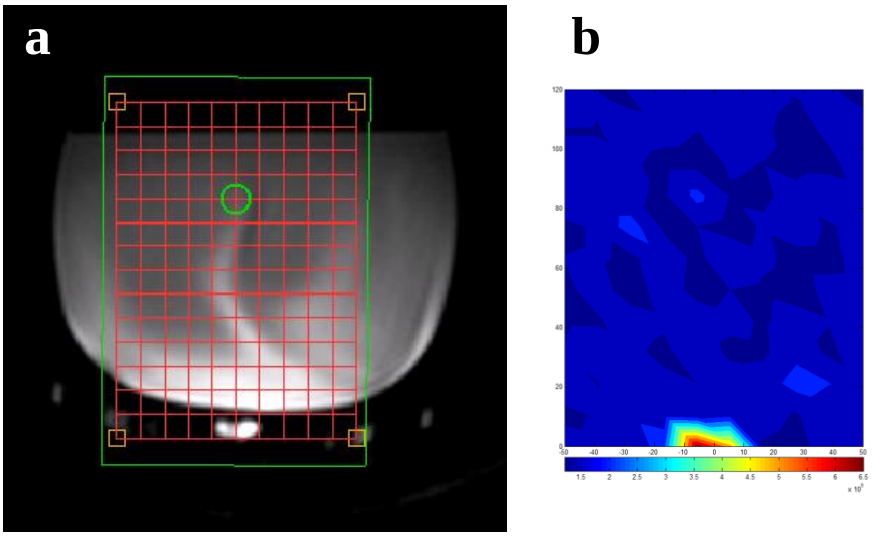

Figure 4.21 ^{13}C MRSI grid showing homogeneous methanol phantom positioning (a) and map of peak signal from external reference across the MRSI range (b). The reference sample can be seen at the bottom of both the MRI and MRSI data.

Figure 4.22 compares the methanol MRSI signal map across the homogenous phantom (a, distance from coil +20mm to +120mm) with the Biot-Savart approximation (b). The same MRSI data from Figure 4.21b were used but spectra were integrated over the methanol peak instead of the external reference peak. Maximum signal was found close to the coil wire with decreasing signal for spectra further away from the coil. The sensitivity pattern showed good agreement to the Biot-Savart method. A voxel by voxel linear regression analysis showed strong significant correlations (Figure 4.22c).

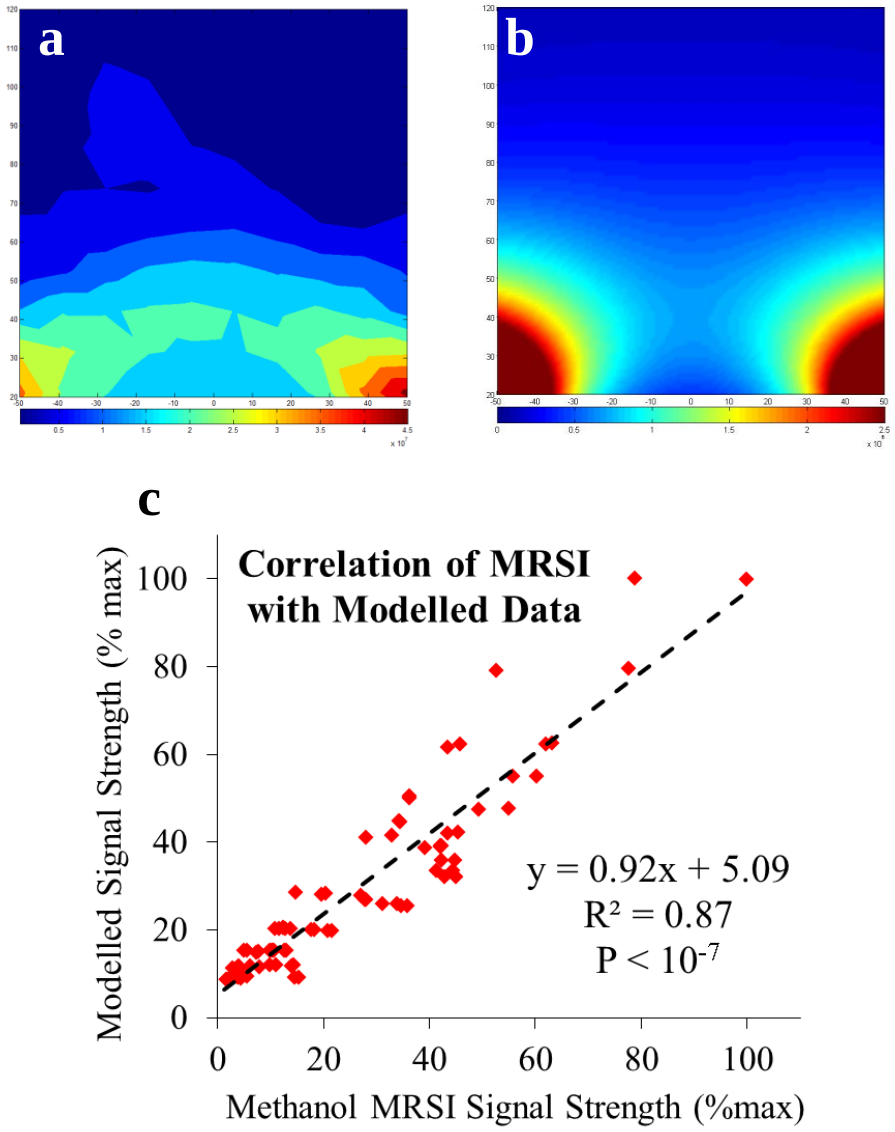

Figure 4.22 ^{13}C MRSI map of methanol signal in homogenous phantom (a) and Biot-Savart model of coil sensitivity (b); and voxel by voxel comparison of MRSI data with modelled data within the region of interest showing line equation, R^2 and P (c).

Liver Phantom Method. Figure 4.23 shows the drop in glycogen ^{13}C MRS in the large liver type phantom (blue circles). The glycogen / reference ratios drops sharply with distance close to the coil and then plateaus when the

phantom is further away. The other methods are also plotted for comparison as discussed below.

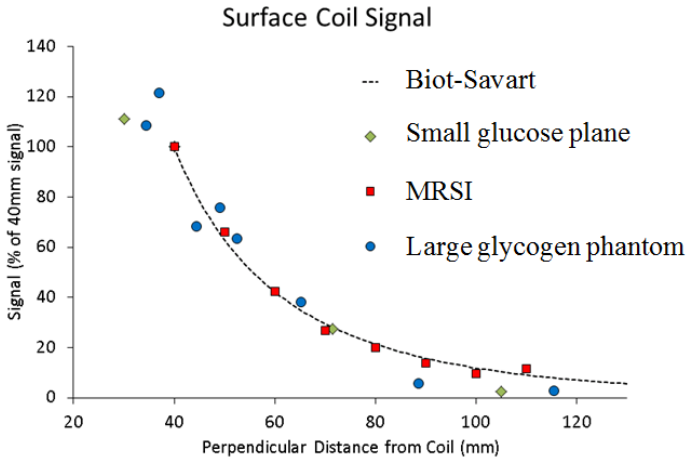

Figure 4.23 A comparison of signal drop with perpendicular distance from coil of ^{13}C MRS for 4 different methods (as labelled on legend).

Comparison between Biot-Savart Method and Phantom Methods. All methods had a similar trend in signal drop with distance from the coil (Figure 4.23) which can be approximated using a power law.

$$S \propto r^{-\alpha}$$

Equation 4.5

where S is signal, r is perpendicular distance from coil and α is a constant. Values for α vary slightly for each method as outlined in Table 4.4.

Method	α	R^2	P
Biot-Savart	2.4	1.00	$< 10^{-7}$
Small phantom	2.9	0.88	0.06
MRSI	2.4	0.98	$< 10^{-5}$
Liver phantom	3.2	0.93	$< 10^{-4}$

Table 4.2 Power law constants for signal drop using 4 different methods

4.3.4 Discussion

The results from this study showed that a Biot-Savart method can be used to successfully determine the sensitivity profile of surface coils for use in ^{13}C MRS studies.

Modelling the response of the AFP pulse across the ^{13}C MRS bandwidth suggests that the frequency range set on the Philips Achieva 3T scanner (Philips, Best, The Netherlands) has been optimised for selective inversion across the ^{1}H MRS bandwidth and not for multinuclear scanning. Because the frequency range of ^{13}C MRS is much larger only a central portion of the spectral window was inverted and therefore this pulse must be changed for inversion studies by extending the frequency sweep range. Whilst AFP pulses were not used in this thesis, this would apply to future studies and reveals the importance of modelling the pulse response before experiments.

By contrast to the AFP pulse, the AHP pulse provided an off resonance response that was highly dependent on B_1 but also seems to be optimised for

^{1}H MRS, sweeping over a smaller bandwidth. Despite this, on resonance spins achieved a much more constant excitation over varying $B_1$with an increase in response at lower B_1. In ^{13}C MRS liver studies the spectrum is centred on glycogen and as such the AHP pulse will enhance this signal compared to block pulses.

Spins down field in the spectrum experienced a lower excitation than on resonance spins and varied approximately linearly with B_1. This does not have an impact on ^{13}C MRS studies because the spectrum is centred at the glycogen signal frequency and downfield peaks are generally not considered of interest *in vivo*. However, the external reference peak used to calibrate the glycogen signal is found in this spectral region (Figure 1.1) but this is not a problem as the reference sample is in a fixed position on the coil and will effectively experience a uniform B_1 field regardless of the pulse.

The up field AHP excitation responses dipped dramatically around the starting adiabatic pulse sweep frequency (-1821 Hz) reaching almost zero for some B_1 field strengths. In ^{13}C MRS liver studies this region of the spectrum is dominated by lipid peaks which are not included in glycogen quantification. In fact, the RF pulse response modelled in this study suggests that the AHP pulse sweeping over a narrower range than the ^{13}C MRS bandwidth actually acts to suppress unwanted lipid signal and produces a beneficial effect. Whilst this pulse was chosen to be used for all studies in this thesis, future studies should compare the benefits of this lipid suppression (using a narrower frequency sweep) with a more uniform excitation across the bandwidth (using a wider frequency sweep) for real life experiments.

All three methods of signal sensitivity mapping agreed well with each other showing similar signal drops for coil-to-sample distances of less than 90 mm. The MRSI data agreed best with the Biot-Savart model. This may be explained by the fact that the Biot-Savart method does not account for noise in the spectra and so would correlate best with maps based on spectra with the greatest signal, narrowest peak width and overall largest SNR (i.e. the methanol MRSI spectra). For coil-to-sample distances greater than 90 mm the glycogen signals from both the small phantom and large liver phantoms were consistently lower than the Biot-Savart method and MRSI data (Figure 4.23) which may be an effect of the peak fitting programme not locating signal that falls below noise.

The small glucose phantom method produced the least clear signal sensitivity maps. Whilst the general pattern of sensitivity was seen in the average over planes at varying distances from the coil, the more subtle variations across the planes did not follow an easily discernible pattern due to the small size of the phantom. This method was also incredibly time consuming. In contrast to the MRSI method where signal sensitivity was simply and quickly mapped using a large homogenous sample, the small phantom repositioning method required hundreds of spectral acquisitions which were undertaken over a number of days and required much effort. The coil and phantom was also taken out and repositioned for successive scans, and new preparation steps need to be undertaken at the start of each session increasing the chance of inter session variability.

4.3.5 Relevance to *In Vivo* Liver Studies

This study emphasises the importance of surface coil position in ^{13}C MRS liver studies. The RF pulse response model combined with the Biot-Savart model will help investigators understand how the signal strength varies in an inhomogeneous B_1 field and can be used to correct acquired spectra alongside scout images. As an example, Figure 4.24 shows the signal variation inside the region occupied by the liver using a liver mask created from *in vivo* MRI data:

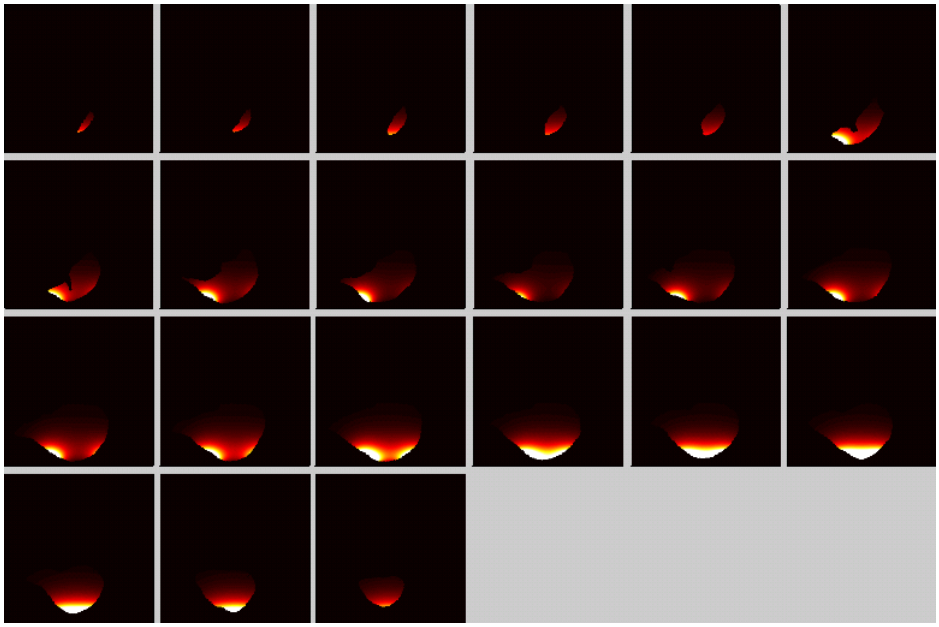

Figure 4.24 Slice by slice heat map of coil sensitivity through the liver.

Using this data, the effects of varying the coil positions with respect to the liver tissue can be considered by applying the Biot-Savart model to the liver mask and changing the current loop element positions (Figure 4.25).

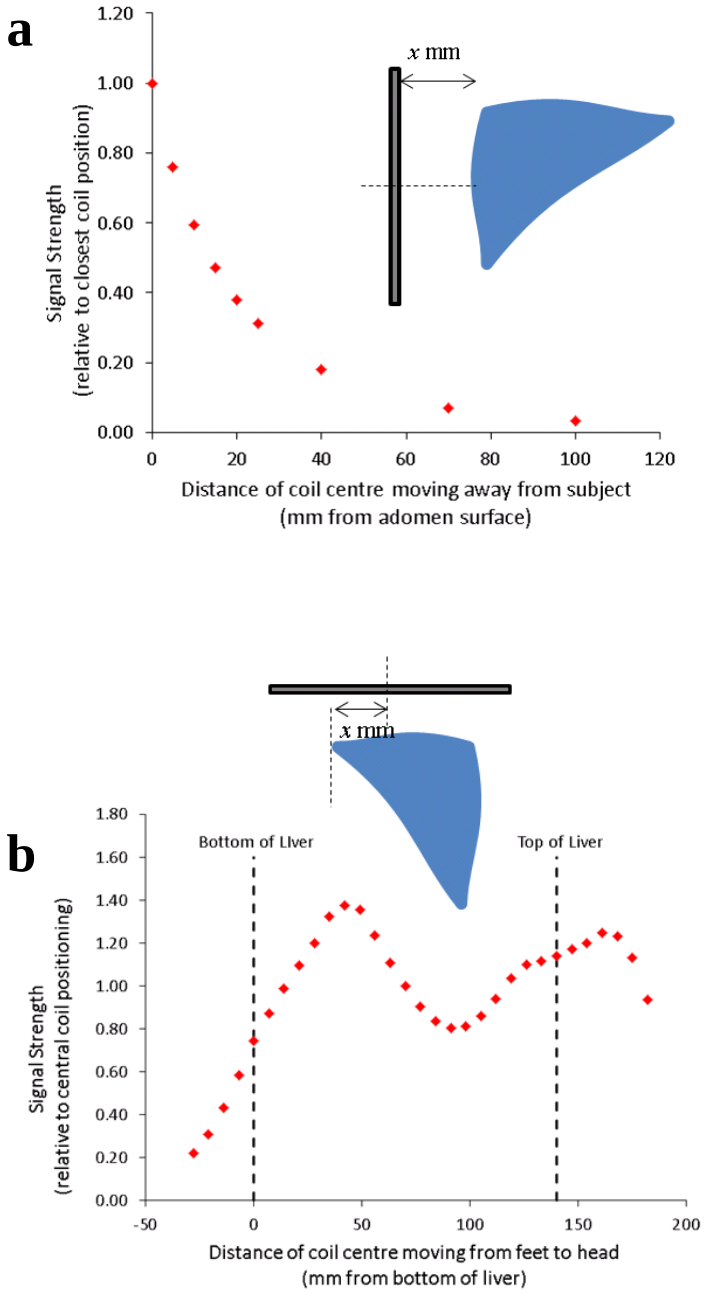

Figure 4.25 Signal strength as coil is moved in the transverse plane (a) and the sagittal plane (b).

Figure 4.25b might seem surprising as the change with distance is not symmetrical. However, this can be explained by the asymmetrical shape of the liver (Figure 4.26a). There is an increase in signal when the coil moves

downwards (towards the feet) as the top half of the coil wire moves over the largest part of the liver (Figure 4.26b). Conversely, when the coil is moved upwards (towards the head) the signal is first reduced as the upper half of the coil moves away from the larger part of the liver, and then begins to increase as the lower half of the coil begins to receive this signal (Figure 4.26c). This is illustrated below in Figure 4.26.

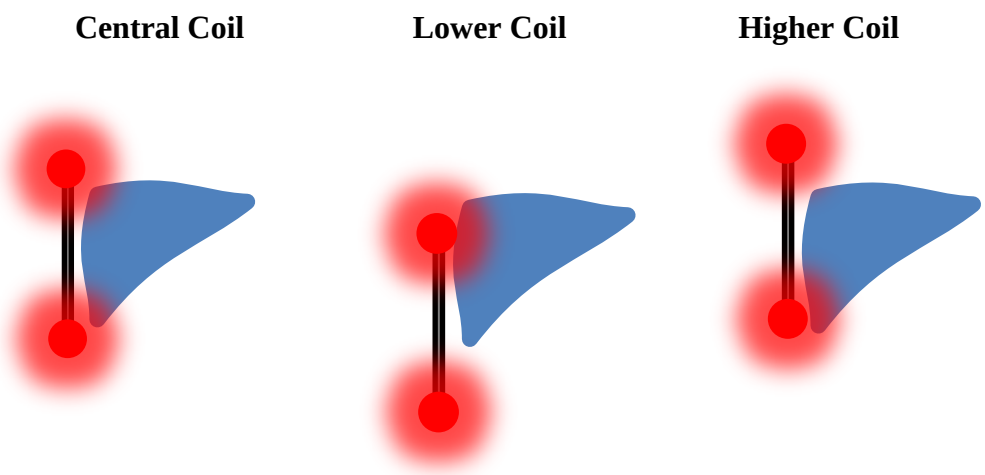

(a) Coil in central position. Contribution is greater from upper portion of liver

(b) Coil moved downwards. Signal from upper portion of the liver is greater than signal loss from lower portion, and so the net signal increases

(c) Coil moved upwards. Signal from upper portion is first reduced, net signal decreases. Continuing will increase net signal

Figure 4.26 Effects of longitudinal coil placement on receive signal.

Understanding the signal variation in this way can be used to optimise coil positioning for *in vivo* experiments as well as correcting the final acquisition using MRI data to determine the liver tissue position and correct accordingly.

In summary, this study provides a useful method of assessing the effects of B_1 field inhomogeneity across surface coils in ^{13}C MRS liver experiments. AHP pulses enhance the on resonance signal compared with block pulses largely due to the lower B_1 experienced at typical liver tissue distances form the coil, and also act to suppress lipid signal in glycogen studies. The RF pulse response in combination with the Biot-Savart model shows a strong signal close to the coil and a sharp signal drop off with distance showing the importance of correct coil positioning in *in vivo* studies.

4.4 Lower end sensitivity of *in vivo* ^{13}C MRS in the liver

4.4.1 Introduction

This section reports on a small pilot study which was undertaken to explore the effects of a low calorie carbohydrate morning intake following an overnight fast on hepatic glycogen levels *in vivo* using ^{13}C MRS. The aim was to determine whether or not ^{13}C MRS could be used to monitor the liver response to a physiological perturbation (a relatively small meal).

4.4.2 Material and Methods

Subjects

Ethical permission was obtained from the local Medical School Research Ethics Committee and all subjects provided informed written consent before participation. Five healthy subjects were recruited and studied

over two visits. All subjects were self-reported healthy male non-smokers with no known cardiovascular, metabolic or liver related diseases (mean age 21 ± 3 years; BMI 24 ± 2 kg/m3).

Study Design

Subjects were studied on two separate days in random order with a 7 day wash out period between study days. Prior to study days subjects were asked to refrain from alcohol and vigorous activity for three days. They were asked to eat the same evening meal on the nights prior to each scan day and then to refrain from consuming any food or drink except water from 10pm until they arrived at the test centre the following morning. On the morning of the study subjects were asked to refrain from vigorous activity on the way to the test centre and to arrive at 8:00am.

Protocol

Initially, natural abundance ^{13}C MR spectra were acquired from the liver to determine hepatic glycogen levels at baseline, after which subject consumed a 250ml drink of either 50g glucose solution (773 kJ) or water (0 kJ). Immediately after ingestion and thereafter at hourly intervals for 4 hours following ingestion, ^{13}C MRS were acquired to monitor any changes in glycogen levels. MR images were also obtained before each spectral acquisition to measure the volume of the liver and gastric contents.

Data Acquisition

All measurements were performed on a Philips Achieva 3T system (Philips, Best, The Netherlands) using the built in ^{1}H transmit / receive body coil for

image acquisition and a ^{13}C surface coil (PulseTeq, Surrey, UK) with quadrature proton decoupling for spectral acquisition (Figure 4.7). A T_1 weighted gradient echo sequence was acquired to measure liver volume (flip angle = 10 TE = 1.5 ms, TR = 3.1 ms, voxel size = 2 x 2 x 7 mm, 36 slices) and a T_2 weighted Turbo Spin Echo sequence was used to measure the volume of gastric contents (TE= 83 ms, TR= 1210 ms, TSE factor = 92, voxel size = 0.8 x 0.8 x 10 mm, 20 slices) using the inbuilt scanner body coil. ^{13}C spectra were acquired by placing the surface coil over the liver and marking its position on the subject's skin to give a consistent sensitive volume across subsequent time points and minimise the repositioning effects highlighted in Section 4.3 of this Chapter. The acquisition involved a $\pi/2$ pulse-acquire sequence with an AHP pulse (Section 4.3) to minimise the effects of B_1 field inhomogeneity within the volume of interest, along with narrow band proton decoupling (7000 Hz bandwidth, 512 samples, TR = 2150 ms, number of averages = 576, total scan duration ~20 mins) as previously described [10].

MRI and MRS Quantification

The liver volumes and gastric content were measured by drawing around regions of interest in Analyze9 software (Mayo Foundation, Rochester, MN, USA). Gastric emptying half-life $T_{1/2}$ was estimated from the change in gastric content with time. ^{13}C spectra were zero filled and line broadened using in house software, Lorentzian curves were fitted to the spectra and the areas of the C_1-glycogen peak (100.4 ppm) and an external reference peak were calculated. Distance from the coil was calculated from the ^{1}H MR images and

quantification achieved by comparison with a cylindrical phantom using Equation 4.10.

$$[Glyc]_{liver} = \frac{R_{liver}}{R_{phantom}}[Glyc]_{phantom}$$

Equation 4.6

where $[Glyc]_{liver}$ and $[Glyc]_{phantom}$ are the total glycogen content of the liver and phantom respectively; and R_{liver} and $R_{phantom}$are the ratios of integrals of glycogen-to-reference peaks in the liver and phantom corrected for distance to coil [28]. Masks were created from liver volume MRI data and a distance correction applied based on Equation 4.5. Distance-to-coil effects (Section 4.3) were the same because all subjects were lean and so the distances were fairly consistent across subjects.

Statistical Analysis

All statistical analysis was done using a matched pair Student's t test. The study was powered *a priori* at (1-β) = 0.8 to reach statistical significance for a 55mM rise (20% of 50g glucose to liver) from basal hepatic glycogen levels based on values and standard deviations from previous studies [11, 25]. Statistical significance was attributed at a probability of 0.05. For changes from baseline, mean difference from baseline and deviation at each time point were used to determine respective effect size and p values calculated using G power software (University of Dusseldorf, Dusseldorf, Germany). Similarly, mean differences and deviations were used to calculate p values for changes between group time-points and area under curves (AUC). Coefficients of variation

(CV%) were calculated using standard equations (inter and intra subject variability). All values are quoted as mean values ± standard error (SEM) unless otherwise stated. Glycogen data time-points are offset by 10 minutes from the time the acquisition started to represent the centre of the 20 minute ^{13}C MRS scan duration.

4.4.3 Results

Absolute Hepatic Glycogen Content

On the control day, absolute glycogen content decreased steadily from baseline (72 ± 19 g) and this drop reached statistical significance at 190 minutes and 250 minutes with reductions of 17 ± 10 g ($P < 0.05$) and 31 ± 23 g ($P < 0.05$) respectively (Figure 4.27). By contrast, on the glucose visit there were no statistically significance differences compared to baseline at any time point.

Mean glycogen content was higher during the glucose visit compared with the control visit with the greatest difference seen in the AUC across the final two time points (glucose visit: 11 ± 3 M min, control visit: 21 ± 5 M min, $P < 0.05$).

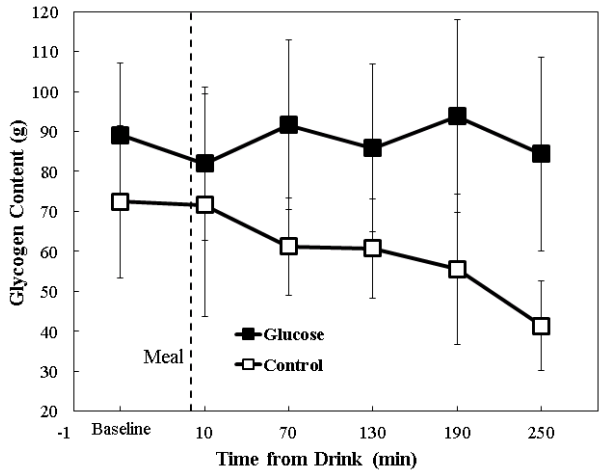

Figure 4.27 Mean (±SEM) absolute glycogen content at baseline and hourly following an 250ml oral ingestion of either 50g glucose (■) or water (□) in healthy volunteers (n = 5).

Liver Volume

There was no difference in the subjects' overnight fasted liver volumes between visits (control: 1.8 ± 0.2 L, glucose: 1.9 ± 0.2 L, P = 0.41). The intrasubject coefficient of variability (CV% = 5.6) was much lower than the intersubject variability (CV% = 23.2) across visits. During both visits changes in liver volumes from baseline were small but significant with a low standard deviation on the mean differences. Maximum change from baseline in both groups was found at t = 200 min (glucose visit: 1.8 ± 0.2 L, control visit: 1.7 ± 0.2 L).

No statistically significant change in liver volume was found between groups at any time point (Figure 4.28), with a maximum difference in % of baseline at t = 80 min (Control = 96 ± 1 $\%_{Baseline}$; Glucose = 99 ± 1 $\%_{Baseline}$; P = 0.47). At this same time point there was a significant change from baseline in the control

arm (Liver volume 1.7 ± 0.2 L, $P \leq 0.05$) whereas no significant change from baseline was found in the glucose arm ($P = 0.54$).

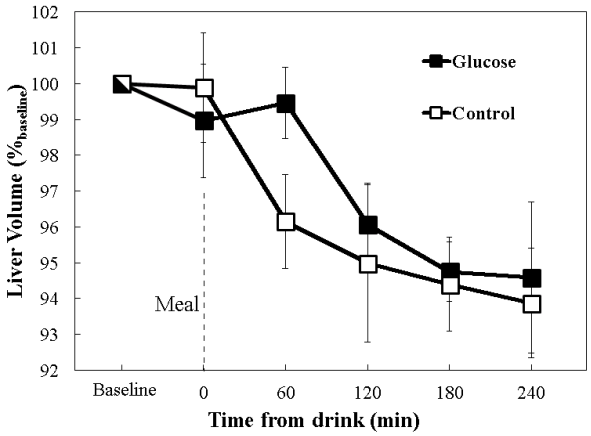

Figure 4.28 Mean (±SEM) absolute liver volume as % of baseline at baseline and hourly following an 250ml oral ingestion of either 50g glucose (■) or water (□) in healthy volunteers (n = 5).

Glycogen Concentrations

Baseline hepatic glycogen concentrations were measured to be 217 ± 38 mM for the control visit and 247 ± 32 mM ($P = 0.55$) for the glucose visit with intersubject coefficients of variation (CV%) = 17.5 and 13.0 respectively, and an intrasubject (CV%) = 32.0 across both visits (Figure 4.29). During the control visit there was a modest reduction from baseline at 190 minutes and 250 minutes to 173 ± 41 mM ($P < 0.1$) and 120 ± 23 mM ($P < 0.1$) respectively, whereas there was no change from baseline during the glucose visit.

Glycogen concentrations were higher during the glucose visit compared with the control visit. The post meal AUC across the time course was significantly

lower during the control visit (AUC = 218 ± 39 M min) compared with glucose visit (AUC = 305 ± 49 M min, P < 0.05).

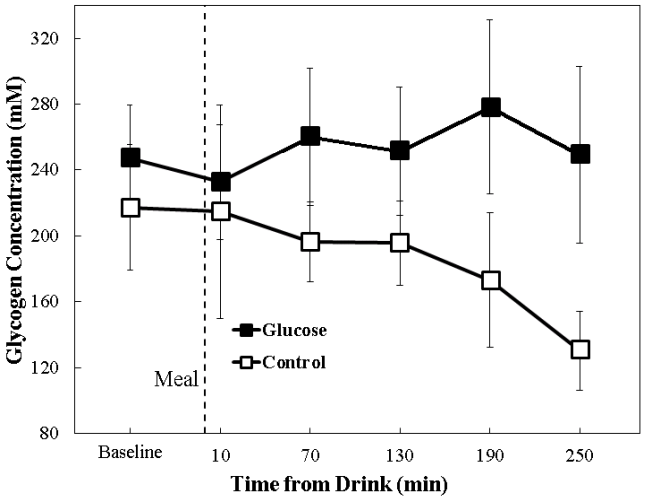

Figure 4.29 Mean (±SEM) glycogen concentration at baseline and hourly following an 250ml oral ingestion of either 50g glucose (■) or water (□) in healthy volunteers (n = 5).

Gastric Content

The subject's overnight fasted gastric content volumes remained consistent across visits (23 ± 11 ml and 20 ± 11 ml for the control and glucose groups respectively, P = 0.73). Gastric content was significantly greater than baseline at 20 minutes for both visits, with increases of 41 ± 21 ml (P < 0.01) during the control visit and 204 ± 36 ml (P < 0.001) during the glucose visit (Figure 4.30). This volume returned back to baseline at 80 minutes for the control visit, but remained significantly higher than baseline for the glucose visit (42 ± 17 ml, P = 0.007).

Gastric content volumes were significantly higher at 20 minutes for the glucose visit compared with the control visit, with a difference of 160 ± 51 ml ($P < 0.005$). Estimates of gastric emptying half-life were $T_{1/2} = 17 \pm 3$ min for the control visit and $T_{1/2} = 44 \pm 9$ min for the glucose visit, with a significant difference between groups of 27 ± 8 min ($P < 0.005$).

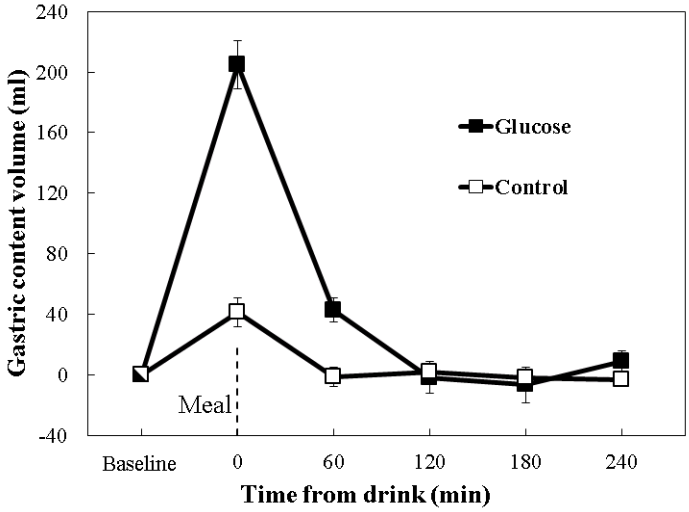

Figure 4.30 Mean (±SEM) gastric content volume at baseline and hourly following an 250ml oral ingestion of either 50g glucose (■) or water (□) in healthy volunteers (n = 5) showing gastric emptying across the time course.

4.4.4 Discussion

This preliminary study has shown that ^{13}C MRS is sensitive enough to measure the physiological rate of depletion of glycogen in *in vivo* conditions. However, during the glucose visit, changes were not sufficient to increase glycogen levels above baseline which indicates that randomized cross over studies with a

control arm are most suitable when responses cannot be accurately predicted or small changes are expected.

This preliminary study has also shown for the first time that a low carbohydrate morning meal alleviates the decline in hepatic glycogen stores, which generally results from prolonged fasting. At baseline the mean hepatic glycogen concentrations were slightly higher during the glucose visit, but this difference fell within the error range of the control visit and was not statistically significant, which is probably due to the small sample size in this pilot study. Despite the small baseline difference, it is clear from the data that the mean glycogen values decline during the course of the day following the control intake, which was not observed during the glucose visit.

The resting rate of endogenous glucose production in healthy individuals is approximately 2 mg kg^{-1} min^{-1} [77] which decreases when a meal is consumed due to an increased insulin release and suppression of glucagon. In the postprandial state absorbed carbohydrates raise blood sugar levels, resulting in an increased rate of cellular glucose intake and glycogen synthesis and storage in the liver [78]. Hepatic glycogen stores become particularly important in the fasting state as glycogenolysis and gluconeogenesis provide the energy required for the brain, renal medulla, and erythrocytes [79]. The data from the present study show that a 50g carbohydrate intake following an overnight fast is not sufficient to replenish liver glycogen levels but does prevent a further decline since hepatic glycogen levels will only increase if the amount of glucose absorbed exceeds the glucose utilisation rate. In order to fully understand this relationship, further investigations should vary the

concentration of glucose intake and measure the hepatic glycogen storage response.

Breakfast is often thought as the most important meal of the day, and research has shown that there are many associated health benefits [80]. Although nutritionists advise for individuals to consume a substantial breakfast amounting to 20% or 30% daily requirements, it is often the case in Western culture that breakfast consists of a low energy and carbohydrate rich meal, such as cereal or toast and orange juice (often less than 1000 kJ) and there has been reported to be an increasing rate of breakfast skipping in children and adolescents [81-83]. This study suggests that following an overnight fast, such low calorie meals halt further reduction in the glycogen content of the liver for up to 4 hours after consumption and provide carbohydrates directly for cells' metabolic needs. The data from the present study show that a larger energy intake is required in order to increase the glycogen content, which may have an effect on subsequent meals throughout the day.

A recent study using ^{13}C MRS observed that liver glycogen levels decline rapidly during fasting with changes from baseline at 12h and 24h after feeding [10] and a subsequent rise on refeeding. Hepatic glycogen reserves provide the main source of energy for the nervous system during this prolonged fasting period. It is generally assumed that ingested carbohydrates are distributed to both the portal vein for hepatic glycogenesis and the wider circulatory system following all feeds in a similar way [13] and current computational models assume blood glucose levels to be the only or main contributing factor [84]. In contrast, this present study shows that below a certain level of carbohydrate

intake there is no net increase in liver glycogen (i.e. no storage), suggesting a suppression of glycogenolysis and utilisation of the ingested carbohydrate by the cells and tissues. Along with other recent work [85] the data from the present study suggest that hepatic glucose metabolism is more complex than the simple model allows for.

Another factor that needs to be considered is muscle glycogen levels and a limitation of the present study is that no measurements of this depot were taken. In addition to hepatic glycogen storage, consumed carbohydrates are also transported to skeletal muscle where they can be stored as glycogen or lipids. Studies have shown that liver glycogen accounts for ~20% of carbohydrate intake [63] although it is concentrated into a smaller volume compared to muscle. Natural abundance ^{13}C MRS can also be used for measurements of glycogen storage in muscle, and a number of studies have monitored these changes following a test meal [28]. Whilst there are benefits of including these measurements into the experimental design by providing a fuller picture of energy metabolism, it has the disadvantage of increasing the scan time for subjects significantly, and also makes interleaving protocols difficult. For the purposes of this study, changes in hepatic glycogen only were considered, but future studies should weigh up the advantages and disadvantages of including muscle measurements.

The finding that gastric emptying was strongly calorie dependent is consistent with previous studies, with the emptying half-life being more than double following glucose intake compared with control feed. This is in keeping with knowledge that the amount of energy consumed relates to the gastric

throughput in the postprandial state [86] as an important factor relating the hepatic metabolism and glycogen storage. Whilst the data showed a convergence in gastric content volume between groups by 120 minutes, it is likely that different meals will have varying emptying rates. As such, this is an important additional measure that would be best included in such investigations.

Previous studies have shown that liver volume increases following test meals due to increased glycogen and lipid storage and blood flow, and whilst this present study did not show a statistically significant difference in liver volume between groups, postprandial liver volumes tended to be greater in the glucose visit compared to the control visit. At 60 minutes post consumption there was a significant decrease from baseline in the control visit which was not observed during the glucose visit, suggesting between group volumetric differences that may be observed in further studies.

This study has further reinforced the potential value of combined MRS and MRI studies as tools in investigating the metabolic effects of diet and its composition. Natural abundance ^{13}C MRS provides a powerful non-invasive *in vivo* method of monitoring glycogen levels in the liver, and can be combined with liver volume and gastric content MRI to provide a full picture of the physiological and metabolic effects of low calorie meal intake. In addition to the measurements undertaken in this study, muscle glycogen levels can also be monitored [8, 30] and both hepatic and muscular lipid levels can be obtained using ^{1}H MRS [21, 87] as discussed previously (section 4.2). Whilst these techniques have been used for many years, current advances in magnet

strength, processing software, pulse sequencing and coil design have improved signal-to-noise ratios and acquisition times, allowing more in depth data to be acquired with a higher temporal resolution.

Future experiments should explore the basic effects of increasing doses of carbohydrate consumption under normal physiological conditions *in vivo*, which would provide better models of hepatic response to meal intake and a foundation for further work. Given the increasing prevalence of metabolic disorders and liver related diseases, there is a current need for investigations into physiological responses to differing meal compositions or lifestyle choices, such as glycaemic index, interval between meals or types and regularity of exercise in healthy or obese subjects. In addition, these MRS techniques can be used to observe the effects of various feeding regimes on patients with metabolic disorders such as Type 2 diabetes or NAFLD. Alongside blood sampling for glucose and hormone measurements these experiments provide a more detailed understanding of the metabolic effects of life-style changes.

4.5 Conclusions

This chapter has explored some of the technical issues faced in MRS studies of hepatic metabolism and considered how these apply to *in vivo* studies.

Firstly, automatic post processing and analysis of ^{1}H MRS was explored. The reluctance to adopt MRS as the clinical standard in liver lipid measurements may in part be due to the difficult post processing steps and time intensive nature of analysis. Automating these processes, and using a peak fitting

algorithm, dramatically reduces the time involved and provides a more repeatable method of analysis with less subjective errors. Whilst mean fat fractions were lower for the automated processing and peak fitting algorithm in this study, the shift was consistent and correlations between automated and manual techniques were significant with a gradient close to unity. Automated techniques are likely to be more accurate as well as more repeatable because phase correction and frequency alignment uses an objective measure, producing better signal averaging.

In the second section, the impact of surface coils, commonly used in ^{13}C MRS measurements of glycogen, was explored. Given the large B_1 field inhomogeneity intrinsic to surface coil experiments, adiabatic pulses prove to induce the greatest magnetization. At 3T the precessional frequency of ^{13}C is comparable with ^{1}H at lower frequencies which meanS that a Biot-Savart model can be used to estimate B_1 field strength and signal sensitivity. Various methods used in this study confirmed the accuracy of using a Biot-Savart model which can then be applied to *in vivo* experiments. Whilst the impact of this is lessened for healthy lean subject studies due to the lower variability in subcutaneous tissue between the liver and the coil, other studies that explore patient populations should consider surface coil positioning and the Biot-Savart model can be used to correct for distance of liver tissue from the coil.

Finally, the small *in vivo* study exploring lower end sensitivity of glycogen measurements showed the importance of a control arm when small changes are expected. The study itself elucidated interesting physiological information about glycogen turnover following an overnight fast [60], but also relates to

measurement sensitivity. Error bars can be large and it is important that experiments are powered accordingly as changes may be subtle.

These technical developments lay the foundation for future studies which can combine both ^{1}H and ^{13}C MRS to investigate hepatic metabolism fully. ^{31}P MRS also provides a method of exploring ATP turnover which will be discussed in the next chapter, along with the application of these techniques in *in vivo* investigations monitoring the effects of dietary interventions.

Chapter 5 *In Vivo* multinuclear MRS Studies of Hepatic Metabolism

This chapter describes two MRS studies of liver metabolism in healthy subjects. The first investigated the immediate postprandial effects of an oral fructose challenge on ATP using ^{31}P MRS. This is set up as a potential biomarker of liver health with consideration of the relation between ATP turn over and baseline hepatic glycogen and lipid stores. The second study investigated the short and longer term effects of either low or high glycaemic index diets on hepatic lipid and glycogen reserves using ^{1}H and ^{13}C MRS.

5.1 Introduction

In the previous chapter various technical factors in MRS measures, in particular ^{1}H MRS of liver lipid levels and ^{13}C MRS of hepatic glycogen using surface coils were explored. In addition to these, ^{31}P MRS offers specific insight into ATP turnover as used in lipid and glycogen metabolism and has been shown to be related to NAFLD, NASH and other metabolic conditions.

As discussed in Chapter 1, Hepatic ATP reserves can be monitored non-invasively *in vivo* using ^{31}P MRS [35]. ^{31}P MRS can be performed in MRI scanners equipped with multinuclear capabilities and produce well resolved

peaks for each of the 3 ATP phosphate groups (α-ATP, β-ATP and γ-ATP), along with inorganic phosphate (Pi), phosphodiesters (PDE) and phosphomonesters (PME) (Phosphocreatine (PCr) is also seen in muscle tissue but not in liver). Together with ^{1}H MRS lipid measurements and ^{13}C MRS glycogen measurements these provide an insight into all the basic mechanisms of human metabolism (Chapter 3).

^{31}P MRS following fructose infusion

A number of studies have used MRS to measure postprandial fluctuations in hepatic ATP levels and ATP reserves. Phosphorylation of absorbed nutrients for energy storage converts ATP into ADP and further to AMP (Chapter 3). Generally, postprandial ATP levels are maintained in the liver, but there are some specific cases where this is not the case. Many studies, for example, have monitored ATP homeostasis using ^{31}P MRS in conjunction with an intravenous (IV) administration of fructose [6, 34, 36]. Fructose infusion is known to deplete ATP levels in the liver [88] due to a lack of phosphorylation feedback which causes the continued phosphorylation of fructose as well as activating AMP deaminase and ultimately uric acid production. This, however, is not the case during glucose intake. During fructose infusion ^{31}P MRS studies, subjects undergo continuous ^{31}P MRS immediately following bolus injection to measure minimum ATP levels and subsequent rates of replenishment. Efficiency of ATP replenishment has been shown to be impaired in obese individuals on a high fructose diet [34] and other studies have shown an inverse correlation between ATP stores and BMI, but no correlation between rates of replenishment and BMI [89]. The mean total fructose consumption in

American male adults has been estimated as 75 g/d [90] and is generally consumed in similar proportion to glucose [91]. Whilst the acute and long term effects of fructose consumption on liver lipids [4] and its connection with NASH [92] have been of much interest recently (though the data are sometimes conflicting [4, 93]), little research has been devoted to investigating the immediate ATP response to an oral fructose intake as opposed to fructose infusion. Furthermore, whilst previous studies have considered the relationship between ATP replenishment following fructose intake and BMI [89] no work has explored the relationship with hepatic lipids or glycogen.

Patients with NASH have been shown to have a reduced ability to replenish ATP following depletion [33] and it has been suggested that this inability to maintain ATP levels may prime hepatocytes to become vulnerable to injury by reactive oxygen species. Baseline hepatic ATP reserves have previously been shown to be more depleted in obese subjects [15, 34] which may be related to the increased frequency of NAFLD in the overweight population. The ability of hepatocytes to maintain adequate ATP reserves and replenish ATP levels post depletion has been hypothesised to be a critical mechanism underlying this pathogenesis [94] . In Section 5.2 the results from an *in vivo* investigation of ATP homeostasis are reported and its potential use as a clinical biomarker of progressive liver disease is discussed.

^{1}H lipid and ^{13}C glycogen MRS study of high v low glycaemic index diets

^{31}P MRS measures of ATP provide important information about the initial postprandial response to foods, in particular with nutrients thought to lead to liver damage such as fructose. However, a broader picture of energy turnover is

seen through monitoring lipid and glycogen stores which help in understanding the potential impact of dietary and lifestyle choices. These studies can go beyond the known effects of excess energy intake and lower energy expenditure and look at the impact of interventions such as macronutrient composition (e.g. carbohydrate versus fat versus protein), quality of carbohydrates (e.g. processed versus complex) or the type of exercise undertaken (e.g. high intensity versus low intensity). One intervention which has gained much recent interest is nutritional glycaemic response.

Glycaemic index (GI) was introduced a number of years ago as a way of ranking carbohydrate containing foods according to their resultant effect on blood glucose levels [95, 96] but has more recently been considered as being potentially important to diabetes, coronary heart disease and obesity [97] and low GI dietary interventions have been shown to be effective in lowering total fat mass and increasing lipid utilisation in patient studies [98, 99]. For the healthy population low GI foods have been linked with improved athletic performance [100] and improved satiety with less hunger between meals [101]. Whilst multiple studies have been published investigating the effects of high or low GI intake, it is extremely difficult to control for other contributing factors, such as overall energy consumption or fibre content, which often leads to diets not being well matched. This fact, along with glycaemic index being a relatively recent concept, has meant that there have been very few studies looking at longer term intervention of calorie and macronutrient composition matched diets with varying GI.

In Section 5.3 a randomized crossover study investigating the effects of a high versus low GI test meal and 7 day diet is reported and the impact of the results are discussed.

5.2 Investigating the effects of an Oral Fructose Challenge on Hepatic ATP Reserves in Healthy Volunteers: A ^{31}P MRS Study

5.2.1 Introduction

In this study postprandial changes in hepatic ATP reserves were monitored in response to an oral fructose challenge using ^{31}P MRS, with the ultimate goal of developing a non-invasive method of assessing liver function by measuring the rates of recovery of ATP reserves. The primary objective was to investigate the dynamic changes in hepatic ATP following an oral administration of a 500 ml 75g fructose solution, the hypothesis being that a 75g oral fructose challenge would deplete ATP levels sufficiently to be measurable using ^{31}P MRS. BMI, baseline liver lipid [21] and baseline glycogen [11] were also measured for each subject in order to explore any correlations with ATP decline and/or recovery.

5.2.2 Study Design

Ethical Permission

Ethical permission was obtained from the local Medical School Research Ethics Committee and subjects provided written informed consent before participation.

Subjects

All subjects were self-reported healthy non-obese males with sedentary lifestyles and no known metabolic disorders. All subjects consumed the oral challenge in the time required (5 minutes) and complied well with the lifestyle restrictions and scanning requirements. The mean age for all subjects was 24 ± 4 years and BMI was 25 ± 3 kg/m^2. Subjects were asked not to eat or drink anything from 10pm the previous evening (except small amounts of water).

Subjects arrived at the centre between 7:30 and 8:30am. On arrival, natural abundance ^{13}C MR spectra were acquired from the liver to determine baseline hepatic glycogen levels, and localized ^{1}H MR spectra were acquired to determine baseline hepatic lipid levels. Subjects were then asked to consume a 500ml drink of 75g fructose solution (1275 kJ) within 5 minutes. Immediately following consumption, subjects were placed in the scanner and ^{31}P MR spectra were acquired continuously for 90 minutes to assess dynamic changes in ATP. During the 90 minutes of scanning, subjects were asked to breathe regularly and remain as still as possible and were allowed to listen to the radio or music.

5.2.3 Data Acquisition

All measurements were performed on a Philips Achieva 3T system (Philips, Best, The Netherlands) using the built-in ^{1}H transmit / receive body coil for scout images and voxel placement.

ATP

Dynamic changes in phosphate metabolites were measured using localized ^{31}P MRS. A ^{31}P surface coil (Philips, Best, The Netherlands) was placed on the abdomen over the liver. Scout MR images were obtained and used for voxel placement in the right lobe of the liver (60 x 60 x 60 mm^3 voxel size). ^{31}P spectra were obtained continuously for 90 minutes using a respiratory triggered ISIS sequence with Nuclear Overhauser Effect (NOE) enhancement and proton decoupling (3 kHz bandwidth, 2048 samples, 5000 ms repetition time) as described previously [25, 102]. The voxel for β-ATP was positioned against the abdominal wall with the chemical shift of all other metabolites directed away from the wall to minimize signal leakage from the abdominal muscle (confirmed by a lack of spectral PCr peak) and maximise signal from β-ATP.

Hepatic Lipids

Baseline lipid levels were measured using the integrated ^{1}H body coil. Scout images were obtained and used for voxel placement (30 x 30 x 30 mm^3 voxel size). ^{1}H spectra were obtained using a respiratory triggered, water suppressed STEAM sequence (2 kHz bandwidth, 1024 samples, 13 ms echo time, 5000 ms repetition time, 40 averages). Two spectra were collected without water suppression for correction to absolute lipid fat fractions as described previously [25] (see Section 4.2).

Glycogen

Baseline glycogen levels were measured from ^{13}C MRS using the 14 cm diameter surface coil with integrated quadrature proton decoupling (PulseTeq, Surrey, UK) as described in Section 4.4, which was placed on the abdomen

over the liver. Scout ^{1}H images were used to determine correct placement. ^{13}C spectra were obtained using a $\pi/2$ pulse-acquire sequence (7 kHz bandwidth, 512 samples, 2150 ms repetition time, 576 averages, ~20 minutes total acquisition time) with an AHP pulse as discussed in Chapter 4 [10].

5.2.4 MRS Analysis

ATP

^{31}P spectra were processed with a 30 Hz exponential filter and data were averaged over 15 minute windows at 5 minutes intervals across the time-course. The β-ATP peak position was defined by the investigator and peak area calculated across the time course (Figure 5.1). The β-ATP peak provides a way of measuring total ATP because the phosphate signal from ADP overlaps with the α-ATP and γ-ATP peaks. The first time point was taken as a reference to measure changes in ATP and recorded as % of baseline value.

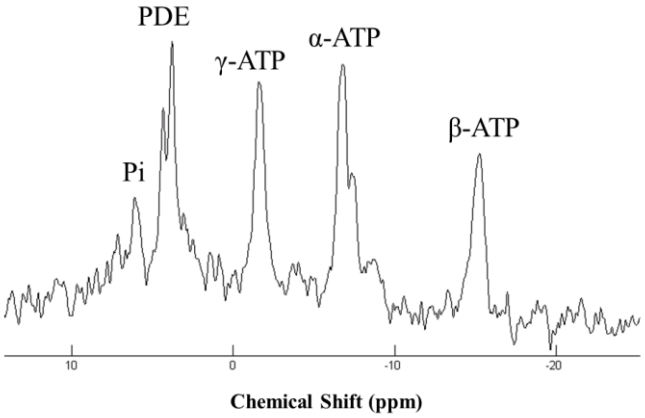

Figure 5.1 ^{31}P Magnetic Resonance Spectrum from one subjects showing signal peaks from ATP and other phosphate metabolites.

Time to reach minimum ATP levels was calculated, and the rate of recovery of absolute ATP was determined using linear fit gradients across the first 4 time points of recovery, where absolute ATP values were calculated using total phosphorous signal as a reference (β-ATP peak area / total ^{31}P signal)

Hepatic Lipids

^{1}H spectra were zero filled to 1024 datapoints and phase corrected before peak areas were calculated using the AMARES algorithm in jMRUI (Universiteit Leuven, Belgium) [103] (Lorentzian curve fitting of water peak at ~4.7ppm and -$[CH_2]_n$- at ~1.3 ppm). Water suppression was applied during spectral acquisition for better resolution of the fat peak, followed by unsuppressed spectra with identical parameters to determine the water peak area (Section 4.2). Because liver lipid levels were not the primary endpoint, T_2 correction was applied using values derived from previous healthy patients studies and lipid/water ratios used to determine absolute fat fractions as described in Chapter 4 and used in previous studies [25].

Glycogen

Glycogen concentrations were measured using the ratio of C_1 to external reference peak areas in the ^{13}C MR spectra as described in Chapter 4 [60] and published previously [28].

5.2.5 Statistical Analysis

All results are expressed as means (±SD). A repeated measures ANOVA F-test was used to determine a significant effect across the time course and a means difference T-tests were subsequently used on individual time points to

determine significant changes. Significances in correlations were determined using linear regression analysis with Pearson correlation coefficients quoted. In all cases significance was attributed to $P < 0.05$. The statistical package used for analysis was SPSS version 21 for Windows (SPSS, Inc., Chicago, IL).

5.2.6 Results

Baseline Hepatic Lipid and Glycogen

The mean baseline liver lipid fat fraction was 4 ± 3 % and correlated significantly with BMI ($R^2 = 0.48$, $P \leq 0.05$) as expected.

The mean baseline hepatic glycogen concentration was 219 ± 81 mmol/l and there were no correlations between individual values and age, BMI or baseline liver lipid levels.

ATP Reserves following Oral Fructose Challenge

Mean postprandial hepatic ATP levels began to decline from 15 minutes after the oral fructose challenge (Figure 5.2). A statistically significant variation from baseline was found across the time course (One way ANOVA F-test, $P < 0.05$). Mean values continued to decline and were significantly below the first two points at t = 30 minutes (86 ± 14%, $P < 0.05$), t = 40 minutes (85 ± 16 %. $P < 0.05$) and t = 45 minutes (84 ± 14%, $P < 0.005$) until reaching minimum at = 50 minutes (80 ± 17%, $P < 0.05$).

There was a trend for values to recover after 50 minutes, but the increase was not statistically significant compared to nadir and levels remained lower than baseline at the end of the study.

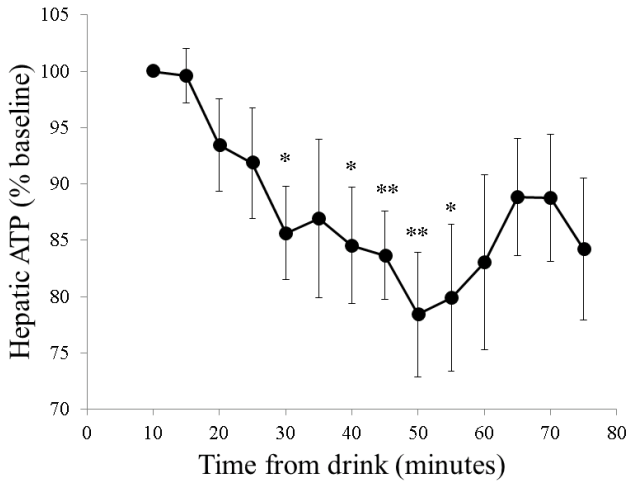

Figure 5.2 Changes in Hepatic ATP (β-ATP peak) from baseline in response to a 75g oral fructose challenge measured using ^{31}P MRS (n=9). * $P < 0.05$, ** $P < 0.005$.

No subject showed any recovery of ATP levels during the first 6 time points (until t = 40 mins). The mean AUC across this period (t=0 to t=40 mins) was 232 ± 19 % h and showed a strong negative correlation with BMI ($R^2 = 0.65$, $P < 0.01$). The average rate of decline in ATP levels over this period was 0.5 ± 0.8 % min^{-1} and was significantly correlated with both BMI ($R^2 = 0.49$, $P < 0.05$) and liver fat ($R^2 = 0.52$, $P < 0.05$) as shown in Figure 5.3.

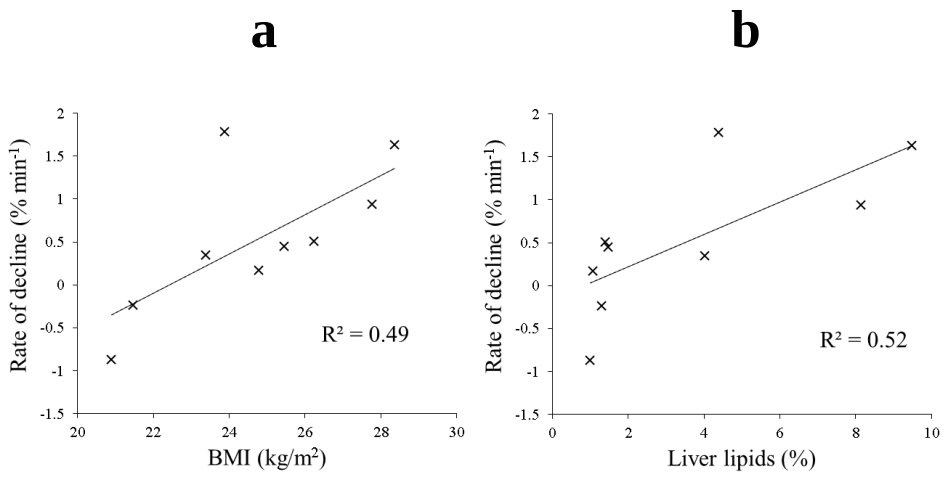

Figure 5.3 Correlation of BMI (a) and liver lipid (b) with rate of decline.

Time to minimum ATP

For two subjects the minimum ATP time point was at the end of the scanning period, and as such the final time point was taken as their time to minimum ATP (which may in fact have been after the scan period).

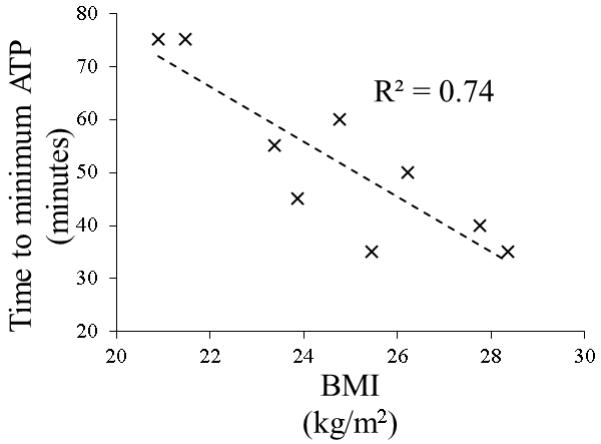

Figure 5.4 Correlation between time to minimum ATP (β-ATP peak) and BMI ($P < 0.005$).

A significant negative correlation was found between time to minimum ATP and BMI (R^2 = 0.74, P < 0.005) as shown in Figure 5.4. No such correlation was observed with age (R^2 = 0.01, P = 0.78) or baseline glycogen (R^2 = 0.003, P = 0.88) but the correlation approached significance with baseline liver fat (R^2 = 0.39, P = 0.07).

Rate of recovery

Figure 5.5 shows the relationship between rate of recovery and baseline glycogen reserves, which had a strong negative correlation that was statistically significant (R^2 = 0.71, P < 0.05). This correlation was not observed with BMI, liver fat, or any other baseline measures.

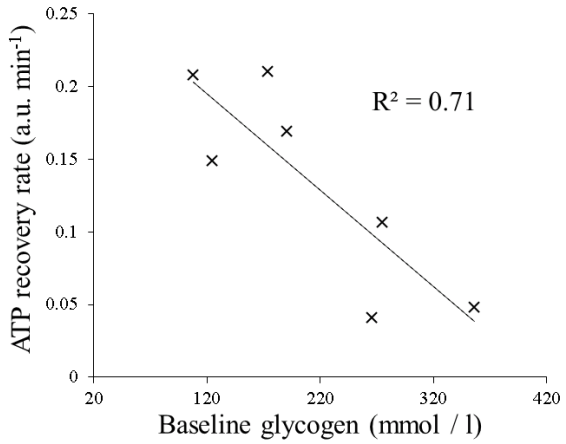

Figure 5.5 Correlation between rate of ATP recovery (β-ATP peak) and baseline glycogen levels measured using ^{31}P MRS (P < 0.05). Recovery rate is measured as the gradient of [β-ATP signal/total phosphorous signal] across the first four points of recovery.

5.2.7 Discussion

Previous studies have used *in vivo* ^{31}P MRS to monitor the depletion and replenishment of liver ATP levels following fructose infusion, and used this to investigate the relationship between ATP homeostasis and liver health. The present study has instead explored the possibility of using ^{31}P MRS following an *oral* fructose challenge, which is more physiological, more patient-acceptable and much simpler to administer than an infusion.

The results from this study showed for the first time that after oral fructose consumption there is a measurable decline in ATP reserves as estimated from the area of the β-ATP peak in ^{31}P MR spectra at 3T, followed by a partial recovery. This observation is characteristic of fructose metabolism and can be explained as a result of the immediate rapid phosphorylation of the monosaccharide. In contrast to glucose, the fructose phosphorylation enzyme fructokinase is not inhibited by ADP and citrate and as such production of fructose 6-phosphate is not regulated [104] resulting in a lower activity of the enzyme AMPK. Under normal physiological conditions an increased cellular level of AMP activates AMPK resulting in the regeneration of ATP, whereas under conditions where AMPK activity is lower (e.g. following fructose consumption) the production of uric acid is favoured over ATP via the activation of AMP deaminase (AMPD, pathway in Figure 5.6). The roles of AMPD and AMPK in the development of fatty liver disease were explored in a recent study [94] and were shown to be important in hepatic fat accumulation. In addition to this, fructose has been shown to up-regulate Glut5 (its main transporter) and Fructokinase [105], and subjects with NAFLD and a higher

intake of fructose have been shown to have a greater hepatic mRNA expression of fructokinase [106].

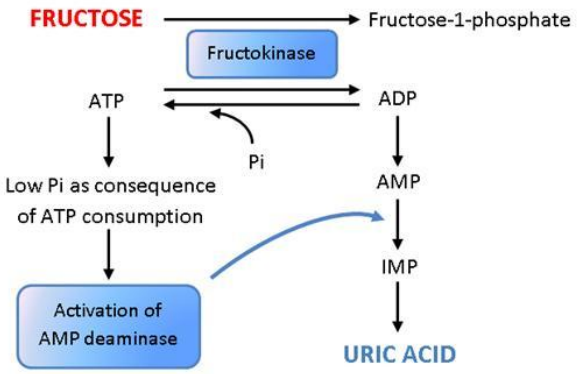

Figure 5.6 Fructose metabolism showing ATP depletion and Uric Acid production.

Eventually, following a partial decline of ATP levels, production of ATP will resume as AMPK acts to stimulate the pathways for ATP synthesis (e.g. glycolysis, fatty acid uptake, β oxidation – see Section 3.7). It is widely accepted that the inhibition of AMPK is an important part of liver lipid accumulation, which may eventually lead to steatosis and NASH [107, 108]. The hypothesis of this present study is that ATP recovery rates which provides a measure of this activity, acts as a biomarker for these progressive conditions.

Apart from infusion studies, few investigations have explored the acute effects of oral fructose on hepatic ATP levels. In a small study of 4 subjects Buemann *et al*. tested the effects of an oral dose of 30g D-Fructose and D-Tagatose on hepatic ATP reserves at 1.5T [109] and reported no drop in ATP following D-fructose consumption (however, they did find a drop following D-Tagatose which reached a maximum at 51 minutes). The data form the present study

suggests that a greater concentration of fructose and higher field strength may be required to produce significant reductions. Whilst previous studies have shown depletion in ATP reserves following fructose infusion, the data from this present study confirms the hypothesis that oral fructose intake can be used to induce a decline in hepatic ATP reserves and that ^{31}P MRS can be used to measure this effect.

In previous infusion studies the β-ATP peak tended to recover by 60 minutes, which was not the case in the present data. This is most likely due to the extra stages necessary in transferring fructose to the hepatic tissue for oral intake compared with infusion, namely gastric emptying and intestinal absorption. These factors are important considerations in all studies involving oral intake but particularly so when considering the direct effect of substrates on metabolites in hepatic tissue. Gastric emptying has been shown to be dependent on meal energy and volume [86], which becomes relevant to the technique used in this study when considering the optimum energy content and volume of the fructose challenge to induce sufficient depletion of hepatic ATP. Another relevant factor to be considered is the variation in fructose intestinal absorption rates reported in the literature. A previous study showed a high variability in intestinal absorption of fructose in healthy subjects following a 50g oral fructose drink [110]. The amount of fructose used in this study (75g in 500ml water) was sufficient for intestinal absorption and delivery to the liver in all subjects, but this factor should be considered in future experiments, and it may be that lower doses and volumes of fructose will not have the same effect.

Likewise, it is unclear if the relationship between fructose dose and ATP depletion is linear.

This study showed for the first time a negative correlation between BMI and time to minimum ATP levels. Subjects with higher BMI tended to reach minimum ATP at later time points. Given that the hepatic ATP response is a combination of ATP depletion and recovery, the findings from this study suggest that individuals with lower BMI have a more effective hepatic ATP recovery in response to a high fructose challenge. This result may be confounded by changes in gastrointestinal function, but also confirms previous studies that have shown that obese subjects have an impaired efficiency of ATP replenishment [34]. Surprisingly this correlation was not observed with liver fat levels as might be expected, although correlations with liver fat did approach significance. Previous studies have shown that there is an impaired hepatic ATP homeostasis in Type II diabetes [111] and it has been suggested that this may precede the development of steatosis in these patients [15]. It may be further hypothesised that the efficiency of hepatic ATP synthesis is reduced in the pre-diabetic population which opens up the possibility that this simple measure of ATP response might potentially provide clinically useful biomarkers of metabolic conditions. This experiment did require 2 hours of scanning on a high field MRI scanner (3T), which may be impractical and costly in a clinical setting. However, it is possible that other related measures might provide a more convenient marker. For example, in this study significant negative correlations were found between the AUC over the first 6 time points and BMI, and also between the average rate of decline in ATP reserves over

this period and both BMI and liver fat. These measures can be made over a much shorter scan duration. Future studies should consider a wider range of liver fat, as well as NAFLD and NASH patients. In particular, studies that separate BMI from liver fat to determine which of these is a better predictor of ATP homeostasis, although admittedly it would be difficult to recruit for this given the correlation between BMI and liver fat.

Observed in this study for the first time was a significant negative correlation between rates of ATP synthesis and baseline glycogen. Glycogen synthesis plays important roles in many metabolic processes in the liver, some of which are particularly relevant to fructose consumption. Studies have shown that fructose activates glycogen synthase resulting in increased glycogenesis, and also that fructose-1-phosphate produced during fructose metabolism is a competitive inhibitor of phosphorylase *a* [112] resulting in a slowed glycogenolysis. These factors result in an increase in net glycogen synthesis following fructose consumption which may indirectly impact ATP synthesis rates. The relationship between glycogen levels and ATP reserves has been explored in a number of publications and linear correlations between glycogen synthesis and ATP turnover in muscle have been reported [113] and between absolute hepatic glycogen levels and total hepatic ATP content during glycogen repletion [114]. This has been explained as the need for increased uridine triphosphate (UTP) during periods when unidirectional flux of glycogen synthesis is greater than glycogenolysis. A possible explanation for the correlations that were observed between rates of ATP synthesis and baseline glycogen levels is that there is a greater demand from glycogen in

subjects with lower baseline glycogen levels, resulting in an increased rate of glycogen synthesis and indirectly ATP synthesis. Whilst it is beyond the scope of this study to determine a causal link, the results from the present study suggest that hepatic glycogen levels are an important factor in the ATP response to fructose. These measurements are rarely factored into such studies but are clearly crucial when exploring rates of ATP resynthesis.

This study has some limitations. Firstly, breath samples were not obtained to estimate levels of intestinal fructose malabsorption [115]. Obtaining blood samples for uric acid analysis would also be a useful addition as hyperuricemia has been associated with an impaired hepatic ATP homeostasis in response to high fructose intake [15]. Secondly, histological comparisons were not made due to the ethical considerations of liver biopsies in healthy subjects. As such, although all subjects in this study had no known liver health problems this was not confirmed through histological analysis. Other studies should investigate the postprandial ATP effects in patients with NASH in comparison with healthy weight and obese people, as well as individuals with type II diabetes. Thirdly, not all subjects had begun ATP repletion by the end of the time course, and as such the rates of recovery could not be determined in two subjects. Subjects also found 500 ml of fluid difficult to consume and the scan time was long and potentially uncomfortable. Future studies should optimize the experimental protocol, in particular the scan duration, time resolution and volume or concentration of fructose challenge used.

The role of ATP homeostasis in the development of NAFLD and other metabolism related disorders appears fundamental, and further work should

explore the immediate postprandial effects of various dietary intakes. Whilst an oral fructose challenge may provide a potential biomarker of liver disease, questions still remain as to the causes and potential preventative measures of these conditions. To investigate this, ^{1}H and ^{13}C MRS provide a powerful non-invasive tool to measure hepatic energy turn over both the short and longer term – specifically glycogen levels and liver lipid accumulation (as explored in previous chapters). One dietary factor that may potentially contribute to the onset of NAFLD and other disorders is glycaemic index, which has been of increasing interest in recent years. In the next section, dietary GI is explored and the results from a randomized cross over dietary intervention study are reported and discussed.

5.3 Multinuclear MRS Investigation of the Impact of High versus Low Glycaemic Index Diets on Hepatic Metabolism: A Randomized Cross Over Study

5.3.1 Introduction

The aim of this study was to investigate the longer term effects of a calorie and macronutrient matched diet with varying GI on overall liver metabolism in healthy subjects by monitoring hepatic glycogen and lipid levels *in* vivo using MRS, alongside changes in blood glucose and insulin levels. A secondary aim was to explore whether these factors correlated with satiety levels.

5.3.2 Subjects

Ethical Permission was obtained from the local medical School Research Ethics Committee and all subject provided written consent before participation. Eight healthy subjects were recruited and studied over four visits. All subjects were self-reported healthy male non-smokers with no known cardiovascular, metabolic or liver related diseases (mean age 20.1 ± 0.4 years, Mean BMI 23.0 ± 0.9).

5.3.3 Study Design

Subjects underwent two separate 7-day diet periods with a four week washout in a randomized cross-over study. Diets consisted of either high GI (HGI) or low GI (LGI) foods, adapted from Morgan *et al*. [116] as shown in Table 5.2.

Total glycaemic index for meals and over the day were calculated using the following equation:

$$GI = \sum (C_{food}/C_{total}) \times GI_{food}$$

Equation 5.1

where C_{food} is the amount of carbohydrate contained in each digested food (grams), C_{total} is the total carbohydrate in the meal and GI_{food} is the reported glyaemic index of the food [117].

On the day before and the day after the diet week, subjects attended the Sir Peter Magnetic Resonance Centre in Nottingham for a test day (Figure 5.9).

Before beginning the study, subjects were screened for eligibility to ensure they were able to be scanned, aged between 18 and 35 years old, with a BMI between 20 and 25 kg/m^2. Subjects provided a 3 day food diary to make sure there were no abnormal eating habits or diet plans in place, and were excluded if they were heavy drinkers (more than 3 units a day), smokers, or had any known metabolic disorders or liver disease. Subjects also filled out an International Physical Activity Questionnaire (IPAQ) which was used to calculate energy expenditure to adjust dietary intervention energy intake based on basal metabolic rate using the equations defined by Henry *et al.* [118]. Prior to test days subjects were asked to refrain from alcohol and to consume the same evening meal the night before visit 1 of both diets.

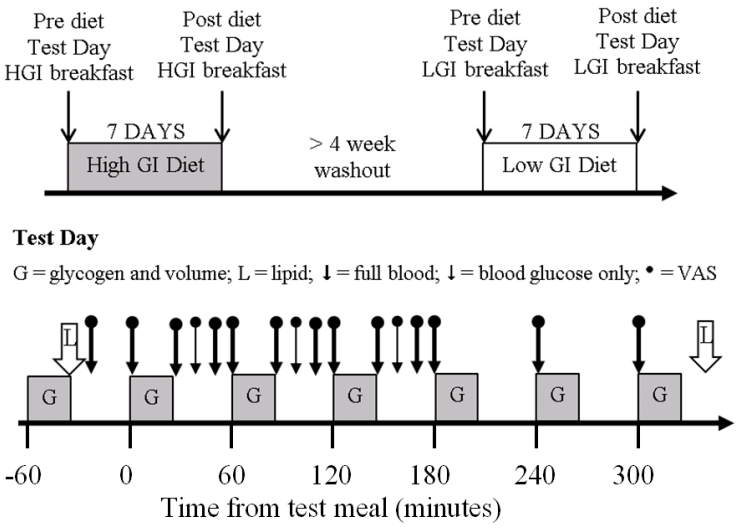

Figure 5.7. Study overview and test day.

Test Day

On the morning of the study subjects arrived at the test centre between 7:30am and 8:00am having fasted from 9pm the evening prior. On arrival, subjects were cannulated in the forearm and blood samples were taken for baseline measures. ^{13}C MR spectra were acquired from the liver to determine baseline hepatic glycogen levels, and localized ^{1}H MR spectra were acquired to determine baseline lipid levels. Baseline hunger / fullness surveys were also filled out using visual analogue scales (VAS). Subjects were then given either a HGI or LGI test breakfast (Table 5.1) corresponding to their diet week (HGI or LGI) which was to be consumed within 10 minutes. Blood samples were taken immediately post consumption (0 mins), at regular intervals for 180 mins (30, 40, 50, 60, 90, 100, 111, 120, 150, 160, 170, 180 mins) and hourly for a further 120 mins (240 and 300 mins). Hepatic glycogen levels were measured immediately following the test meal and at hourly intervals for 300 mins. Throughout the test day subjects filled out hunger / fullness surveys at the same time points as blood sampling, and at 360 minutes post consumption a final liver lipid scan was acquired.

Diet Week

During the diet week subjects were provided with all the food on the first test visit and given instructions on how to store the food. Subjects were also given a check list with quantities of food printed and space to write out any extra food consumed, along with some scales and a measuring jug. The diet quantities were adjusted using scores from the IPAQ filled out during screening and the energy intake and macro nutrient content were matched for

the HGI and LGI diets. Subjects were told to follow the diet rigidly and not to add any items, which was monitored by subjects recording when they had consumed the products, and to note any amounts left over if they really couldn't finish. There was also space each day to record any extra food or drink they had consumed. On days 1 (start of diet), day 4 (middle of diet) and day 7 (end of diet) subjects filled out hunger / fullness surveys before and after each meal to assess any changes throughout the week.

All food was purchased from the online shopping supermarket Ocado as it was difficult to source pumpernickel bread elsewhere. Subjects either carried the food home for the week or it was delivered and they were informed how to store products. Subjects were also given a contact number if they had any problems with the diet. Generally, compliance was good, but subjects did tend to struggle to finish the pumpernickel bread and some commented that they didn't feel full on either diet.

	High GI	**Low GI**
Test Meal	Sultana Bran (90g) Skimmed Milk (180ml) Water (170ml) Glucose (15g)	All Bran (80g) Semi Skimmed Milk (150ml) Orange Juice (200ml)
Energy	420 kcal	420 kcal
Fat	3g (7%)	4g (8%)
Protein	13g (12%)	14g (13%)
Carb	84g (81%)	83g (78%)
GI	88	42

Table 5.1 Test day breakfast.

	High GI Diet					
	Weight (g)	Energy (kJ)	Fat (g)	Protein (g)	Carbohydrate (g)	GI
Breakfast						
Sultana Bran	90	1226	2	7	61	90
Skimmed Milk	180	234	1	5	7	48
Water	170	0	0	0	0	0
Glucose	15	247	0	0	15	100
Breakfast Total		**1754**	**3**	**13**	**84**	**88***
Lunch						
Fruit Loaf	144	1674	6	10	77	90
Margarine	25	799	19	0	0	0
Strawberry Yoghurt	125	418	1	3	20	85
Skimmed Milk	120	156	1	3	5	48
Lunch Total		**3078**	**27**	**17**	**103**	**87***
Dinner						
Cottage Pie ready meal	300	1004	8	15	26	65
Medium Cheddar	35	603	12	9	0	0
Strawberry Yoghurt	125	418	1	3	20	85
Water	200	0	0	0	0	0
Glucose	30	494	0	0	30	100
Mars Bar	58	1029	10	2	38	68
Dinner Total		**3548**	**31**	**29**	**114**	**79***
Day Total		**8380 kJ**	**61 g**	**59 g**	**301 g**	**84***
Energy Proportions		**2002 kcal**	**28%**	**12%**	**61%**	

	Low GI Diet					
	Weight (g)	Energy (kJ)	Fat (g)	Protein (g)	Carbohydrate (g)	GI
Breakfast						
All Bran	80	1092	1	8	56	42
Semi Skimmed Milk	150	314	3	5	7	25
Orange Juice	200	352	0	1	20	50
Breakfast Total		**1758**	**4**	**14**	**83**	**42***
Lunch						
Pumpernickel Bread	180	1414	2	9	70	41
Margarine	12	377	10	0	0	0
Black Cherry Yoghurt	150	837	9	5	24	17
Probiotic Orange	200	544	2	4	23	30
Lunch Total		**3172**	**23**	**18**	**117**	**34***
Dinner						
Lasagne ready meal	280	1159	7	14	37	28
Apple	133	268	0	0	15	38
Fruit and Nut	90	1715	24	6	42	15
Semi Skimmed Milk	150	314	3	5	7	25
Dinner Total		**3456**	**34**	**25**	**101**	**24***
Day Total		**8386 kJ**	**61 g**	**57 g**	**301 g**	**32***
Energy Proportions		**2004 kcal**	**28%**	**12%**	**61%**	

*Calculated from GI proportional contribution to total carbohydrate (Equation 5.1)

Table 5.2 Overview of 7 day diet.

5.3.4 Data Acquisition

Blood Samples

Prior to the test day the equipment were carefully labelled with the subject number, time point and visit number and set out ready for the scan day (Figure 5.7). During the test day two subjects were interleaved, which required careful planning and management to ensure smooth running. This was most difficult on days were there was a problem with some data points, but did reduce the number of days involved and price of the study. Scan day flow charts and diaries were strictly followed and helped to co-ordinate the multiple personnel involved.

Blood was obtained from the forearm and drawn into fluoride/oxalate tubes for blood glucose analysis and EDTA tubes for insulin analysis. Immediately following collection, blood was stored on ice and then centrifuged on site. Plasma was separated off and stored at -80^{0}C at the Queens Medical Centre (QMC), Nottingham.

Figure 5.7 Photo of labelled centrifuge tubes and blood vials.

Blood glucose analysis was undertaken in the Queen Medical Centre Human Physiology Department using a YSI 2300 STAT Plus^{TM} Glucose and Lactate Analyser (YSI, UK). Insulin measurements were also conducted internally at the QMC using a Millipore HI-14k kit (Missouri, USA).

MRS

All measurements were performed on a Philips Achieva 3T system (Philips, Best, The Netherlands) using the built in ^{1}H transmit / receive body coil for image acquisition and the ^{13}C surface coil (PulseTeq , Surrey, UK) described in Section 4.3 for spectral acquisition. A T_1 weighted gradient echo sequence was acquired to measure liver volume (flip angle = 10 TE = 1.5 ms, TR = 3.1 ms, voxel size = 2 x 2 x 7 mm, 36 slices) and a T_2 weighted Turbo Spin Echo sequence was used to measure the volume of gastric contents (TE= 83 ms, TR= 1210 ms, TSE factor = 92, voxel size = 0.8 x 0.8 x 10 mm, 20 slices).

^{13}C MR spectra were acquired by placing the surface coil over the liver and marking its position on the subject's skin to give a consistent sensitive volume across subsequent time points, as was shown to be important in Section 4.3 (all subjects were lean which reduced the coil-to-sample distance effects). The acquisition involved a $\pi/2$ pulse-acquire sequence with an AHP pulse along with narrow band proton decoupling (7000 Hz bandwidth, 256 samples, TR = 959 ms, number of averages = 888, total scan duration ~20 mins) as adapted from previous routines used in Chapter 4 and published previously [60].

^{1}H MR spectra were acquired using a Philips XL torso coil (Philips, Best, The Netherlands) shown in Figure 5.8. Scout images were obtained and used for voxel placement (30 x 30 x 30 mm voxel size). ^{1}H spectra were obtained using

a respiratory triggered, water suppressed PRESS sequence (2 kHz bandwidth, 1024 samples, 5000 ms repetition time, 40 averages) at 4 different TEs (40ms, 50ms, 60ms and 80ms). A water unsuppressed spectrum was acquired with half the averages to determine lipid fat fractions as described previously [25].

Figure 5.8 XL Torso coil used for high quality ^{1}H MRS.

Surveys

Appetite was assessed using validated paper VAS ratings [119]. At each time point subjects answered each of five mixed appetite questions – "1. How hungry do you feel", "2. How satisfied do you feel", "3. How full do you feel?", "4. How strong is your desire to eat" and "5. How much do you think you can eat". Terms expressing the notions 'extremely' and 'not at all' were anchored at either end of a 100-mm horizontal line printed below each questions. Participants placed a small mark intercepting the horizontal line to correspond to the subjective response to each question. All ratings where scored on a scale from 0 to 100 using a ruler to measure the closest millimetre were the mark crossed so that higher scales indicate greater subjective sensations [120]. For comparison of the pre diet test days the overnight fasted

VAS scores were used as a reference and values are expressed as a change from baseline. For variation between pre and post diet test days, absolute VAS scores were used.

5.3.5 MRS Analysis

MRI

Gastric content and liver volume were measured by visually adjusting the image contrast for optimal viewing and drawing around regions of interest for each slice using the Analyze9 software (Mayo Foundation, Rochester, MN, USA).

Liver Glycogen Stores

Liver glycogen levels were quantified by comparison with a liver sized phantom of known concentration, as described in Section 4.4.2 [28]. Because all subjects were lean and the distance between coil and liver did not vary much between subjects a distance correction was not applied.

Hepatic Lipids

Liver lipid levels were quantified using methods similar to those described in Section 5.2.5, however individual T_2 values were determined from varying TE acquisitions as shown to be important in Section 4.2.

Spectra acquired at 4 different TEs (40ms, 50ms, 70ms, 80ms) were automatically post processed using the software developed in Section 4.2 and the peak fitting algorithm was used to determine fat fraction as published previously [25].

5.3.6 Statistical Analysis

All results are expressed as means (±SEM). A repeated measures ANOVA F-test was used to determine significant main effect across the time course, and a means difference T-test was used on individual time points and AUCs to determine significant changes. In all cases significance was attributed to $P < 0.05$. The statistical package used for analysis was SPSS version 21 for Windows (SPSS, Inc., Chicago, IL).

Despite the procedure being fully explained to volunteers and informed consent obtained, one subject did not respond well to needles and blood samples could not be obtained on any test day reducing the overall sample size of blood measurements to $n = 7$. In addition to this, personnel struggled to obtain blood samples from one subject on the pre high GI diet visit, and another subject on the post low GI diet visit. As this was a randomized cross over study, in the following results statistical T-tests included only subjects with repeated measures, and the adjusted sample sizes are quoted.

5.3.7 Results

Blood Samples

Pre diet blood glucose levels: The blood glucose response to the LGI and HGI test breakfasts during visit 1 are shown in Figure 5.9a. Blood glucose levels rose significantly above baseline following the test meal on both test days, peaking at 35 minutes post consumption ($n = 5$; HGI, $P = 0.001$; LGI, $P < 0.05$). Glucose concentrations immediately following consumption were significantly higher during the HGI visit compared with the LGI visit ($P <$

0.005) and reached a maximum at the 35 minute measurement (n = 5, HGI, 8.4 ± 0.4 mmol/l; LGI, 6.2 ± 0.4 mmol/l; P < 0.05). The AUC for changes in blood glucose from fasted state across a 2 hour time course (glycaemic index) was 107 ± 26 mmol/l min following the HGI breakfast and 36 ± 7 mmol/l min following the LGI breakfast.

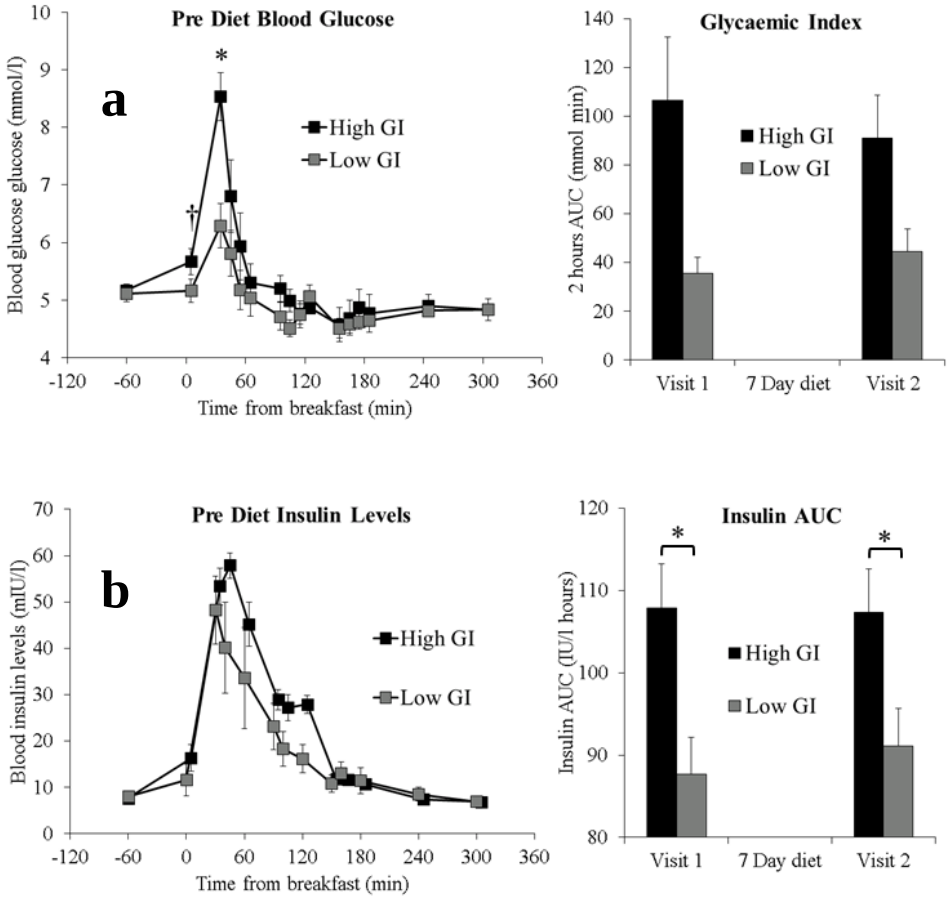

Figure 5.9 Blood glucose (a) and insulin (b) response HGI (black) and LGI (grey) test meals *P < 0.05.

Post diet blood glucose levels: The glycaemic response (AUC over 120 minutes) after the 7 day diet fell within error range of pre diet levels for both

the HGI post diet visit (91 ± 17 mmol/l min; P = 0.78) and LGI post diet visit (45 ± 9 mmol/l min; P = 0.49, n = 5).

Insulin Levels

Figure 5.9b shows the blood glucose response to the HGI and LGI test breakfasts during visit 1. Insulin levels rose sharply in response to the breakfast followed by a slower decline back to baseline.

The insulin response was greater for HGI compared LGI, with significant differences in AUCs on both the pre diet (HGI 108 ± 6; LGI 88 ± 5 IU/l h; n = 6, $P < 0.05$) and post diet test day (HGI 107 ± 5; LGI 91 ± 5 IU/l h; n = 6, $P \leq 0.01$) (Figure 5.9).

There was no significant effect of the 7 day HGI or LGI diets, with pre diet and post diet value remaining similar (n = 6, HGI P = 0.66, LGI P = 0.90).

Gastric Content

Gastric content volume rose immediately following consumption and slowly emptied over the time course as expected (Figure 5.10). Values immediately following test meal and the AUC across the time course were significantly greater during for LGI (Peak = 477 ± 21 ml, AUC = 5.9 ± 0.6 l hours) compared with HGI (Peak = 361 ± 30 ml , AUC = 4.4 ± 0.4 l hours) on the pre diet visit (Peak $P < 0.001$, AUC $P < 0.05$).

The AUC in gastric content increased following the 7 day HGI diet and decreased following the 7 day LGI diet compared to pre diet values (Two way F-test, $P < 0.005$).

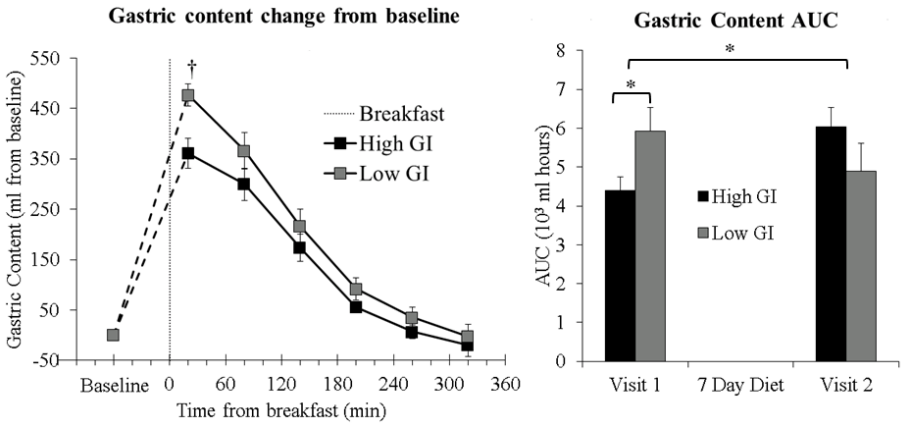

Figure 5.10 **Gastric content across the test days for high and low GI diets († P < 0.005, * P < 0.05).**

Liver Volume

Fasted liver volumes before the7 day diet were consistent across HGI (1.7 ± 0.1 l) and LGI (1.7 ± 0.1 l) visits and showed strong correlations ($R^2 = 0.8$, $P \leq 0.001$). There was no significant change in liver volume across the time course or between visits.

Liver Glycogen Pre diet test day

Mean baseline liver glycogen concentrations before the 7 day diet were consistent across HGI (288 ± 37 mmol/l) and LGI (273 ± 32 mmo/l) visits (T-test, P = 0.67).

Low GI breakfast. Following the test breakfast hepatic glycogen levels increased from baseline for the first 180 minutes and then began to decline until the end of the test day (Figure 5.11) showing a significant effect across the time course (One way repeat measures F-Test, $P \leq 0.01$). There was a statistically significant percentage rise from baseline at 60 minutes (15 ± 6 %,

$P < 0.05$) and 180 minutes (14 ± 6 %, $P < 0.05$), followed by a significant decline to 85 ± 10 % at 300 minutes post consumption compared to 60 minutes ($P \leq 0.01$) and 180 minutes ($P < 0.05$).

High GI breakfast. Following test meal hepatic glycogen levels tended to increase from baseline throughout the full test day (Figure 5.11) but did not reach significance above baseline.

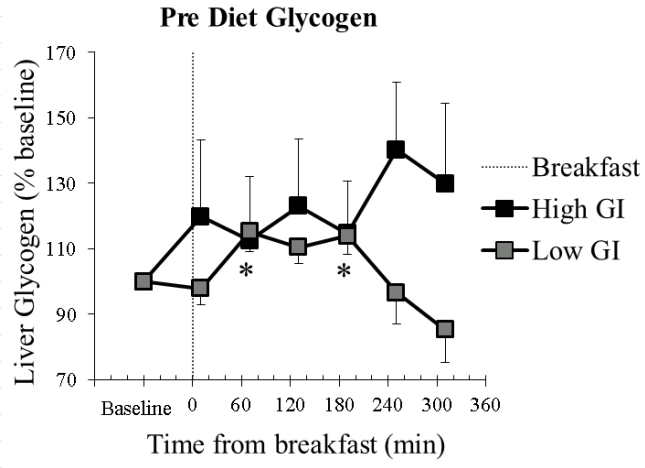

Figure 5.11 Postprandial response to a high or low GI breakfast on the pre diet baseline test day (*$P < 0.05$).

Comparison between test meals. The inter subject variability in percentage change from baseline following the HGI breakfast was much higher than the LGI breakfast as seen by the increased error bars for the high GI arm on Figure 5.11. The average inter subject coefficient of variation (CV) post consumption was significantly higher during the high GI visit (HGI CV = 48%; LGI CV = 20%; $P \leq 0.001$).

Mean hepatic glycogen concentrations were similar up to 180 minutes post consumption for both HGI and LGI pre diet test meals, after which levels continued to rise for HGI and began to decline for LGI (Figure 5.11). There was a statistically significant effect between test meals across the time course (two way repeat measures F-test, $P < 0.05$). Absolute glycogen concentrations where significantly higher at 240 minutes following consumption of HGI breakfast (359 ± 31 mmol/l) compared with LGI (256 ± 33 mmo/l, $P \leq 0.01$).

Liver Glycogen following 7 day diet

Compared to pre diet levels, fasted liver glycogen tended to be higher following both the 7 day HGI (131 ± 13 %) and LGI (120 ± 19 %) diets (Figure 5.12a) but only reached significance for HGI (HGI $P \leq 0.05$; LGI $P = 0.34$) .

Glycogen levels continued to be higher across the time course following the HGI diet compared with LGI, with the AUC increasing from 13.13 ± 0.99 mol/l h to 14.46 ± 1.44 mol/l h for the high GI diet and from 11.74 ± 1.14 mol/l h to 11.98 ± 0.88 mol/l h for the low GI diet (Figure 5.12b). Despite a larger increase in AUC following the high GI diet statistical significance was not reached ($P = 0.10$).

Compared to pre diet levels, the maximum liver glycogen concentration across the time course was significantly higher following the HGI diet (pre diet 404 ± 31 mmol/l; post diet 457 ± 33 mmol/l; $P < 0.05$) but not for the LGI diet (Figure 5.12c). There was also a significance difference in maximum glycogen levels between HGI and LGI on post diet test days (LGI post diet 393 ± 24 mmo/l, $P < 0.01$).

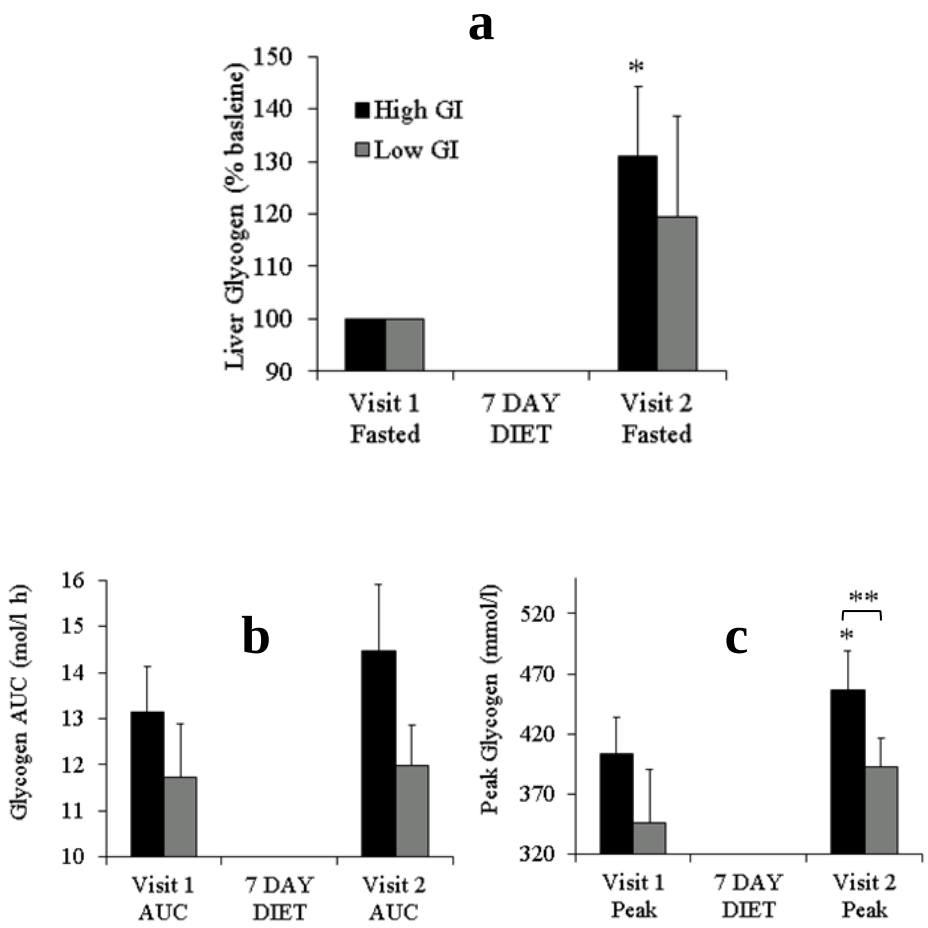

Figure 5.12 Fasted glycogen levels (a), test day glycogen AUC (b) and test day peak glycogen levels (c) show pre and post diet test days for high and low GI diets (*P < 0.05, **P<0.01).

Liver Lipids

On the pre diet test day, fasted liver lipid levels where consistent across HGI and LGI visits (HGI = 2.4 ± 1.2 %; LGI = 2.4 ± 1.0 %; T-test P = 0.82). At the end of the test day liver lipid levels were still within error range of fasted levels, although during the HGI visit mean values had increased slightly (HGI end of day = 3.1 ± 1.4%; P = 0.28). The inter subject coefficient of variation stayed consistent across all lipid scans (45 ± 1%)

On post diet test days, fasted liver lipid levels were higher than pre diet fasted levels for HGI (4.7 ± 2.0 %) and lower than pre diet fasted levels for LGI (1.6 ± 0.7 %) reaching statistical significance (Two way repeated measures F-test, $P < 0.05$). Lipid levels remained consistent for end of day measurements and LGI end of day measurement was significantly lower for post compared with pre diet test day ($P < 0.05$) as shown in Figure 5.13.

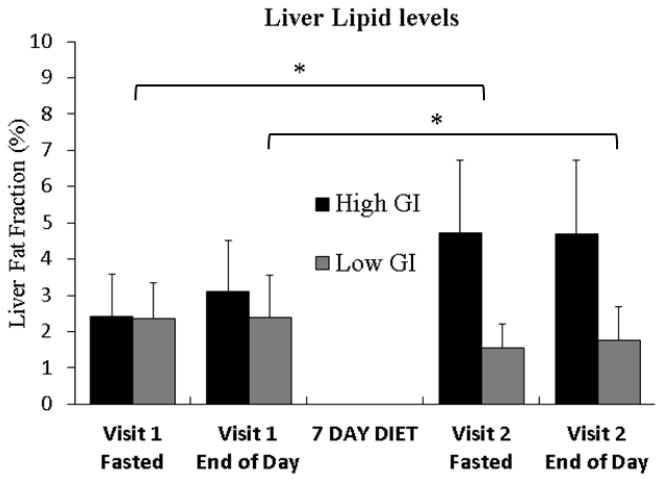

Figure 5.13 Hepatic lipid levels at the start and end of pre and post diet test days for the high and low GI diets (*P<0.05).

Subjective Appetite Ratings - Scan Day

Figure 5.14 shows the subjective appetite ratings (VAS scores) in response to a HGI or LGI test breakfast.

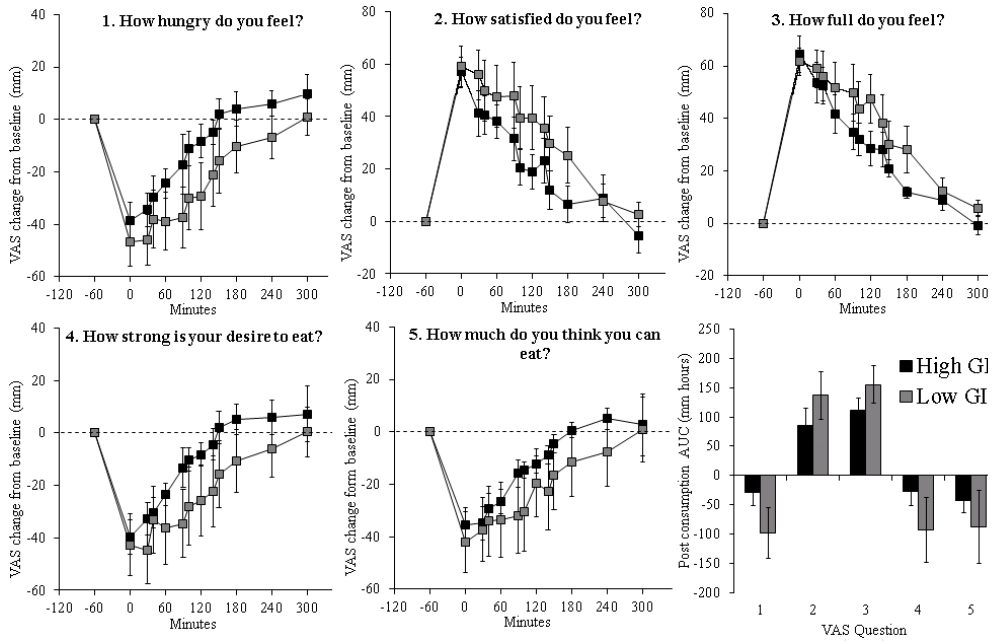

Figure 5.14 VAS rating in response to 5 questions and the AUC across the time course for the high and low GI diets.

Hunger Scores

On all four test days change from baseline hunger ratings, desire to eat and amount of food subjects thought they could consume reduced significantly following both LGI and HGI breakfasts ($P < 0.001$) and slowly rose back to baseline and further over the time course (Figure 5.14). During the pre-diet test day these visual scores tended to be higher across the time course following the HGI breakfast compared with LGI (i.e. more hungry) but did not reach statistical significance across the time course or in the AUC ($P = 0.2$).

Fullness Scores

On all four test days change from baseline fullness and satisfaction ratings increased significantly following both the LGI and HGI breakfast ($P < 0.001$) and slowly decreased back to baseline and further over the time course, the

converse of hunger related scores as expected (Figure 5.14). During the pre-diet test day these visual scores tended to be higher across the time course following the LGI breakfast compared with HGI (i.e. more full) but did not reach significance. The mean difference between LGI and HGI visit fullness rating AUCs across the time course approached significance (High GI, 112 ± 20 mm hours; Low GI, 156 ± 32 mm hours; P = 0.076).

Pre diet versus Post Diet

Post diet VAS scores were similar to pre diet VAS scores (Figure 5.15) with no statistical significance differences in AUCs across the test day. Following the 7 day HGI diet scores for satisfaction and fullness tended to be larger compared to pre diet and there was a significant percentage increase in overnight fasted fullness scores post diet compared to pre (3.6 ± 1.2 %, P = 0.017).

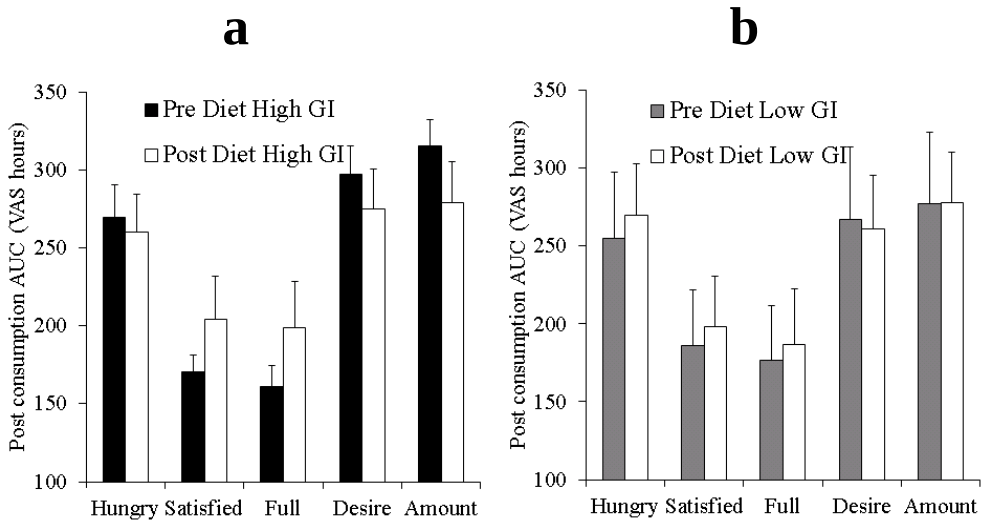

Figure 5.15 VAS AUC across pre and post diet test days for the high GI (a) and low GI (b) diets.

Subjective Appetite Rating – Take Home

The take home surveys were not consistently filled out by volunteers. During the HGI diet, two subjects forgot to fill out Day 7 VAS scores, and during the LGI diet one subject forgot to fill out Day 7 VAS scores. In addition, during the LGI diet one subject forgot to bring back his take home survey and has not returned it since (he reported to have kept the diet well). This reduced the sample size to n = 7 for comparison including LGI VAS scores, n = 6 for comparison including HGI VAS scores for day 7 or LGI VAS scores for day 7 and n = 5 for comparisons between both diets that include VAS scores for day 7.

Figure 5.16 shows the sum of the VAS scores for each question on day 1, day 4 and day 7 during the LGI an HGI diets. During the HGI diet there was a significant increase in total hunger ($n = 8$, $P < 0.005$) and desire to eat ($n = 8$, $P < 0.05$) ratings from Day 1 to Day 4 and a significant decrease in total satisfaction ratings ($n = 8$, $P < 0.05$) from Day 1 to Day 4. Total hunger and desire to eat ratings across the week tended to be higher (Figure 5.16f) but did not reach statistical significance possibly due to the small sample size ($n = 5$, $P = 0.3$).

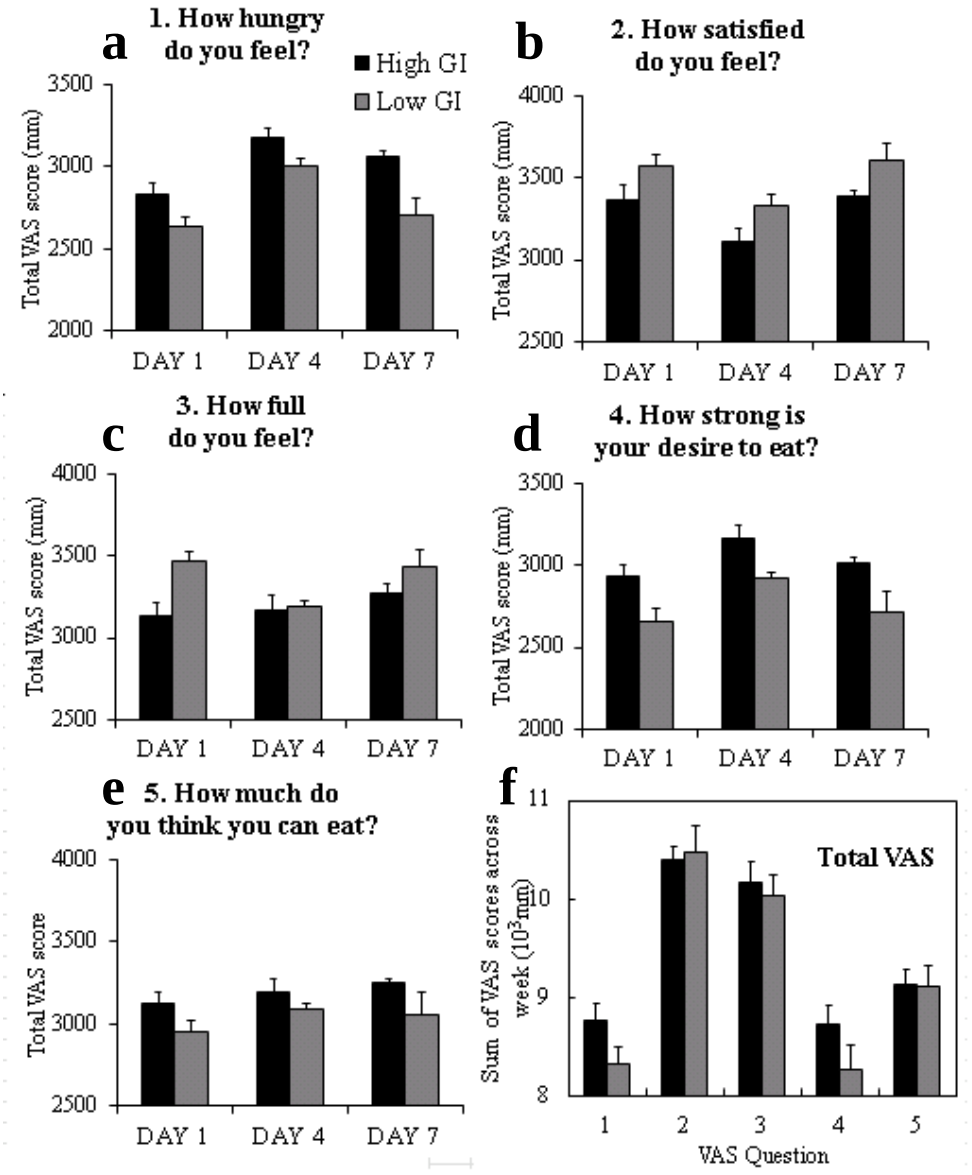

Figure 5.16 Total sum of VAS scores on Day 1, 4 and 7 during the diet week, questions 1 – 5 shown in a – e, and sum across week shown in f.

At the end of between meal periods the percentage change from baseline values show that hunger ratings, desire to eat and amount subjects thought they could consume tended to be higher during the HGI diet compared to the LGI diet (Figure 5.17). Notably, during the HGI diet hunger levels elevated from

baseline rapidly and remained high during Day 4 and Day 7 (Figure 5.17a). Overnight fasted hunger scores and desire to eat were significantly elevated on Day 4 of both the LGI ($P < 0.05$) and HGI ($P < 0.05$) diets with no significant difference between diets.

5.3.8 Discussion

The aim of this study was to investigate the effects of a 7 day high versus low GI diet on hepatic metabolism and satiety in healthy subjects using multinuclear MRS and blood sampling.

The glycaemic response to both test meals was as expected, with blood glucose levels peaking at significantly higher levels following a HGI compared with a LGI breakfast on both the pre and post diet test days. These observations are in strong agreement with Morgan *et al* [116] for both the peak height and timing of blood glucose levels in response to the same test breakfast as used in their study.

From the calculated glycaemic index values the LGI breakfast should have produced a glycaemic response which was 48% of the HGI breakfast. The results showed the LGI blood glucose response nearer 34% of the HGI breakfast on the pre diet test day which rose to nearly 50% on the post diet visit.

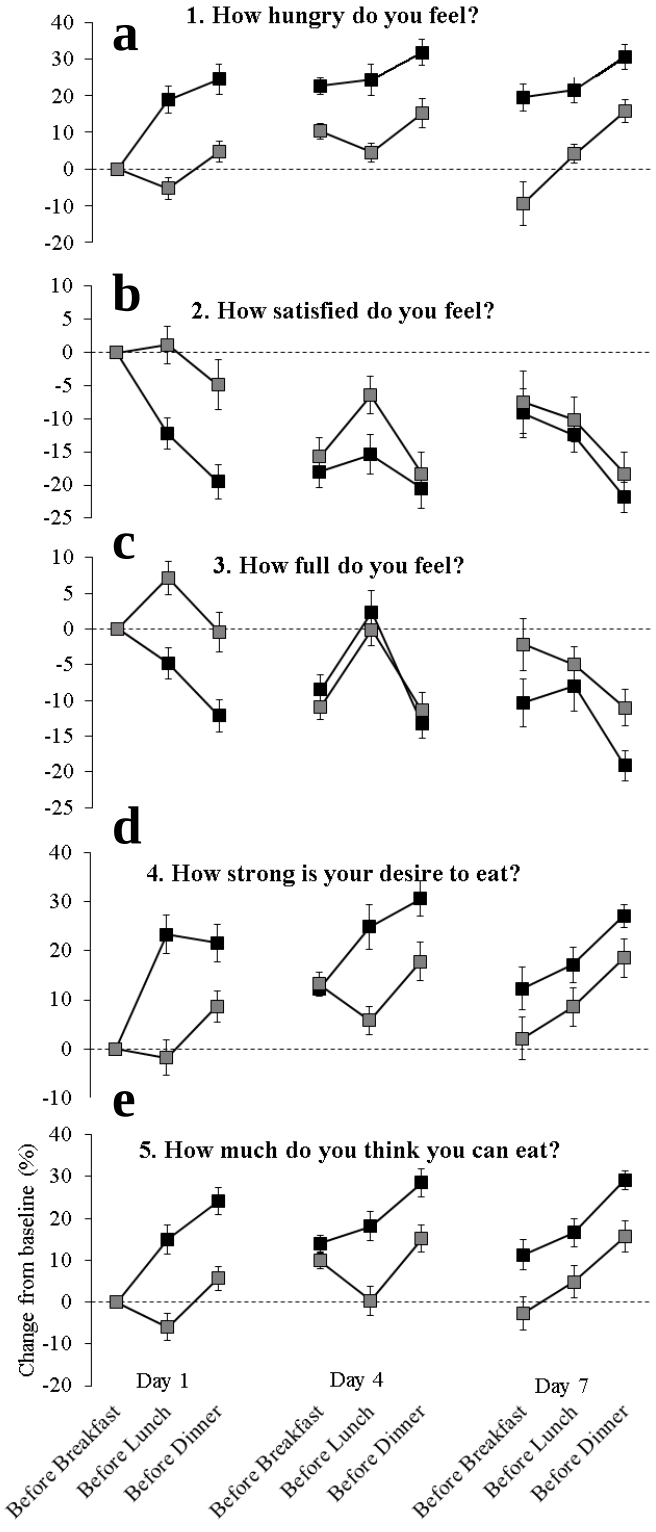

Figure 5.17 Change form baseline VAS scores during the diet week at the end of each post absorptive period (breakfast, lunch and dinner).

Whilst the present study only involved a small number of subjects and the dietary intervention was over a short period, previous studies have shown a significant effect of a 5 week HGI versus LGI diet on postprandial blood glucose levels [117] and it is clear that the glycaemic response is not a static factor, but rather physiologically dependent and adaptive. The insulin results in this study are also consistent with previous studies following a morning test meal of similar energy and glycaemic index [117] and significant differences in AUCs on both pre and post diet test days were found.

Gastric emptying data showed evidence of adaptive changes even after a 7 day dietary intervention. It is well established that emptying of gastric contents is dependent on meal volume and energy intake [86] and that increasing the fibre content in a test meal slows down gastric function [121]. Highly significant differences in the gastric content remaining 20 minutes post consumption of the HGI compared to the LGI test breakfast ($P < 0.001$) were found with faster emptying on the HGI visit. The significant difference between HGI and LGI gastric content AUC's observed on the pre diet test day was not seen on the post diet test day, such that there was a significant main effect of diet across the 7 day dietary intervention ($P < 0.005$). Adaptive changes in gastric function have been observed previously [122, 123] after a 14 day high fat dietary intervention. The findings of this present study are consistent with these studies as the gastric contents AUC following the LGI diet tended to be smaller post diet compared to pre diet indicating a faster emptying of stomach contents after adaptation. The finding of a slower gastric emptying following a week on HGI diet was in contrast to Horowitz *et al.* who reported an increased gastric

emptying of glucose following a 4 – 7 day diet with a glucose dietary supplement compared to without [124]. However, in that study the extra glucose would count towards increased energy consumption per day whereas in this present study diets where isocaloric. The effects observed in this study suggest that gastric function adapts to a HGI or LGI diet so as to normalise its effects. The standard western diet will have a glycaemic index somewhere between the extremes of these diets, and the first pre diet test breakfast represents a sudden extreme divergence from this norm. The observed effects were then mitigated as the diet was regularly consumed.

Subjective appetite ratings in response to the test breakfasts showed trends as expected and has been previously reported [125]. Pre diet VAS ratings, normalised to overnight fasted scores, reflected in an increased feeling of hunger and decreased feelings of fullness during the high- versus the low- GI test day (and it seems likely that significance would have been reached given a larger sample size). This has been linked to activity in brain regions related to reward and cravings [126]. Other studies have shown that longer term low glycaemic load dietary interventions were more satiating compared with high GI interventions [101]. Interestingly, during the HGI arm hunger ratings tended to be less and fullness ratings tended to be greater on the post diet test day compared to pre diet test day with the AUC significantly greater for the question ‘how full do you feel?’. This may be reflective of the slowed gastric emptying observed.

This study showed for the first time an increased glycogen storage following a HGI breakfast compared with an isocaloric LGI breakfast. Glycogen changes

over time were similar to previous studies, with increases from fasted levels following a morning meal [127]. During the pre diet test day the increase in mean absolute glycogen levels following the HGI breakfast accounted for 25% of the ingested intake, in strong agreement with the literature [63]. Following the LGI breakfast the increase in mean absolute glycogen levels only accounted for 15% of intake. As shown in Chapter 4, a low dose morning challenge did not induce a rise in hepatic glycogen stores but rather prevented a decline [60]; the findings in the present study may also suggest that the proportion of food taken up for hepatic glycogen synthesis can be affected by the glycaemic response or glucose absorption rate. The hepatic glycogen response to the HGI breakfast seen in this study bore a strong resemblance to the leading study on directly assessed hepatic glycogen metabolism [11] which tested the response to a test meal with a high glucose content and found peak hepatic glycogen stores between 240 and 300 min, followed by a steady decline to 600 minutes. By contrast, the low GI breakfast of the present study led to lower peak hepatic glycogen levels (though still significantly above baseline) which subsequently declined from 180 minutes until the end of the scan day. Similar findings have been reported in muscle in a number of studies [14, 128] in which HGI test meals prompted a greater storage of muscle glycogen. This relationship can be explained due to the increased insulin levels observed, which will drive an increased rate of glycogenesis. This study also showed a significantly greater variability in the HGI glycogen response compared with LGI which should be considered in future studies.

For the first time this study showed a significant increase in fasted and peak glycogen levels following a 7 day HGI diet compared to before the start of the diet, which was not observed during the LGI diet. It may be hypothesized that this is due to a similar effect as that observed following the HGI v LGI breakfast intake where there was higher subsequent glycogen storage for HGI. Glycogen levels after the previous evening meal will be the starting point for the decline in glycogen through the overnight fast, and so an elevated evening postprandial glycogen level will result in an elevated morning fasted measurement.

Most striking in the present study was the liver lipid measurements (Figure 5.13). Mean lipid levels increased over the course of the HGI diet and decreased slightly over the course of the isocaloric LGI diet, with a significant main diet effect. Previous studies have shown liver lipid levels can be perturbed over a short dietary intervention period [4] even after only a 4 day hypercaloric intervention [129]. The novel aspect of this present study is that isocaloric and macro nutrient matched diets were examined in a cross over design, elucidating new information about the effect of glycaemic index specifically on liver lipid deposition. In a recent cross sectional analysis, Valtuena *et al* reported a strong correlation between steatosis grading and dietary GI assessed from 3 day food diaries [130]. They also reported that this correlation was not observed with total carbohydrate content, total fibre content or glycaemic load. The present study corroborates this evaluation and shows remarkably that glycaemic index increases liver lipid storage even under isocaloric regimes. The implications on dietary advice and relevance to clinical

practice are obvious. Liver fibrosis, hepatosteatosis and non-alcoholic fatty liver disease is becoming an increasing burden on health services globally, and the short term build-up of liver lipids in response to dietary intake is the obvious precursor to these diseases. Previous studies have observed that a 5 week LGI diet decreases total fat mass and improves lipid profiles in overweight men [98] which suggests that the improvements observed in this study may be sustained over longer dietary interventions, although future studies should explore this also.

Given that the two diets used in this study were isocaloric, and there was no weight change over the course of the diet week, it is likely that energy balance was achieve with both diets. Further work is needed to assess the possible effects of the low GI diet on intramuscular fat content and muscle glycogen content to establish whether the lower liver levels seen with this diet are mirrored by elevated muscle levels. Glycogen storage in the muscle seems a prime candidate for an alternative energy sink and previous studies have shown that prior meal intake can affect muscle glycogen synthesis rates following subsequent meals, the so called ‘second meal’ effect [28]. This does however seem conflicting with studies that have shown an increased muscle glycogen uptake after high GI meals [14, 128]. As far as the author is aware, there are presently no studies that have looked at the longer term effect of glycaemic index dietary intake on glycogen storage in the muscle and future studies should explore this. An alternative or corresponding hypothesis could be that there is a change in the overall glycogen turnover on a low vs high GI diet. Wee *et al* did report a lesser reduction in post exercise muscle glycogen

following a LGI breakfast compared with a HGI breakfast, and that lipid oxidation plays more of a role in energy demands following low GI meals[128]. Studies have also reported a lower resting energy expenditure on high GI diets compared to low GI diets [131, 132] which would presumably result in a greater overall energy storage. This adaptive change in energy metabolism has not yet been fully addressed and future studies should employ a crossover design study to explore the final fate of consumed meals.

5.4 Conclusions

This chapter has explored the use of ^{31}P MRS, ^{1}H MRS and ^{13}C MRS for *in vivo* investigations of hepatic metabolism. Two separate studies were conducted, the first of which considered the shorter term impact of oral fructose consumption on hepatic ATP homeostasis, and the second looking at the longer term impact of different glycaemic index diets on liver lipid and glycogen stores. Both are relevant in understanding the current prevalence of NAFLD and metabolic disorders, and working towards preventative measures.

In the first study it was shown that depletion in hepatic ATP reserves following an oral fructose challenge is observable using ^{31}P MRS in healthy subjects, allowing for a completely non-invasive assessment of ATP synthesis. BMI was negatively correlated with the time to minimum ATP levels, and both BMI and liver fat were negatively correlated with ATP levels post consumption indicating an impaired hepatic energy homeostasis in subjects with higher BMI. Baseline hepatic glycogen levels were also inversely correlated with ATP synthesis rates indicating a potential area for future work. These findings open

up the interesting possibility of making simple non-invasive measures of liver health prior to the onset of more damaging conditions.

The second study explored the impact of a high versus low GI diet on liver health and metabolism. The blood glucose and insulin responses were as expected, and satiety levels followed the expected trends. This study showed for the first time a greater rise in hepatic glycogen stores following a high compared to a low GI test breakfast, and also that a 7-day high GI diet tended to increase liver glycogen. Most strikingly, the 7 day high GI diet caused a rise in liver fat stores and conversely a low GI diet cause a decrease in liver fat stores. Future studies should explore the basic physiology and clinical significance in more detail.

In summary, the MRS techniques used in these studies have unveiled new information and can be used either in the clinical setting or to explore potentially beneficial lifestyle interventions. These studies show that MRS provides powerful methods of non-invasively measuring hepatic metabolism *in vivo*. Future investigations should explore the findings of these studies further.

Whilst the strength of ^{1}H MRS and ^{13}C MRS in investigating lipid and glycogen levels has been clearly shown in this chapter, there are still sensitivity difficulties associated with ^{13}C MRS, and there would be obvious benefits in combining these measures into one. The next chapter explores a new technique that could potentially measure glycogen and lipid levels alongside each other using chemical exchange saturation transfer (CEST) techniques, observable in ^{1}H MRS.

Chapter 6 SpectroCEST to Measure Liver Lipid and Glycogen Levels

This chapter explores a new alternative method of measuring glycogen and lipid levels simultaneously using a novel technique named spectroCEST. The theory behind the technique is first described. The experimental sections report the results from a number of phantom studies. Finally, preliminary in vivo data is shown and discussed along with future directions for research

6.1 Background

6.1.1 Introduction

Chapter 3 highlighted the importance of glycogen and lipid as energy stores in the liver. Investigating the relationship between the metabolic pathways leading to these is likely to help further understanding of the basic physiological responses to meal intake and metabolic disorders. However, one of the problems in conducting MRS liver studies of lipid and glycogen stores is that multiple coils and scan routines (^{1}H MRS and ^{13}C MRS) are required, and ^{13}C MRS scans can increase scan durations. However, CEST techniques (as discussed in Section 2.5.2) potentially provide a method of measuring lipid and glycogen levels in a single scan session. This technique is based on the fact that

the magnetization of hydrogen nuclei in water will transfer to hydrogen nuclei in glycogen via chemical exchange and vice versa. Saturating the hydrogen spins of glycogen leads to a change in water peak signal and can be used to calculate glycogen levels. At the same time, individual spectra can be averaged to produce the usual spectrum used for liver lipid analysis.

6.1.2 GlycoCEST *in vivo*

Van Zijl *et al* [133] have explored the use of CEST sequences to measure glycogen concentrations via the exchange of saturated hydrogen nuclei in the hydroxyl group (OH) with water. Glycogen, and its monomer glucose were explored in a number of CEST experiments *ex vivo* and *in vivo*.

The hydroxyl group of glycogen and glucose resonates at a frequencies between 0.5 and 1.5 ppm downfield from water, which lie extremely close to the water peak with lower resolutions available at lower B_0. For saturation transfer to be measurable the slow MR exchange condition must be fulfilled:

$$\Delta\omega \gg k$$

where $\Delta\omega$ is the frequency offset from water and k is the exchange frequency. Van Zijl *et al* showed that whilst the OH group is visible in ^{1}H MRS for glycogen in pure water at low temperatures, in physiological conditions (pH ~7.1; temperature ~37^{o}C) the signal becomes much smaller, and in most cases (at 3T) become undetectable. This was attributed to a faster exchange between glycogen OH and water and was reflected in the Z spectra in which MTR_{asym} was undetectable at lower pH and temperature and became more visible in physiological conditions.

Others have considered the NOE effects, i.e. cross relaxation of the OH group on water [134]. The cross relaxation effect can be defined as

$$NOE_{water} = T_1\sigma$$

Equation 6.1

where $T_1$is the longitudinal relaxation of water and σ is a cross relaxation product between water and glycogen. Ling *et al*. noted that NOE in the ^{1}H MR spectra has been recorded for glycogen previously [135] where saturation of the water proton caused a negative NOE for the OH group (H_1, 5.38 ppm) of glycogen in H_2O. As such, NOE peaks up field from water may complicate an MTR_{asym} analysis and it may be more appropriate to use Lorentzian fitting to quantify CEST effects (Section 2.5.3).

6.1.3 Combined glycoCEST Spectroscopy and Lipid Measurements

The aim of this study was to develop a combined MR CEST acquisition to measure lipid and glycogen levels in a single scans session. The CEST Z spectrum can be obtained by acquiring ^{1}H MRS with varying frequency offset of the presaturation pulses and measuring the variation in the water peak signal to give the Z spectrum (Figure 6.1).

The Z spectrum can be used to determine glycogen levels whilst individual suppressed and unsuppressed spectra can be averaged and used to calculate liver fat fractions.

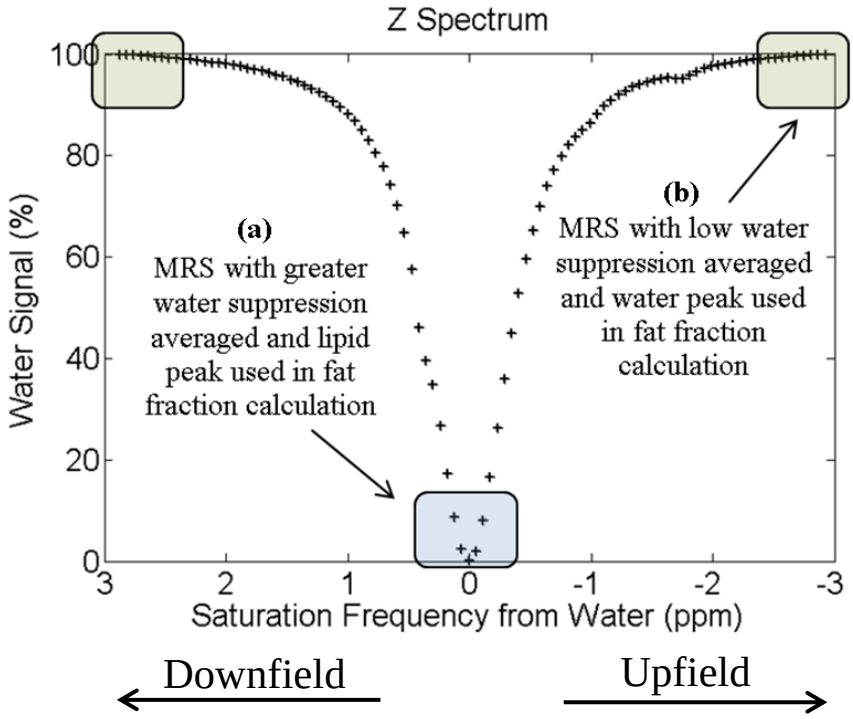

Figure 6.1 Simulated Z spectrum showing regions where spectra can be averaged for water suppressed (a) and non supressed (b) signal.

Glycogen Levels

Equation 2.26 can be used to measure the chemical exchange between glycogen OH and water (0.5 – 1.5 ppm) which is an indirect measure of glycogen levels. The effect of glycogen can be seen in the asymmetry of the Z spectrum (Seen at ~0.5ppm on simulated Z spectrum Figure 6.1)

Liver Lipid Levels

Due to the large water peak in the spectrum, ^{1}H MRS liver lipid studies often compare the lipid peak signal from a water suppressed sequence with the water peak signal from an unsuppressed acquisition (Chapter 5). The Z spectrum provides suppressed spectra for saturations frequency offsets around the water

peak frequency, whereas saturations far off resonance will give unsuppressed spectra.

In this study spectra in regions of high water suppression (Figure 6.1a) were averaged to produce a spectrum with low water signal therefore improved fat distinction and spectra in regions of low water saturation (Figure 6.1b) were averaged to produce a spectrum with a full water signal. The ratio of lipid peak area from the suppressed spectrum and the water peak area from the unsuppressed spectrum was used to determine the liver lipid fat fraction. This technique has been called spectroCEST

6.2 Pilot Study

6.2.1 Method

MR protocol

For phantom experiments a low power pre saturation pulse train with gradient dephasing was programmed on the Philips scanner, followed by a PRESS or STEAM localisation technique (Figure 6.2). Saturation was achieved using a long duration, continuous wave low power RF pulse (B_1 between 0.1 and 1 μT, total time = 1000ms). Previous studies have applied crusher gradients following the presaturation pulse [133] in order to dephase any unwanted signal. To enhance this effect in this study the saturation pulse was split into 10 smaller pulses (100ms) with a small gap in between for a short high power crusher gradient (0.5ms). The spacing between pulses was small enough for

relaxation effects to be negligible with the crusher gradients acting to destroy transverse magnetization.

Presaturation pulses were applied over a range of frequencies that varied for each study. In order to prevent saturation build up between subsequent scans the first saturation pulse was applied at the water frequency (0 Hz), and subsequent scans alternated between negative and positive presaturation frequencies (±*x* Hz).

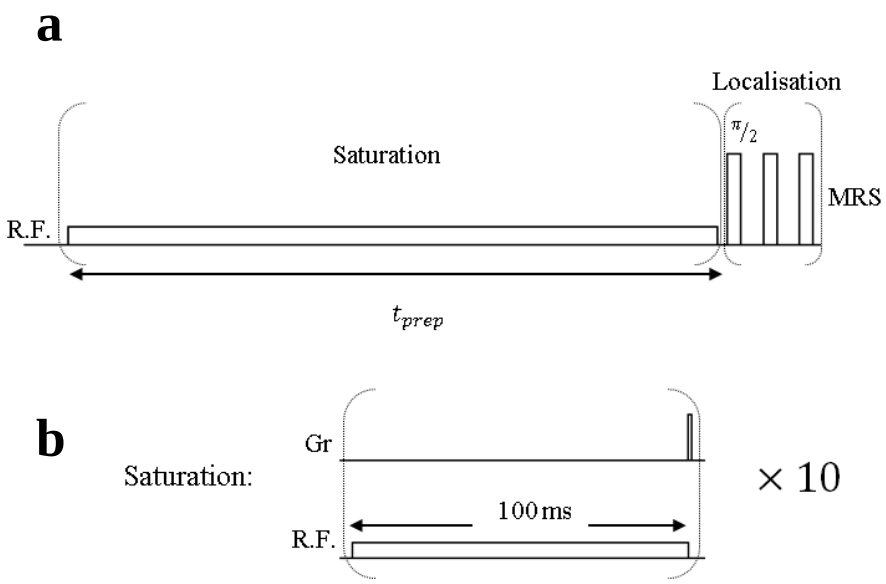

Figure 6.2 Pulse sequence of spectroCEST showing overall scan (a) and saturation blocks (b).

Phantom Studies

Glycogen Phantoms. Three 100ml glycogen phantoms were created with increasing concentrations similar to *in vivo* hepatic glycogen concentration: 100 mmol/l, 200 mmol/l and 400 mmol/l (~0.05% sodium azide added for

preservation). For all scanning glycogen phantoms were kept warm using hot water bottles (~37 ^{O}C) to ensure chemical exchange.

For each phantom a non-localised ^{13}C MR spectra was acquired (adiabatic half passage sequence, BW = 7000Hz, TR ~2000ms, NSA = 200, 1024 datapoints) using the PulseTeq surface coil (Surrey, UK), as discussed previously

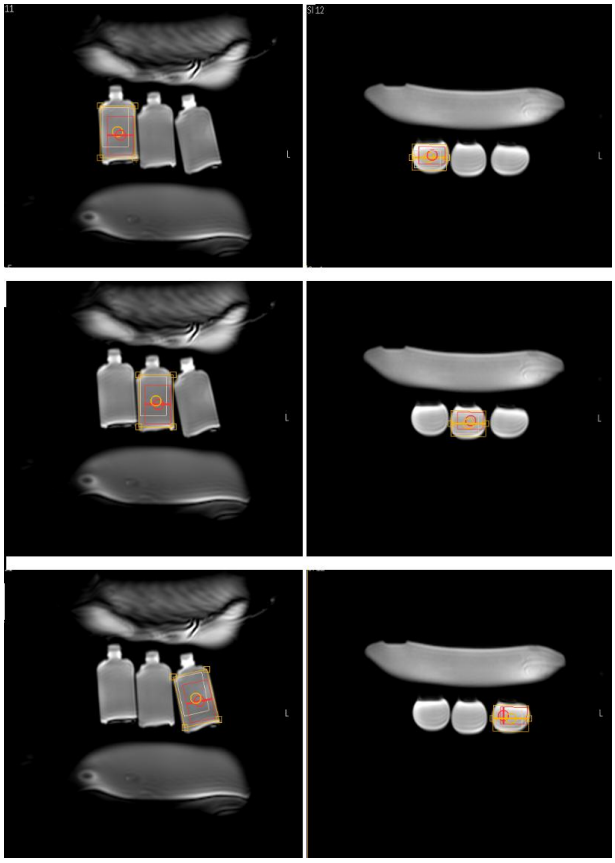

Figure 6.3 MRI of three 100ml glycogen phantoms of varying concentration showing localization of 100 mmol/l (top), 200 mmol/l (middle) and 400 mmol/l (bottom) for spectroCEST.

Following this, all three phantoms were placed next to each other and MRI scans were acquired using a Philips XL torso coil (Best, Netherlands) as shown

in Figure 6.3 (hot water bottles also seen). For each phantom, STEAM localized ^{1}H MR spectra were acquired (20mm x 30mm x 45mm) using the novel spectroCEST technique described above (Figure 6.2) with saturation frequencies ranging from -1000 Hz to 1000 Hz in 20 Hz steps (TE = 20, TR = 2046, 1024 datapoints, Saturation $B_1 = 0.25\mu T$). STEAM was used because previous studies have shown beneficial effects in *in vivo* studies where low motion is expected [24] as described in Section 4.2.

Glucose and Fat Phantoms. van Zijl *et al.*[133] demonstrated that the Z spectrum from glucose has a similar sensitivity to glycogen, although it contains more exchangeable hydrogen. Given its similar response to glycogen, glucose was used in a second phantom experiment to explore combined CEST and lipid measurements using spectroCEST. Two glucose + fat phantoms were produced with different glucose concentration (100 mmol/l and 200 mmol/l) and constant fat concentration (24g). Coconut oil was used as the fat component because it shares a similar fat peak to the main *in vivo* ^{1}H MRS peak (CH_2 fatty acid backbone). Given that *in vivo* studies have shown PRESS may have benefits where motion is expected [68], PRESS was used for this study in order to explore spectroCEST using both STEAM and PRESS localisation. For each phantom, PRESS localized ^{1}H MRS was acquired (30mm x 30mm x 30mm) using spectroCEST (Figure 6.2) with saturation frequencies ranging from -1000 Hz to 1000 Hz in 20 Hz steps (TE = 35, TR = 24223, 512 datapoints, saturation $B_1 = 1\ \mu T$).

***In Vivo* Pilot**

Preliminary *in vivo* spectroCEST was acquired from two subjects. Ethical Permission was obtained from the local medical School Research Ethics Committee. Subjects were safety screened and gave informed consent before being scanned.

Firstly, a PRESS localized *in vivo* Z spectrum was acquired using spectroCEST (Figure 6.2) during 4 breath holds (saturation ω_0 = 0 and $\pm\Delta\omega$ Hz for each breathhold, where $\Delta\omega$ = 50, 100, 150 and 1000, B_1 = 1μt, N = 3 and VOI = 65 x 65 x 65 mm, Figure 6.4).

Following this, the sequence was repeated in a different subject with varying saturation pulse power (B_1 = 0, 0.5, 1, 2, 3 and 4μT) and analysed to compare the best *in vivo* power for glycogen saturation transfer.

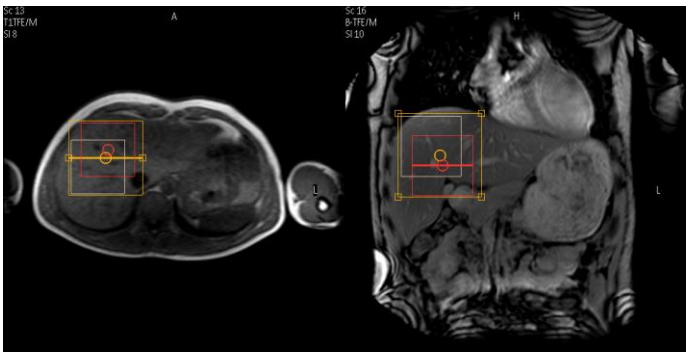

Figure 6.4 MRI of subject for pilot CEST spectroscopy data showing large localization VOI in the liver.

6.2.2 MRS Analysis

The CEST effect was measured using a programme written in Matlab. ^{1}H MR Spectra were auto phase corrected using the programme discussed in Section

4.2 and the peak height of the water signal was calculated for each spectrum. This was plotted across the saturation range to produce the CEST Z spectra. Because of the expected NOE cross relaxation effects discussed previously, glycogen analysis used the Lorentzian difference method (Equation 2.26). For glucose phantom analysis a more simple Asymmetry analysis was used (Equation in Figure 2.13).

For the glucose phantom and *in vivo* data, individual ^{1}H MR spectra were used to determine the fat fractions present. Water suppressed spectra (defined when water signal was below 2%) were averaged and used to determine the lipid peak area, and non-water supressed spectra (defined when water signal was above 98%) were averaged and used to determine the water peak area. Fat to water ratios were used to determine the fat fraction as described previously.

For the glycogen phantom experiment, *in vivo* ^{13}C MRS was zero filled to 4096 data points and line broadened as described in Chapter 5 and the glycogen / reference peak ratios were compared with the CEST Lorentzian difference in the glycogen region of the Z spectra

The error ranges were estimated from the noise in individual spectra and calculated for the Z spectrum analysis through error propagation.

Phantom Studies

Glycogen phantoms. The CEST effect downfield from water for each of the three glycogen phantoms is shown in Figure 6.5a where the Lorentzian difference is the difference between the Z spectrum and the Lorentzian fit. The

area under the LD curve was 160 ± 2 , 287 ± 2 and 475 ± 2 x10^3 %Hz for the 100, 200 and 400 mmol/l glycogen phantoms respectively.

Correlations between glycogen concentration and area under LD curves are shown in Figure 6.5b and significant fit to a straight line ($P < 10^{-7}$).

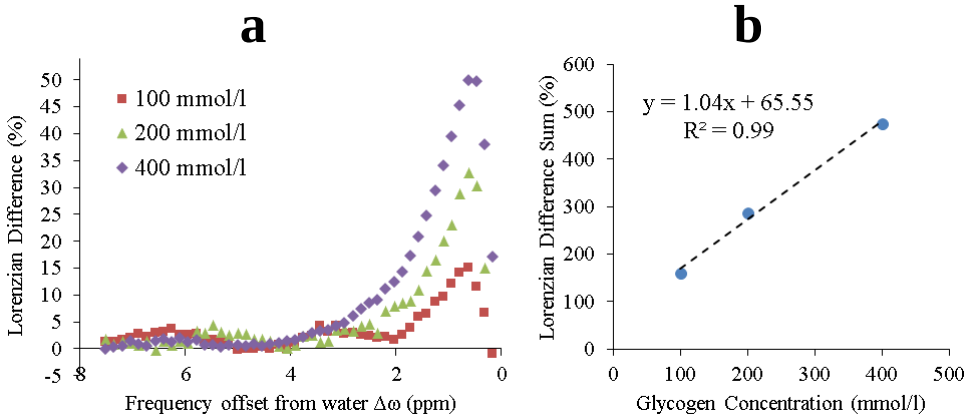

Figure 6.5 Lorentzian difference of each glycogen phantom (a) showing correlation between glycogen concentration and sum under curves (b).

The glycogen CEST results also correlated well with the measurements using ^{13}C MRS shown in Figure 6.6.

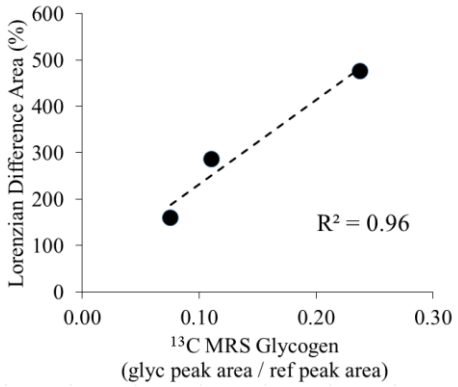

Figure 6.6 Correlation between ^{13}C MRS and area under Lorentzian difference curve ($R^2 = 0.96$, $P<10^{-7}$).

Glucose and Coconut Oil. Acquiring ^{1}H MRS using the spectroCEST sequence gave good quality spectra for water and lipid peak analysis (Figure 6.7).

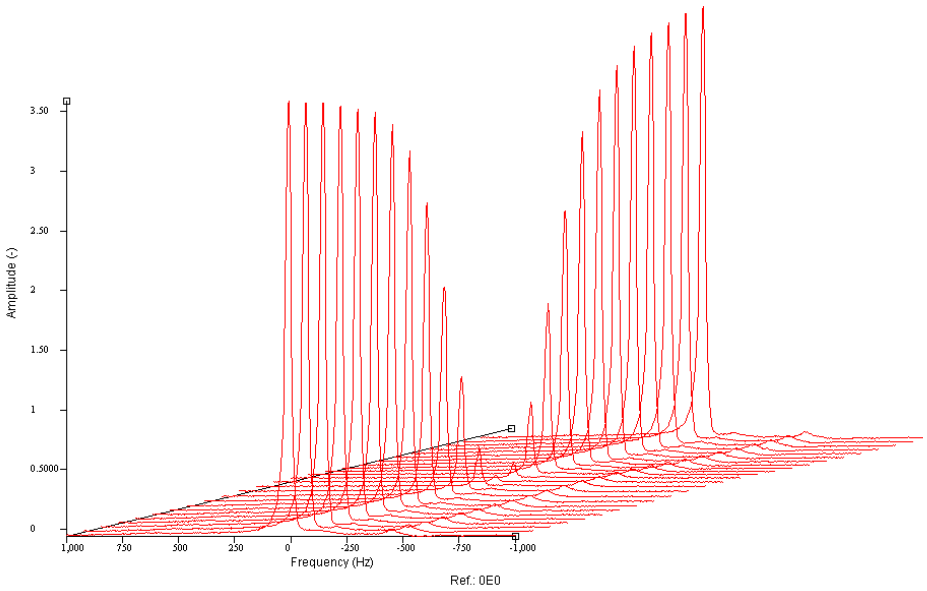

Figure 6.7 ^{1}H MRS acquired at varying saturation frequencies.

25 out of the 100 spectra acquired from the 100 mmol/l phantom are shown in Figure 6.7 with varying pre saturation pulse frequencies going into the page. Figure 6.8 shows the full Z spectrum produced from this data and the 200mmol/l phantom, and also the MTR_{asym}. The asymmetry peaked at ~2 ppm with values of 11.0 ± 0.4 and 16.7 ± 1.5 for the 100 and 200 mmol/l respectively.

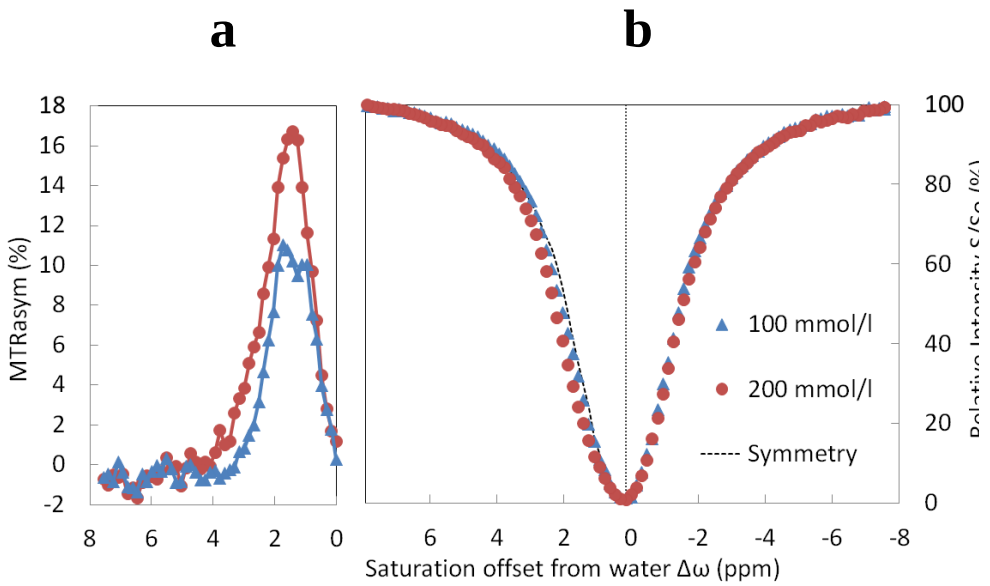

Figure 6.8 $\boldsymbol{MTR_{asym}}$ (a) and Z spectrum (b) for two different concentrations of glucose + 24g fat phantoms (100mM and 200mM).

The area under asymmetry curves was 108 ± 7 and 182% ± 9 x10^3 %Hz for the 100 mmol/l and 200 mmol/l phantoms respectively. Errors are estimated from noise propagation (Figure 6.9)

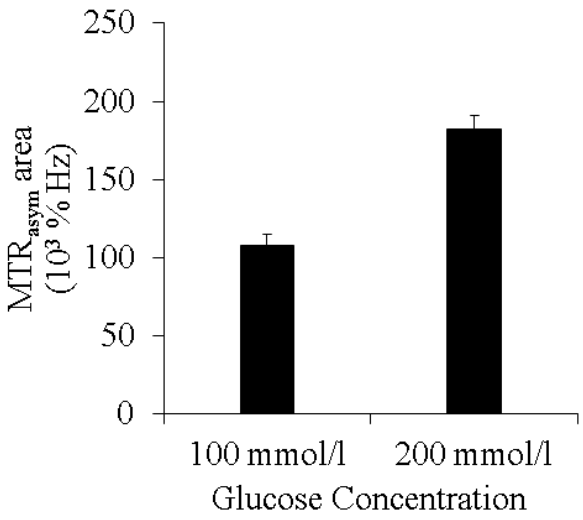

Figure 6.9 Area under Asymmetry curve for both glucose phantoms.

The water unsuppressed ^{1}H MR spectrum (averaged where $S/S_0 > 98\%$) is shown in Figure 6.10 (left) and the water unsuppressed spectrum (averaged where $S/S_0 < 2\%$) is shown in Figure 6.10 (right).

The fat peak / water peak ratios were 0.028 ± 0.004 for the 100 mmol/l phantom and 0.036 ± 0.004 for the 200 mmol/l. The fat fractions calculated were 4.7 ± 0.7 % and 5.9 ± 0.7 % for the 100 and 200 mmol/l glucose phantoms respectively.

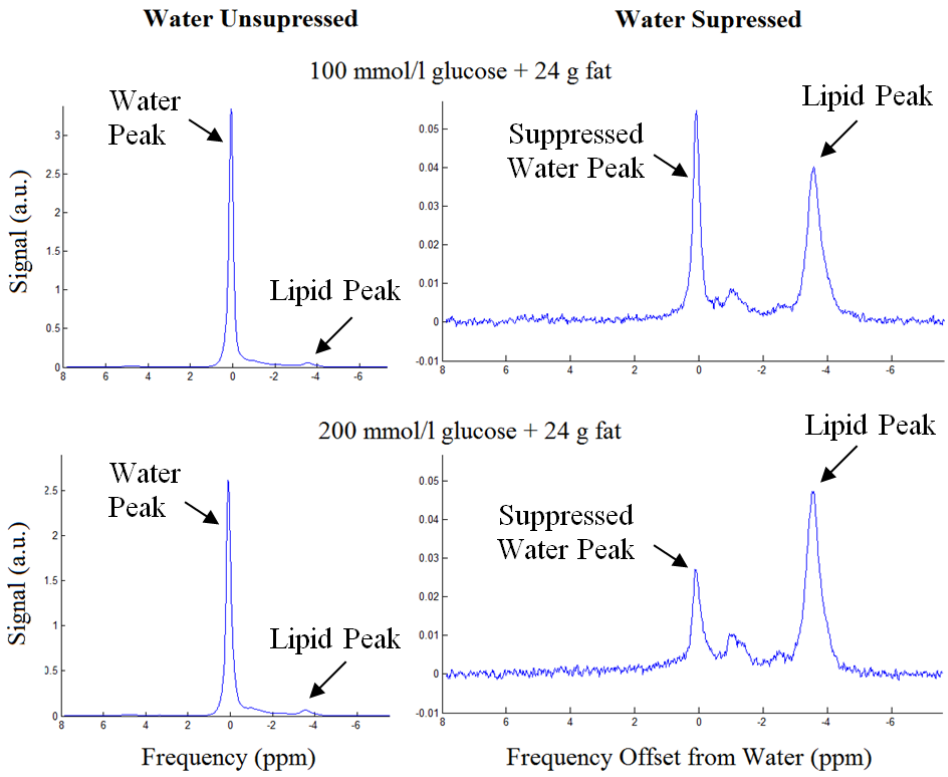

Figure 6.10 ^{1}H MRS spectra used for Z spectra in Figure 6.8 and averaged for water signal >98% max (left) and water signal <2% max (right). Top is the 100 mmol/l glucose phantom and bottom is the 200 mmol/l glucose phantom.

In Vivo Pilot

Figure 6.11a shows the ^{1}H MR spectra with saturation frequencies of 0, -0.8 and +0.8 ppm off resonance from water. The reduction in water signal at +0.8ppm is due to the saturation transfer from glycogen. Normalizing this to the signal of no saturation reveals the *in vivo* Z spectra shown in Figure 6.11b. The asymmetry has a peak of 5.3 ± 0.5% representing glycogen saturation transfer. The fat/water ratio gave a liver fat fraction of 5 ± 1 %.

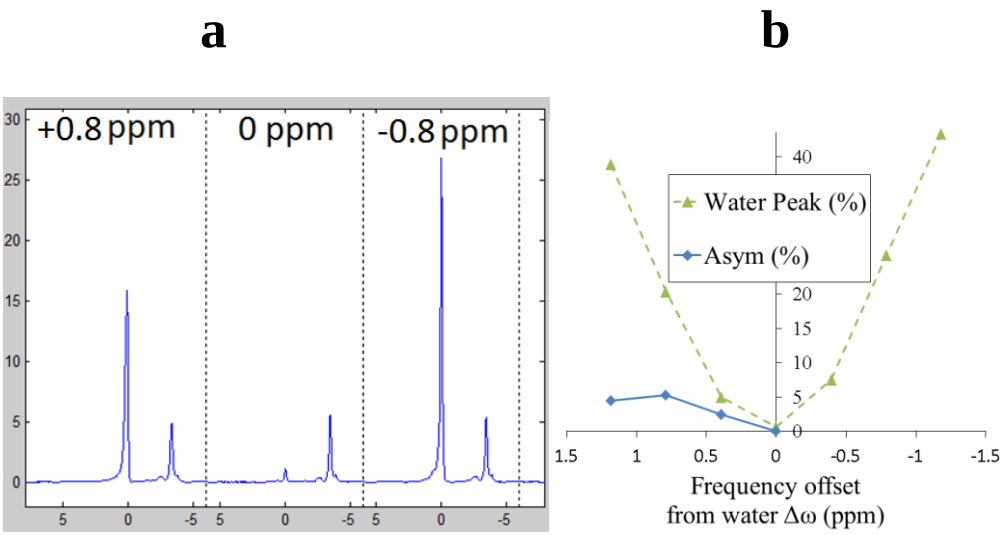

Figure 6.11 *In vivo* ^{1}H MRS (a) at +0.8, 0 and -0.8ppm showing change in water peak height I*n vivo* Z spectra generated from acquired spectra (b).

The results of the second pilot *in vivo* study acquired at varying saturation pulse strengths at a frequency offset ±0.8 ppm is shown in Figure 6.12. The difference between these curves (asymmetry) represents the saturation transfer. From the second subject, the greatest difference between peak height at ±0.8 ppm is seen for saturation B_1 of 1μT (11%).

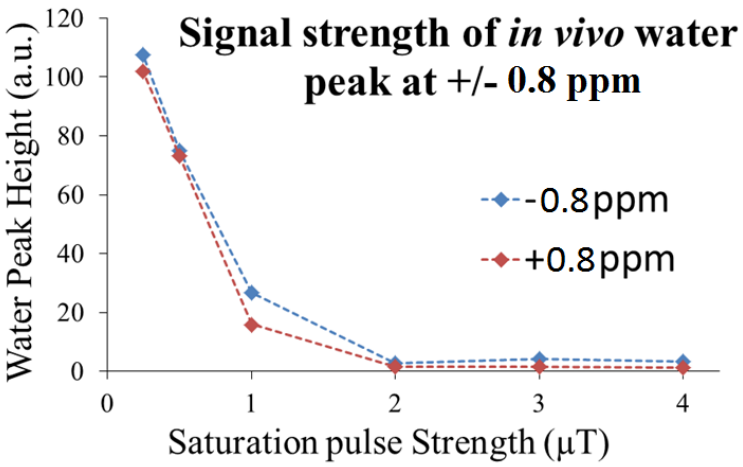

Figure 6.12 Water peak height of spectra acquired in one subject for saturation frequencies ±0.8ppm at varying $\boldsymbol{B_1}$.

6.3 Discussion

SpectroCEST experiments offer an exciting novel technique which may prove useful for *in vivo* hepatic metabolism studies. The transfer of saturation from the glycogen molecule to water provides a glycogen signal in the ^{1}H MR spectra which can be observed at body temperature allowing for a simultaneous analysis of the fat peak for liver fat levels, and the Z spectrum for glycogen levels.

The glycogen phantom data showed that a glycogen localization sequence can be successfully incorporated into the CEST saturation protocol. The CEST signal from each of the three phantoms could be distinguished from each other using MRS localisation in the novel spectroCEST protocol. The glycogen H_1 peak has been previously reported as 5.38 ppm, which lies 0.88 ppm downfield from water [135]. The data from the present study corresponds well with this as

the peak in the Lorentzian difference curve was at 0.6 ppm. However, added complications were found, attributed mainly to the reported NOE effects [55, 134] which meant that a simple asymmetry analysis was not applicable. This has been observed elsewhere, as discussed in the introduction, and as such a Lorentzian difference method of analysis was used [57]. This method proved to be useful and showed strong and significant correlations with both glycogen concentration and ^{13}C MRS. However, as van Zijl has previously shown, the relationship between concentration and glycogen CEST signal is not linear, and this needs to be explored further before attempts at quantification can be made. This is particularly important within the range of concentrations expected in hepatic studies (~100 – 400 mmol/l) and it is likely that quantifying concentrations will require computational models and curve fitting analysis. This adds complications, limiting the advantages of spectroCEST over ^{13}C MRS.

The glucose and coconut oil phantom data illustrated the potential of this technique in measuring overall hepatic metabolism and the results showed for the first time the measurement of glucose concentrations using CEST asymmetry and fat fractions using the CH_2 and water MRS peaks in a single scan session. These results are similar to van Zijl *et al*'s seminal work on glycoCEST [133], although they found over a larger range of concentrations that the CEST effect was not linear with concentration (10, 20, 50, 100 and 200 mmol/l at 4.7T).

The fat fraction measurements observed were similar across glucose phantoms, as expected. However, they were less than the actual fat fraction of the

phantoms (7.9%, 24g in 300 ml liquid). Some of this can be explained by the fact that only the CH_2 peak was measured, and the spectrum in Figure 6.10 clearly shows other lipid peaks. However, it is unlikely that this accounts for all of the under estimation. A further explanation may be that spectra were not corrected for T_2 relaxation. Future studies should measure T_2 in these phantoms by varying TE, which was shown to be important in Chapter 4.

Pilot *in vivo* data showed the potential use of spectroCEST in *in vivo* liver studies. Although this was only conducted on one subject, the Z spectra showed a peak asymmetry at the frequency of glycogen, which suggests that *in vivo* spectroCEST is viable. One potential difficulty is the limited resolution of the Z spectrum that can be acquired during one breath hold given the time required to achieve successful saturation. However, this would not be a limitation for muscle glycogen measurements.

The results showing the difference between signal just upfield / down field of water for different field strengths (Figure 6.12) gives some idea of the optimum saturation power. High pulse strength leads to increased direct saturation of water so that the difference between upfield and downfield frequencies is reduced. As the saturation pulse strength is lowered there is enough continuous saturation of the glycogen OH group for chemical exchange to take place (saturation transfer) without the direct saturation of water. However, below a certain strength the B_1 becomes too weak to provide adequate saturation, and the difference between upfield / downfield water saturation will again become negligible. Realistically, this should be repeated with multiple datasets and used to optimise the CEST sequence.

6.4 Future Work

Whilst this chapter has introduced the spectroCEST concept and investigated some of the fundamental aspects of using it as a viable alternative to glycogen and lipid measurements using ^{13}C MRS and ^{1}H MRS, problems have by no means been exhaustively covered.

The phantom protocol used in this study was limited because there was no method of controlling temperature. Ideally, a thermostat should be used to maintain body temperature (~37 ^{o}C). Once this is set up it will enable future studies to explore the exact relationship between glycogen concentration and the CEST signal as this is crucial for any future development. Phantom data should also be used to establish the measurement repeatability. Further to this, *in vivo* studies should validate glycogen measurements against ^{13}C MRS.

6.5 Conclusions

This chapter has explored using the novel technique named 'spectroCEST' as an alternative method of assessing both lipid and glycogen reserves during a signal scan session. Whilst the lipid fat fraction measurements made using ^{1}H MRS are fairly routine, the CEST technique used in this way is novel and relies on the saturation of the OH group in the glycogen molecule and its subsequent transfer to water via chemical exchange.

In the phantom studies it was shown that a range of glycogen concentrations can be observed using the spectroCEST approach, and that glucose and fat measurements can be made simultaneously using the chemical exchange of glucose seen in the Z spectrum, and the lipid and water peaks in suppressed

and unsuppressed ^{1}H MRS. NOE and other upfield effects need to be overcome, but a Lorentzian difference method of analysis gave results that corresponded well with glycogen concentrations and ^{13}C MRS data.

Preliminary *in vivo* data in two subjects showed that spectroCEST may have potential for use in metabolic studies. ^{1}H MRS data was used to determine liver fat fractions and also to produce a low resolution Z spectrum.

Chapter 7 Conclusions

In this thesis, multinuclear MRS techniques were developed and applied in a range of *in vivo* human studies, exploring the effect of dietary interventions on the healthy liver.

Firstly, post processing of ^{1}H MRS for measurements of liver lipid levels were automated and compared with manual techniques. An algorithm was written in Matlab to automate phase correction and frequency alignment of spectra and compared with subjective corrections in jMRUI. Similarly, a peak fitting algorithm was written in Matlab, and compared to peak area calculations using subjective user defined regions. A secondary end point of this first study was to consider where T_2 relaxation should be individually assessed, as has been suggested in previous studies [24]. The results from this section showed that T_2 variation was greater than inter subject variability confirming that individual T_2 relaxation measurements are important in future studies [24]. Automated post processing results were shown to correlate well with manual techniques, considerably speeding up analysis. The peak fitting algorithm gave consistently and significantly higher fat fractions, although only by a small degree. It was suggested that this probably represents a more accurate result as it includes the overlapping peak regions in the analysis. Altogether, automating post processing and using peak fitting provides a more repeatable, operator-

independent method which also requires less expertise and dramatically reduces the time of analysis. This builds on previous work covered by Hamilton *et al* [23, 24] and helps to provide a more operator friendly approach, increasing its appeal for use in a clinical setting.

Following this, the effects of surface coil B_1field inhomogeneity was considered, particularly with reference to ^{13}C MRS measurements of hepatic glycogen levels as is commonly used. To understand the signal sensitivity both the transmit power and the receive sensitivity needed consideration, as included in the law of reciprocity discussed at length by Hoult [74]. Pulse shape modelling was first used to assess the effect of varying B_1 on transverse magnetization induced by the RF pulse across the spectral bandwidth. This presents particular problems to ^{13}C MRS as it has a much wider frequency range compared with ^{1}H MRS. The adiabatic pulse response model showed the importance of fully optimising the ^{13}C MRS study before application as vendors may optimise for ^{1}H MRS (e.g. in the bandwidth of the selective inversion of the adiabatic full passage pulse). Modelling the response to the AHP pulse sweeping from ~ -2000 to 0 Hz showed that greater excitation over varying B_1 was achieved for on resonance spins and also downfield compared with a standard block pulse (although signal did drop with frequency offset). Spins upfield from resonance had a complicated response that fluctuated at the start of the sweep frequency (-2000 Hz) which would have a net effect that suppressed signal in this region. In ^{13}C MRS hepatic studies the spectrum is centred at the glycogen peak (100.4 ppm) and there is an overwhelmingly large unwanted fat signal upfield (with an external reference peak downfield) and as

such the AHP is ideal for these experiments. Applying the static field model *in vivo* it was seen that distances between coil and sample typical for liver tissue the transverse magnetization is approximately linear with $B_1$for *in vivo* experiments due to the sharp power drop. Using this information, a signal sensitivity map was modelled using a static field model and showed strong agreement compared with phantom methods. All data showed a sharp drop off in signal with distance from the coil, and this was most significant with perpendicular distance from coil. This has important implications for *in vivo* human studies, particularly when there is an expected variation in subcutaneous liver fat with body frame. This should be considered carefully, as in some experiments the distances between the coil and the liver will vary between groups and therefore impact final glycogen quantification. For example, a study comparing patients to type II diabetic patients (T2D) such as Tomiyasu *et al* [12] would expect more subcutaneous fat in the T2D group. The static field model provides a simple way of correcting for these differences.

Technical developments were also explored in the *in vivo* setting through a low dose oral glucose challenge study. This small but informative pilot study showed that ^{13}C MRS is sensitive enough to measure the decline in glycogen reserves following a period of fast but that some meals may be too small to induce observable changes from baseline.

These technical advances were applied in two human studies, one that explored the immediate postprandial changes in ATP reserves following an oral fructose challenge using ^{31}P MRS, and another that investigated the longer term change

in hepatic lipid and glycogen levels in response to a high or low glycaemic index diet using ^{1}H and ^{13}C MRS. The ^{31}P MRS experiment showed that an oral fructose challenge could be used to produce a decline in ATP reserves, and that the rate of decline and/or recovery may be related to liver health. This offers a potentially useful clinical marker that is completely non-invasive and potentially valuable, such changes in ATP reserves may predate the onset of liver disease.

The results from the 7 day high versus low glycaemic index diet elucidated new information that requires further investigation. For the first time, glycogen reserves were shown to be increased following a short term intervention with high GI diet which can be explained as a result of the rapid increase in blood sugar levels, and the output of insulin into the blood stream. It is unclear how these variations may continue to vary throughout the day, or in the longer, chronic term, and future work should explore the impact of this on other metabolic measures. Most strikingly, this investigation showed that a 7 day high glycaemic index diet significantly increased liver lipid levels in comparison to the decline seen following a low glycaemic index diet. Given that both diets were well matched for energy content and macronutrient composition, this finding suggests that the type of carbohydrate intake may play an important role in liver health. Whist a recent cross sectional study has suggested this link [130] the study presented in this thesis has shown a direct link for the first time. The accumulation of liver fat has obvious adverse effects on health and wellbeing and it has been suggested that this may be a factor that leads to type II diabetes [136]. Given the current burden of this and other

metabolic disorders, this simple dietary intervention provides a potentially powerful avenue of further research and application.

Finally, chapter 6 considered using a new alternative method of measuring liver fat and glycogen levels in a single scan routine using CEST spectroscopy. The ^{1}H MR spectrum can be used to determine the liver lipid levels through the CH_2 peak, and saturation of the OH group in the glycogen polymer can be measured indirectly through the reduction in the water peak at ~0.88ppm. Furthermore, the so called 'Z spectrum' requires the saturation of water directly, allowing for better resolution of the fat peaks in fat fraction analysis. Phantom data showed that glycogen could be measured in the Z spectrum and a localised spectroscopy routine (PRESS or STEAM) was used to determine the concentration of three glycogen phantoms. Difficulties did arise with potential NOE signals upfield from water, and a Lorentzian difference method of analysis needed to be used. A preliminary Z spectrum was also acquired *in vivo* and showed that this method may have strong potential, although much further work is required.

Magnetic Resonance Spectroscopy provides a powerful tool to investigate important aspects of hepatic metabolism *in vivo* and in a completely non-invasive way. The methods and techniques discussed in this thesis give access to unique data and carry minimal risk or discomfort to volunteers. Although biopsies will remain to be important in assessing various key parameters of liver tissue, they carry great risk to patients. Therefore, multi nuclear MRS has the unique ability to provide a complete picture of the two main energy storage

pathways in the liver (lipid and glycogen stores) in addition to ATP reserves, non-invasively and repeatedly.

In conclusion, the developments made in this thesis have clear potential to improve knowledge of human physiology and to characterise pathology and will certainly have manifold applications and a thriving future.

References

1 Zelber-Sagi, S., R. Lotan, M. Webb, Z. Halpern, and R. Oren. Incidence and Regression Rates of Nafld in a Seven Years Follow up of a Cohort from the General Population. *Journal of Hepatology*, 2011, **54**(S351-S352;

2 Birkenfeld, A.L. and G.I. Shulman. Nonalcoholic Fatty Liver Disease, Hepatic Insulin Resistance, and Type 2 Diabetes. *Hepatology*, 2014, **59**(2), 713-723;

3 Kearney, J. Food consumption trends and drivers. *Philosophical Transactions of the Royal Society B-Biological Sciences*, 2010, **365**(1554), 2793-2807;

4 Johnston, R.D., M.C. Stephenson, H. Crossland, S.M. Cordon, E. Palcidi, E.F. Cox, M.A. Taylor, G.P. Aithal, and I.A. Macdonald. No Difference Between High-Fructose and High-Glucose Diets on Liver Triacylglycerol or Biochemistry in Healthy Overweight Men. *Gastroenterology*, 2013, **145**(5), 1016-+;

5 Kechagias, S., A. Ernersson, O. Dahlqvist, P. Lundberg, T. Lindstroem, F.H. Nystrom, and F.F.S. Group. Fast-food-based hyper-alimentation can induce rapid and profound elevation of serum alanine aminotransferase in healthy subjects. *Gut*, 2008, **57**(5), 649-654;

6 Johnston, R.D., G.P. Aithal, S.D. Ryder, and I.A. MacDonald. Fast-food hyper-alimentation and exercise restriction in healthy subjects. *Gut*, 2009, **58**(3), 469-470;

7 Khoo, E.Y.H., M.C. Stevenson, E. Leverton, R. Cross, J.W. Eriksson, S.M. Poucher, I. Spendlove, P.G. Morris, I.A. Macdonald, P. Mansell, and G.P. Aithal. Elevation of Alanine Transaminase and Markers of Liver Fibrosis After a Mixed Meal Challenge in Individuals with Type 2 Diabetes. *Digestive Diseases and Sciences*, 2012, **57**(11), 3017-3025;

8 Taylor, R., T.B. Price, D.L. Rothman, R.G. Shulman, and G.I. Shulman. Validation of C-13 Nmr Measurement of Human Skeletal-Muscle Glycogen by Direct Biochemical Assay of Needle-Biopsy Samples. *Magnetic Resonance in Medicine*, 1992, **27**(1), 13-20;

9 Jue, T., J.A.B. Lohman, R.J. Ordidge, and R.G. Shulman. Natural Abundance C-13 Nmr-Spectrum of Glycogen in Humans. *Magnetic Resonance in Medicine*, 1987, **5**(4), 377-379;

10 Awad, S., M.C. Stephenson, E. Placidi, L. Marciani, D. Constantin-Teodosiu, P.A. Gowland, R.C. Spiller, K.C.H. Fearon, P.G. Morris, I.A. Macdonald, and D.N. Lobo. The effects of fasting and refeeding with a 'metabolic preconditioning' drink on substrate reserves and

mononuclear cell mitochondrial function. *Clinical Nutrition*, 2010, **29**(4), 538-544;

11 Taylor, R., I. Magnusson, D.L. Rothman, G.W. Cline, A. Caumo, C. Cobelli, and G.I. Shulman. Direct assessment of liver glycogen storage by C-13 nuclear magnetic resonance spectroscopy and regulation of glucose homeostasis after a mixed meal in normal subjects. *Journal of Clinical Investigation*, 1996, **97**(1), 126-132;

12 Tomiyasu, M., T. Obata, Y. Nishi, H. Nakamoto, H. Nonaka, Y. Takayama, J. Autio, H. Ikehira, and I. Kanno. Monitoring of liver glycogen synthesis in diabetic patients using carbon-13 MR spectroscopy. *European Journal of Radiology*, 2010, **73**(2), 300-304;

13 Casey, A., R. Mann, K. Banister, J. Fox, P.G. Morris, I.A. MacDonald, and P.L. Greenhaff. Effect of carbohydrate ingestion on glycogen resynthesis in human liver and skeletal muscle, measured by C-13 MRS. *American Journal of Physiology-Endocrinology and Metabolism*, 2000, **278**(1), E65-E75;

14 Burke, L.M., G.R. Collier, and M. Hargreaves. Muscle Glycogen-Storage after Prolonged Exercise - Effect of the Glycemic Index of Carbohydrate Feedings. *Journal of Applied Physiology*, 1993, **75**(2), 1019-1023;

15 Abdelmalek, M.F., M. Lazo, S. Bonekamp, A.M. Diehl, and J.M. Clark. Increased Dietary Fructose Impairs Hepatic Atp Homeostasis in Nafld. *Hepatology*, 2009, **50**(4), 777a-777a;

16 Thampanitchawong, P. and T. Piratvisuth. Liver biopsy: complications and risk factors. *World Journal of Gastroenterology*, 1999, **5**(4), 301-304;

17 Ratziu, V., F. Charlotte, A. Heurtier, S. Gombert, P. Giral, E. Bruckert, A. Grimaldi, F. Capron, T. Poynard, and L.S. Grp. Sampling variability of liver biopsy in nonalcoholic fatty liver disease. *Gastroenterology*, 2005, **128**(7), 1898-1906;

18 Joy, D., V.R. Thava, and B.B. Scott. Diagnosis of fatty liver disease: is biopsy necessary.? *European Journal of Gastroenterology & Hepatology*, 2003, **15**(5), 539-543;

19 Reeder, S.B., I. Cruite, G. Hamilton, and C.B. Sirlin. Quantitative Assessment of Liver Fat with Magnetic Resonance Imaging and Spectroscopy. *Journal of Magnetic Resonance Imaging*, 2011, **34**(4), 729-749;

20 Yokoo, T., M. Shiehmorteza, G. Hamilton, T. Wolfson, M.E. Schroeder, M.S. Middleton, M. Bydder, A.C. Gamst, Y. Kono, A. Kuo, H.M. Patton, S. Horgan, J.E. Lavine, J.B. Schwimmer, and C.B. Sirlin.

Estimation of Hepatic Proton-Density Fat Fraction by Using MR Imaging at 3.0 T. *Radiology*, 2011, **258**(3), 749-759;

21 Szczepaniak, L.S., E.E. Babcock, F. Schick, R.L. Dobbins, A. Garg, D.K. Burns, J.D. McGarry, and D.T. Stein. Measurement of intracellular triglyceride stores by H-1 spectroscopy: validation in vivo. *American Journal of Physiology-Endocrinology and Metabolism*, 1999, **276**(5), E977-E989;

22 Clark, M.H., R. Larsen, W. Lu, and M. Hoenig. Investigation of H-1 MRS for quantification of hepatic triglyceride in lean and obese cats. *Research in Veterinary Science*, 2013, **95**(2), 678-680;

23 Hamilton, G., T. Yokoo, M. Bydder, I. Cruite, M.E. Schroeder, C.B. Sirlin, and M.S. Middleton. In vivo characterization of the liver fat H-1 MR spectrum. *Nmr in Biomedicine*, 2011, **24**(7), 784-790;

24 Hamilton, G., M.S. Middleton, M. Bydder, T. Yokoo, J.B. Schwimmer, Y. Kono, H.M. Patton, J.E. Lavine, and C.B. Sirlin. Effect of PRESS and STEAM Sequences on Magnetic Resonance Spectroscopic Liver Fat Quantification. *Journal of Magnetic Resonance Imaging*, 2009, **30**(1), 145-152;

25 Stephenson, M.C., E. Leverton, E.Y.H. Khoo, P.S. M., L. Johansson, J.A. Lockton, E.J. W., P. Mansell, P.G. Morris, and I.A. Macdonald. Variability in fasting lipid and glycogen contents in hepatic and skeletal muscle tissue in subjects with and without type 2 diabetes: a ^{1}H and ^{13}C MRS study. *NMR in Biomedicine*, 2013, **26**(1518 - 1526;

26 Jue, T., D.L. Rothman, G.I. Shulman, B.A. Tavitian, R.A. Defronzo, and R.G. Shulman. Direct Observation of Glycogen-Synthesis in Human-Muscle with C-13 Nmr. *Proceedings of the National Academy of Sciences of the United States of America*, 1989, **86**(12), 4489-4491;

27 Jue, T., D.L. Rothman, B.A. Tavitian, and R.G. Shulman. Natural-Abundance C-13 Nmr-Study of Glycogen Repletion in Human-Liver and Muscle. *Proceedings of the National Academy of Sciences of the United States of America*, 1989, **86**(5), 1439-1442;

28 Jovanovic, A., E. Leverton, B. Solanky, B. Ravikumar, J.E.M. Snaar, P.G. Morris, and R. Taylor. The second-meal phenomenon is associated with enhanced muscle glycogen storage in humans. *Clinical Science*, 2009, **117**(3-4), 119-127;

29 van der Graaf, M., J.H. de Haan, P. Smits, A.H. Mulder, A. Heerschap, and C.J. Tack. The effect of acute exercise on glycogen synthesis rate in obese subjects studied by C-13 MRS. *European Journal of Applied Physiology*, 2011, **111**(2), 275-283;

30 Carey, P.E., J. Halliday, J.E.M. Snaar, P.G. Morris, and R. Taylor. Direct assessment of muscle glycogen storage after mixed meals in

normal and type 2 diabetic subjects. *American Journal of Physiology-Endocrinology and Metabolism*, 2003, **284**(4), E688-E694;

31 Jacobsen, N.E., *NMR Spectroscopy Explained: Simplified Theory, Applications and Examples for Irganic Chemistry and Structural Biology*. 1st ed. 2007: Wiley-Blackwell.

32 Saner, M., G. Mckinnon, and P. Boesiger. Glycogen Detection by Invivo C-13 Nmr - a Comparison of Proton Decoupling and Polarization Transfer. *Magnetic Resonance in Medicine*, 1992, **28**(1), 65-73;

33 Cortez-Pinto, H., J. Chatham, V. Chacko, C. Arnold, and A.M. Diehl. Impaired liver ATP homeostais in human nonalcoholic steatohepatitis (NASH). *Gastroenterology*, 1999, **116**(4), A1116-A1116;

34 Nair, S., V.P. Chacko, C. Arnold, and A.M. Diehl. Hepatic ATP reserve and efficiency of replenishing: Comparison between obese and nonobese normal individuals. *American Journal of Gastroenterology*, 2003, **98**(2), 466-470;

35 Oberhaensli, R.D., G.J. Galloway, D.J. Taylor, P.J. Bore, and G.K. Radda. Assessment of Human-Liver Metabolism by P-31 Magnetic-Resonance Spectroscopy. *British Journal of Radiology*, 1986, **59**(703), 695-699;

36 Nair, S., V.P. Chacko, C. Arnold, and A.M. Diehl. Basal hepatic ATP stores and recovery from fructose induced depletion in obese and lean healthy individuals: Implications in the pathogenesis of obesity associated liver diseases. *Hepatology*, 2001, **34**(4), 462a-462a;

37 Geva, T. Magnetic resonance imaging: Historical perspective. *Journal of Cardiovascular Magnetic Resonance*, 2006, **8**(4), 573-580;

38 Purcell, E.M., H.C. Torrey, and R.V. Pound. Resonance Absorption by Nuclear Magnetic Moments in a Solid. *Physical Review*, 1946, **69**(1-2), 37-38;

39 Rabi, I.I., J.R. Zacharias, S. Millman, and P. Kusch. A new method of measuring nuclear magnetic moment. *Physical Review*, 1938, **53**(4), 318-318;

40 Bloembergen, N., E.M. Purcell, and R.V. Pound. Relaxation Effects in Nuclear Magnetic Resonance Absorption. *Physical Review*, 1948, **73**(7), 679-712;

41 Lauterbur, P.C. Image Formation by Induced Local Interactions - Examples Employing Nuclear Magnetic-Resonance. *Nature*, 1973, **242**(5394), 190-191;

42 Mansfield, P. and P.K. Grannell. Nmr Diffraction in Solids. *Journal of Physics C-Solid State Physics*, 1973, **6**(22), L422-L426;

43 Ernst, R.R. and W.A. Anderson. Application of Fourier Transform Spectroscopy to Magnetic Resonance. *Review of Scientific Instruments*, 1966, **37**(1), 93-+;

44 Damadian, R., K. Zaner, D. Hor, T. Dimaio, L. Minkoff, and Goldsmit.M. Nuclear Magnetic-Resonance as a New Tool in Cancer Research - Human Tumors by Nmr. *Annals of the New York Academy of Sciences*, 1973, **222**(Dec31), 1048-1076;

45 de Graaf, R.A., *In Vivo NMR Spectroscopy: Principles and Techniques*. 2nd ed. 2007: Wiley-Blackwell.

46 Levitt, M.H., *Spin Dynamics: Basics of Nuclear Magnetic Resonance*. 2nd ed. 2008: Wiley-Blakcwell.

47 Keeler, J., *Understanding NMR Spectroscopy*. 2nd ed. 2010: Wiley-Blackwell.

48 Zeeman, P. On the Influence of Magnetism on the Nature of the Light Emitted by a Substance .32. *American Journal of Physics*, 1948, **16**(4), 218-223;

49 Callaghan, P.T., *Principle of Nuclear Magnetic Resonance Microscopy*. 1st ed. 1993, Clarendon Press.

50 Hanson, L.G. Is quantum mechanics necessary for understanding magnetic resonance? *Concepts in Magnetic Resonance Part A*, 2008, **32A**(5), 329-340;

51 Hahn, E.L. Spin Echoes. *Physical Review*, 1950, **77**(5), 746-746;

52 Bloch, F., W.W. Hansen, and M. Packard. Nuclear Induction. *Physical Review*, 1946, **69**(3-4), 127-127;

53 Vinogradov, E., A.D. Sherry, and R.E. Lenkinski. CEST: From basic principles to applications, challenges and opportunities. *Journal of Magnetic Resonance*, 2013, **229**(155-172;

54 van Zijl, P.C.M., J. Zhou, N. Mori, J.F. Payen, D. Wilson, and S. Mori. Mechanism of magnetization transfer during on-resonance water saturation. A new approach to detect mobile proteins, peptides, and lipids. *Magnetic Resonance in Medicine*, 2003, **49**(3), 440-449;

55 van Zijl, P.C.M. and N.N. Yadav. Chemical Exchange Saturation Transfer (CEST): What is in a Name and What Isn't? *Magnetic Resonance in Medicine*, 2011, **65**(4), 927-948;

56 Hua, J., C.K. Jones, J. Blakeley, S.A. Smith, P.C.M. van Zijl, and J.Y. Zhou. Quantitative description of the asymmetry in magnetization transfer effects around the water resonance in the human brain. *Magnetic Resonance in Medicine*, 2007, **58**(4), 786-793;

57 Jones, C.K., A. Huang, J.D. Xu, R.A.E. Edden, M. Schar, J. Hua, N. Oskolkov, D. Zaca, J.Y. Zhou, M.T. McMahon, J.J. Pillai, and P.C.M. van Zijl. Nuclear Overhauser enhancement (NOE) imaging in the human brain at 7 T. *Neuroimage*, 2013, **77**(114-124;

58 Zhou, J.Y., J.F. Payen, D.A. Wilson, R.J. Traystman, and P.C.M. van Zijl. Using the amide proton signals of intracellular proteins and peptides to detect pH effects in MRI. *Nature Medicine*, 2003, **9**(8), 1085-1090;

59 Tannus, A. and M. Garwood. Adiabatic pulses. *Nmr in Biomedicine*, 1997, **10**(8), 423-434;

60 Bawden, S.J., M.C. Stephenson, E. Ciampi, K. Hunter, L. Marciani, R.C. Spiller, G.P. Aithal, P.G. Morris, I.A. Macdonald, and P.A. Gowland. A Low Calorie Morning Meal Prevents the Decline of Hepatic Glycogen Stores: A Pilot *in vivo* ^{13}C Magnetic Resonance Study. *Food and Function*, 2014, **5**(9), 2237 - 2242;

61 Doyle, V.L., M. Buil, G.S. Payne, and M.O. Leach. Calculation of Sensitivity Correction Factors for Surface Coil Mrs. *Magnetic Resonance in Medicine*, 1995, **33**(1), 108-112;

62 Matson, G.B., D.J. Meyerhoff, T.J. Lawry, R.S. Lara, J. Duijn, R.F. Deicken, and M.W. Weiner. Use of Computer-Simulations for Quantitation of P-31 Isis Mrs Results. *Nmr in Biomedicine*, 1993, **6**(3), 215-224;

63 Radziuk, J. and S. Pye. Hepatic glucose uptake, gluconeogenesis and the regulation of glycogen synthesis. *Diabetes-Metabolism Research and Reviews*, 2001, **17**(4), 250-272;

64 Stevenson, E.J., P.E. Thelwall, K. Thomas, F. Smith, J. Brand-Miller, and M.I. Trenell. Dietary glycemic index influences lipid oxidation but not muscle or liver glycogen oxidation during exercise. *American Journal of Physiology-Endocrinology and Metabolism*, 2009, **296**(5), E1140-E1147;

65 Bottomley, P.A. Spatial Localization in Nmr-Spectroscopy Invivo. *Annals of the New York Academy of Sciences*, 1987, **508**(333-348;

66 Granot, J. Selected Volume Excitation Using Stimulated Echoes (Vest) - Applications to Spatially Localized Spectroscopy and Imaging. *Journal of Magnetic Resonance*, 1986, **70**(3), 488-492;

67 Frahm, J., K.D. Merboldt, and W. Hanicke. Localized Proton Spectroscopy Using Stimulated Echoes. *Journal of Magnetic Resonance*, 1987, **72**(3), 502-508;

68 Felblinger, J., R. Kreis, and C. Boesch. Effects of physiologic motion of the human brain upon quantitative H-1-MRS: analysis and correction by retrogating. *Nmr in Biomedicine*, 1998, **11**(3), 107-114;

69 Pattany, P.M., I.H. Khamis, B.C. Bowen, K. Goodkin, R.G. Weaver, J.B. Murdoch, M.J.D. Post, and R.M. Quencer. Effects of Physiologic human brain motion on proton spectroscopy: Quantitative analysis and correction with cardiac gating. *American Journal of Neuroradiology*, 2002, **23**(2), 225-230;

70 Pattany, P.M., M.G. Massand, B.C. Bowen, and R.M. Quencer. Quantitative analysis of the effects of physiologic brain motion on point-resolved spectroscopy. *American Journal of Neuroradiology*, 2006, **27**(5), 1070-1073;

71 Moyher, S.E., D.B. Vigneron, and S.J. Nelson. Surface Coil Mr-Imaging of the Human Brain with an Analytic Reception Profile Correction. *Jmri-Journal of Magnetic Resonance Imaging*, 1995, **5**(2), 139-144;

72 Letcher, J.H. Computer-Assisted Design of Surface Coils Used in Magnetic-Resonance Imaging .1. The Calculation of the Magnetic-Field. *Magnetic Resonance Imaging*, 1989, **7**(6), 581-583;

73 Hoult, D.I. and R.E. Richards. Signal-to-Noise Ratio of Nuclear Magnetic-Resonance Experiment. *Journal of Magnetic Resonance*, 1976, **24**(1), 71-85;

74 Hoult, D.I. The principle of reciprocity in signal strength calculations - A mathematical guide. *Concepts in Magnetic Resonance*, 2000, **12**(4), 173-187;

75 Altmann, S.L., *Rotations, Quaternions, and Double Groups*. 2005: Dover Publications Inc.

76 Grant, I.S.P.W.R., *Electromagnetism*. 2nd ed. 1990: Wiley-BlackWell.

77 Lavoie, C., F. Ducros, J. Bourque, H. Langelier, and J.L. Chiasson. Glucose metabolism during exercise in man: The role of insulin and glucagon in the regulation of hepatic glucose production and gluconeogenesis. *Canadian Journal of Physiology and Pharmacology*, 1997, **75**(1), 26-35;

78 Rose, A.J. and S. Herzig. Metabolic control through glucocorticoid hormones: an update. *Molecular and Cellular Endocrinology*, 2013, **380**(1 - 2), 65 - 78;

79 Consoli, A. Role of Liver in Pathophysiology of Niddm. *Diabetes Care*, 1992, **15**(3), 430-441;

80 Rampersaud, G.C., M.A. Pereira, B.L. Girard, J. Adams, and J.D. Metzl. Review - Breakfast habits, nutritional status, body weight, and academic performance in children and adolescents. *Journal of the American Dietetic Association*, 2005, **105**(5), 743-760;

81 Berkey, C.S., H.R.H. Rockett, M.W. Gillman, A.E. Field, and G.A. Colditz. Longitudinal study of skipping breakfast and weight change in adolescents. *International Journal of Obesity*, 2003, **27**(10), 1258-1266;

82 Siega-Riz, A.M., B.M. Poplin, and T. Carson. Differences in food patterns at breakfast by sociodemographic characteristics among a nationally representative sample of adults in the United States. *Preventive Medicine*, 2000, **30**(5), 415-424;

83 Ruxton, C.H.S., K.R. OSullivan, T.R. Kirk, and N.R. Belton. The contribution of breakfast to the diets of a sample of 136 primary-schoolchildren in Edinburgh. *British Journal of Nutrition*, 1996, **75**(3), 419-431;

84 Konig, M., S. Bulik, and H.G. Holzhutter. Quantifying the Contribution of the Liver to Glucose Homeostasis: A Detailed Kinetic Model of Human Hepatic Glucose Metabolism. *Plos Computational Biology*, 2012, **8**(6),

85 Eelderink, C., T.C. Moerdijk-Poortvliet, H. Wang, M. Schepers, T. Preston, T. Boer, R.J. Vonk, H. Schierbeek, and M.G. Priebe. The glycemic response does not reflect the in vivo starch digestibility of fiber-rich wheat products in healthy men. *Journal of Nutrition*, 2012, **142**(2), 258-263;

86 Kwiatek, M.A., D. Menne, A. Steingoetter, O. Goetze, Z. Forras-Kaufman, E. Kaufman, H. Fruehauf, P. Boesiger, M. Fried, W. Schwizer, and M.R. Fox. Effect of meal volume and calorie load on postprandial gastric function and emptying: studies under physiological conditions by combined fiber-optic pressure measurement and MRI. *American Journal of Physiology-Gastrointestinal and Liver Physiology*, 2009, **297**(5), G894-G901;

87 Thomas, E.L., J.A. Fitzpatrick, S.J. Malik, S.D. Taylor-Robinson, and J.D. Bell. Whole body fat: Content and distribution. *Progress in Nuclear Magnetic Resonance Spectroscopy*, 2013, **73**(56-80;

88 Johnson, R.J., L.G. Sanchez-Lozada, and T. Nakagawa. The Effect of Fructose on Renal Biology and Disease. *Journal of the American Society of Nephrology*, 2010, **21**(12), 2036-2039;

89 Cortez-Pinto, H., J. Chatham, V.P. Chacko, C. Arnold, A. Rashid, and A.M. Diehl. Alterations in liver ATP homeostasis in human

nonalcoholic steatohepatitis - A pilot study. *Jama-Journal of the American Medical Association*, 1999, **282**(17), 1659-1664;

90 Marriott, B.P., N. Cole, and E. Lee. National Estimates of Dietary Fructose Intake Increased from 1977 to 2004 in the United States. *Journal of Nutrition*, 2009, **139**(6), S1228-S1235;

91 Jalal, D.I., G. Smits, R.J. Johnson, and M. Chonchol. Increased Fructose Associates with Elevated Blood Pressure. *Journal of the American Society of Nephrology*, 2010, **21**(9), 1543-1549;

92 Schultz, A., D. Neil, M.B. Aguila, and C.A. Mandarim-de-Lacerda. Hepatic Adverse Effects of Fructose Consumption Independent of Overweight/Obesity. *International Journal of Molecular Sciences*, 2013, **14**(11), 21873-21886;

93 White, J.S. Challenging the Fructose Hypothesis: New Perspectives on Fructose Consumption and Metabolism. *Advances in Nutrition*, 2013, **4**(2), 246-256;

94 Lanaspa, M.A., C. Cicerchi, G. Garcia, N.X. Li, C.A. Roncal-Jimenez, C.J. Rivard, B. Hunter, A. Andres-Hernando, T. Ishimoto, L.G. Sanchez-Lozada, J. Thomas, R.S. Hodges, C.T. Mant, and R.J. Johnson. Counteracting Roles of AMP Deaminase and AMP Kinase in the Development of Fatty Liver. *Plos One*, 2012, **7**(11),

95 Jenkins, D.J.A., T.M.S. Wolever, R.H. Taylor, H. Barker, H. Fielden, J.M. Baldwin, A.C. Bowling, H.C. Newman, A.L. Jenkins, and D.V. Goff. Glycemic Index of Foods - a Physiological-Basis for Carbohydrate Exchange. *American Journal of Clinical Nutrition*, 1981, **34**(3), 362-366;

96 Foster-Powell, K., S.H.A. Holt, and J.C. Brand-Miller. International table of glycemic index and glycemic load values: 2002. *American Journal of Clinical Nutrition*, 2002, **76**(1), 5-56;

97 Jenkins, D.J.A., C.W.C. Kendall, L.S.A. Augustin, S. Franceschi, M. Hamidi, A. Marchie, A.L. Jenkins, and M. Axelsen. Glycemic index: overview of implications in health and disease. *American Journal of Clinical Nutrition*, 2002, **76**(1), 266s-273s;

98 Bouche, C., S.W. Rizkalla, J. Luo, H. Vidal, A. Veronese, N. Pacher, C. Fouquet, V. Lang, and G. Slama. Five-week, low-glycemic index diet decreases total fat mass and improves plasma lipid profile in moderately overweight nondiabetic men. *Diabetes Care*, 2002, **25**(5), 822-828;

99 Solomon, T.P.J., J.M. Haus, M.A. Cook, C.A. Flask, and J.P. Kirwan. A Low-Glycemic Diet Lifestyle Intervention Improves Fat Utilization during Exercise in Older Obese Humans. *Obesity*, 2013, **21**(11), 2272-2278;

100 Stevenson, E., C. Williams, G. McComb, and C. Oram. Improved recovery from prolonged exercise following the consumption of low glycemic index carbohydrate meals. *International Journal of Sport Nutrition and Exercise Metabolism*, 2005, **15**(4), 333-349;

101 Chang, K.V.T., J.W. Lampe, Y. Schwarz, K.L. Breymeyer, K.A. Noar, X.L. Song, and M.L. Neuhouser. Low Glycemic Load Experimental Diet More Satiating Than High Glycemic Load Diet. *Nutrition and Cancer-an International Journal*, 2012, **64**(5), 666-673;

102 Bawden, S.J., M.C. Stephenson, L. Marciani, G.P. Aithal, I.A. Macdonald, P.A. Gowland, and P.G. Morris. Investigating Alterations in Hepatic ATP levels following Fructose and Fructose+Glucose Ingestion: A Simple Non-invasive Technique to Assess Liver Function Using 31P MRS. *Proceedings 20th Scientific Meeting of the ISMRM, Melbourne*, 2012, **1369**(

103 Stefan, D., F. Di Cesare, A. Andrasescu, E. Popa, A. Lazariev, E. Vescovo, O. Strbak, S. Williams, Z. Starcuk, M. Cabanas, D. van Ormondt, and D. Graveron-Demilly. Quantitation of magnetic resonance spectroscopy signals: the jMRUI software package. *Measurement Science & Technology*, 2009, **20**(10),

104 Tappy, L., K.A. Le, C. Tran, and N. Paquot. Fructose and metabolic diseases: New findings, new questions. *Nutrition*, 2010, **26**(11-12), 1044-1049;

105 Korieh, A. and G. Crouzoulon. Dietary-Regulation of Fructose Metabolism in the Intestine and in the Liver of the Rat - Duration of the Effects of a High Fructose Diet after the Return to the Standard Diet. *Archives Internationales De Physiologie De Biochimie Et De Biophysique*, 1991, **99**(6), 455-460;

106 Ouyang, X., P. Cirillo, Y. Sautin, S. McCall, J.L. Bruchette, A.M. Diehl, R.J. Johnson, and M.F. Abdelmalek. Fructose consumption as a risk factor for non-alcoholic fatty liver disease. *Journal of Hepatology*, 2008, **48**(6), 993-999;

107 Ix, J.H. and K. Sharma. Mechanisms Linking Obesity, Chronic Kidney Disease, and Fatty Liver Disease: The Roles of Fetuin-A, Adiponectin, and AMPK. *Journal of the American Society of Nephrology*, 2010, **21**(3), 406-412;

108 Musso, G., R. Gambino, and M. Cassader. Emerging Molecular Targets for the Treatment of Nonalcoholic Fatty Liver Disease. *Annual Review of Medicine*, 2010, **61**(375-392;

109 Buemann, B., H. Gesmar, A. Astrup, and B. Quistorff. Effects of oral D-tagatose, a stereoisomer of D-fructose, on liver metabolism in man as

examined by P-31-magnetic resonance spectroscopy. *Metabolism-Clinical and Experimental*, 2000, **49**(10), 1335-1339;

110 Rumessen, J.J. and E. Gudmandhoyer. Absorption Capacity of Fructose in Healthy-Adults - Comparison with Sucrose and Its Constituent Monosaccharides. *Gut*, 1986, **27**(10), 1161-1168;

111 Szendroedi, J., M. Chmelik, A.I. Schmid, P. Nowotny, A. Brehm, M. Krssak, E. Moser, and M. Roden. Abnormal Hepatic Energy Homeostasis in Type 2 Diabetes. *Hepatology*, 2009, **50**(4), 1079-1086;

112 Bollen, M., S. Keppens, and W. Stalmans. Specific features of glycogen metabolism in the liver. *Biochemical Journal*, 1998, **336**(19-31;

113 Lim, E.L., K.G. Hollingsworth, F.E. Smith, P.E. Thelwall, and R. Taylor. Effects of raising muscle glycogen synthesis rate on skeletal muscle ATP turnover rate in type 2 diabetes. *American Journal of Physiology-Endocrinology and Metabolism*, 2011, **301**(6), E1155-E1162;

114 Gallis, J.L., H. Gin, H. Roumes, and M.C. Beauvieux. A metabolic link between mitochondrial ATP synthesis and liver glycogen metabolism: NMR study in rats re-fed with butyrate and/or glucose. *Nutrition & Metabolism*, 2011, **8**(

115 Choi, Y.K., F.C. Johlin, R.W. Summers, M. Jackson, and S.S.C. Rao. Fructose intolerance: An under-recognized problem. *American Journal of Gastroenterology*, 2003, **98**(6), 1348-1353;

116 Morgan, L.M., J.W. Shi, S.M. Hampton, and G. Frost. Effect of meal timing and glycaemic index on glucose control and insulin secretion in healthy volunteers. *British Journal of Nutrition*, 2012, **108**(7), 1286-1291;

117 Nazare, J.A., S. Normand, A.O. Triantafyllou, A.B. de la Perriere, M. Desage, and M. Laville. Modulation of the postprandial phase by beta-glucan in overweight subjects: Effects on glucose and insulin kinetics. *Molecular Nutrition & Food Research*, 2009, **53**(3), 361-369;

118 Henry, C.J.K. Basal metabolic rate studies in humans: measurement and development of new equations. *Public Health Nutrition*, 2005, **8**(7A), 1133-1152;

119 Flint, A., A. Raben, J.E. Blundell, and A. Astrup. Reproducibility, power and validity of visual analogue scares in assessment of appetite sensations in single test meal studies. *International Journal of Obesity*, 2000, **24**(1), 38-48;

120 Astbury, N.M., M.A. Taylor, and I.A. Macdonald. Breakfast Consumption Affects Appetite, Energy Intake, and the Metabolic and Endocrine Responses to Foods Consumed Later in the Day in Male

Habitual Breakfast Eaters. *Journal of Nutrition*, 2011, **141**(7), 1381-1389;

121 Benini, L., G. Castellani, F. Brighenti, K.W. Heaton, M.T. Brentegani, M.C. Casiraghi, C. Sembenini, N. Pellegrini, A. Fioretta, G. Minniti, M. Porrini, G. Testolin, and I. Vantini. Gastric-Emptying of a Solid Meal Is Accelerated by the Removal of Dietary Fiber Naturally Present in Food. *Gut*, 1995, **36**(6), 825-830;

122 Castiglione, K.E., N.W. Read, and S.J. French. Adaptation to high-fat diet accelerates emptying of fat but not carbohydrate test meals in humans. *American Journal of Physiology-Regulatory Integrative and Comparative Physiology*, 2002, **282**(2), R366-R371;

123 Cunningham, K.M., J. Daly, M. Horowitz, and N.W. Read. Gastrointestinal Adaptation to Diets of Differing Fat Composition in Human Volunteers. *Gut*, 1991, **32**(5), 483-486;

124 Horowitz, M., K.M. Cunningham, J.M. Wishart, K.L. Jones, and N.W. Read. The effect of short-term dietary supplementation with glucose on gastric: Emptying of glucose and fructose and oral glucose tolerance in normal subjects. *Diabetologia*, 1996, **39**(4), 481-486;

125 Bornet, F.R.J., A.E. Jardy-Gennetier, N. Jacquet, and J. Stowell. Glycaemic response to foods: Impact on satiety and long-term weight regulation. *Appetite*, 2007, **49**(3), 535-553;

126 Lennerz, B.S., D.C. Alsop, L.M. Holsen, E. Stern, R. Rojas, C.B. Ebbeling, J.M. Goldstein, and D.S. Ludwig. Effects of dietary glycemic index on brain regions related to reward and craving in men. *American Journal of Clinical Nutrition*, 2013, **98**(3), 641-647;

127 Roden, M., K.F. Petersen, and G.I. Shulman. Nuclear magnetic resonance studies of hepatic glucose metabolism in humans. *Recent Progress in Hormone Research, Vol 56*, 2001, **56**(219-237;

128 Wee, S.L., C. Williams, K. Tsintzas, and L. Boobis. Ingestion of a high-glycemic index meal increases muscle glycogen storage at rest but augments its utilization during subsequent exercise. *Journal of Applied Physiology*, 2005, **99**(2), 707-714;

129 Bortolotti, M., R. Kreis, C. Debard, B. Cariou, D. Faeh, M. Chetiveaux, M. Ith, P. Vermathen, N. Stefanoni, K.A. Le, P. Schneiter, M. Krempf, H. Vidal, C. Boesch, and L. Tappy. High protein intake reduces intrahepatocellular lipid deposition in humans. *American Journal of Clinical Nutrition*, 2009, **90**(4), 1002-1010;

130 Valtuena, S., N. Pellegrini, D. Ardigo, D. Del Rio, F. Numeroso, F. Scazzina, L. Monti, I. Zavaroni, and F. Brighenti. Dietary glycemic index and liver steatosis. *American Journal of Clinical Nutrition*, 2006, **84**(1), 136-142;

131 Pereira, M.A., J. Swain, A.B. Goldfine, N. Rifai, and D.S. Ludwig. Effects of a low-glycemic load diet on resting energy expenditure and heart disease risk factors during weight loss. *Jama-Journal of the American Medical Association*, 2004, **292**(20), 2482-2490;

132 Agus, M.S.D., J.F. Swain, C.L. Larson, E.A. Eckert, and D.S. Ludwig. Dietary composition and physiologic adaptations to energy restriction. *American Journal of Clinical Nutrition*, 2000, **71**(4), 901-907;

133 van Zijl, P.C.M., C.K. Jones, J. Ren, C.R. Malloy, and A.D. Sherry. MR1 detection of glycogen in vivo by using chemical exchange saturation transfer imaging (glycoCEST). *Proceedings of the National Academy of Sciences of the United States of America*, 2007, **104**(11), 4359-4364;

134 Ling, W., R.R. Regatte, G. Navon, and A. Jerschow. Assessment of glycosaminoglycan concentration in vivo by chemical exchange-dependent saturation transfer (gagCEST). *Proceedings of the National Academy of Sciences of the United States of America*, 2008, **105**(7), 2266-2270;

135 Chen, W., M.J. Avison, X.H. Zhu, and R.G. Shulman. Nmr-Studies of H-1 Noes in Glycogen. *Biochemistry*, 1993, **32**(43), 11483-11487;

136 Taylor, R. Pathogenesis of type 2 diabetes: tracing the reverse route from cure to cause. *Diabetologia*, 2008, **51**(10), 1781-1789;